DISSERTATION

Jacob A. Martin, Civilian, AFRL/RYMT

AFIT-ENP-DS-16-D-016

DEPARTMENT OF THE AIR FORCE
AIR UNIVERSITY

AIR FORCE INSTITUTE OF TECHNOLOGY

Wright-Patterson Air Force Base, Ohio

PASSIVELY ESTIMATING INDEX OF REFRACTION FOR SPECULAR REFLECTORS USING POLARIMETRIC HYPERSPECTRAL IMAGING

DISSERTATION

Presented to the Faculty

Department of Engineering Physics

Graduate School of Engineering and Management

Air Force Institute of Technology

Air University

Air Education and Training Command

in Partial Fulfillment of the Requirements for the

Degree of Doctor of Philosophy

Jacob A. Martin, B.S, M.S.

Civilian, AFRL/RYMT

December 2016

PASSIVELY ESTIMATING INDEX OF REFRACTION FOR SPECULAR

REFLECTORS USING POLARIMETRIC HYPERSPECTRAL IMAGING

DISSERTATION

Jacob A. Martin, B.S, M.S.
Civilian, AFRL/RYMT

Committee Membership:

Kevin C. Gross, PhD, AFIT/ENP (Chair)

Kurt G. Eyink, PhD, AFRL/RXAN (Member)

Maj. Milo W. Hyde IV, PhD, AFIT/ENG (Member)

Michael A. Marciniak, PhD, AFIT/ENP (Member)

ADEDJI B. BADIRU, PhD

Dean, Graduate School of Engineering and Management

AFIT-ENP-DS-16-D-016

Abstract

This research develops methods to determine index of refraction via polarimetric-hyperspectral radiance measurements from a remote platform without detailed *a priori* information about the target and its surroundings. A forward model is presented taking a fundamental material property, the spectrally resolved index of refraction, and relating it to a smaller number of parameters using either the Lorentz oscillator model or another model developed as part of this research. For smooth surfaces, which are the focus of this work, the reflectance and emittance of a material can be solved for using Fresnel's equations. Finally, the radiance measured by a sensor observing an object can be predicted from these reflectance values and knowledge of the downwelling radiance, object temperature, and atmospheric conditions. The goal of this research is to invert this problem, using measured polarimetric hyperspectral radiance values to estimate the complex index of refraction, $\tilde{N}$, object temperature, downwelling radiance, and viewing angle relative to the target surface normal. Data is collected using a Telops LWIR (875-1250 cm^{-1}) Hypercam which has been customized by adding a linear wire grid polarizer to the front of the instrument. The index of refraction retrieval technique is applied to synthetic data, laboratory measurements with blackbody-like downwelling radiation, and outdoor measurements over a short path under daytime, clear sky downwelling.

Results from synthetic datasets showed the how the retrieval performed when varying thermal contrast, sensor noise, spectral resolution, and combinations of viewing angles. Three datasets under laboratory conditions were examined. The first experiment explored the ability to retrieve the complex index of refraction, $\tilde{N}$, from a material much warmer than its surroundings, i.e. an emission-dominated signa-

iv

ture. Specifically, the complex index of refraction of a heated Pyrex beaker was estimated to within 0.2 rms difference when compared to "truth" estimated via ellipsometry measurements. Results show that the surface normal can also be estimated to within 5 degrees while still simultaneously fitting index of refraction object temperature, and downwelling radiance. Additionally, two experiments were conducted using a blackbody to illuminate a quartz glass block and silicon carbide wafer, i.e. a reflection-dominated signature. Using these measurements, index of refraction was retrieved to within 0.08 rms error, again compared to "truth" estimated via ellipsometry measurements, for both materials. For these two experiments, the surface normal was retrieved within $3°$ while maintaining the accuracy of the $\tilde{N}$ retrieval.

In addition to the data collected in a laboratory setting, an experiment was also conducted outdoors under clear sky day-time conditions with a variety of different targets and using a number of different settings (viewing angle, spectral resolution, etc.) The downwelling radiance under a clear sky is much more spectrally structured than the blackbody-like downwelling radiance seen the laboratory data and requires more parameters to properly describe. Even with this additional complexity, however, the index of refraction could still be retrieved to within 0.16 rms error from truth for a quartz glass target and 0.04 rms error for a sapphire glass target.

All of these results compare favorably to existing material identification techniques, specifically the maximum smoothness temperature emissivity algorithm. The primary advantage of estimating index of refraction instead of emissivity is because the index of refraction is invariant to the viewing angle, unlike emissivity. Additional work will need to be done to make this techinique useful operationally, such as accounting for rough surfaces and improving the processsing time, but this work represents the first time that index of refraction has been accurately determined hyperspectrally in the LWIR without detailed *a priori* knowledge of scene conditions.

Table of Contents

List of Figures

xvii

List of Abbreviations

PASSIVELY ESTIMATING INDEX OF REFRACTION FOR SPECULAR REFLECTORS USING POLARIMETRIC HYPERSPECTRAL IMAGING

I. Introduction

As off-nadir remote sensing platforms become increasingly prevalent in remote sensing, material identification techniques robust to changing viewing geometries must be developed. Current identification strategies often rely on estimating reflectivity or emissivity which vary with viewing angle. Presented here is a technique, leveraging a combination of two of the most common remote sensing modalities: polarimetric imaging (PI) and hyperspectral imaging (HSI), to estimate index of refraction which is invariant to viewing geometry.

Polarimetric remote sensing measures the proportion of light arriving at the sensor whose electric field is oriented in one plane as compared to an orthogonal plane. There are many different methods for measuring this, but for this work, polarization will be measured using a linear polarizer, which blocks out one linear polarization state. By rotating the polarizer to different positions, the polarization state of the radiance arriving at the detector can be determined. In addition to remote sensing applications, polarimetric imaging is used extensively in astronomy [1, 2], biology [3, 4], medicine [5, 6], and geology [7, 8]; as well as many other fields.

Within remote sensing applications, polarimetry is particularly useful in discriminating man-made targets from background. Flat, smooth objects tend to have a large polarimetric signature, while natural objects tend to have rougher, randomly oriented, surfaces, which reduces their polarization. Because of this, polarimetry is a popular modality in target detection. Polarization can also be beneficial in distin-

guishing categories of materials. Metals tend to polarize light very minimally, while dielectrics usually have a larger polarizing effect. With an understanding of certain scene conditions, this can be extended to calculate the index of refraction of materials, and/or their orientation relative to the sensor. This is of particular interest, as it directly relates to this research, and will be discussed in more detail later in this document. Measuring index of refraction at one wavelength can be useful, but different materials may often have similar indicies in one spectral band. To accurately contrast one material from another, measurements at multiple wavelengths — i.e. hyperspectral measurements — are useful.

Another common remote sensing modality is hyperspectral imaging, which measures the amount of light in a large number of different frequency bands. Like polarimetric imaging, this too has a wide variety of uses including ecology [9, 10], geology [11, 12], gaseous plume detection and characterization [13, 14], and medicine [15, 16] to name a few. The amount of light in each band is compared and this data can be manipulated to find groups of pixels in a scene that are likely made of similar materials. With careful calibration, material properties, such as reflectivity and emissivity, can be determined spectrally. This information can be compared with known spectral reflectances of materials to identify the material. For this research, measurements are taken in the Long-Wave Infrared (LWIR), sometimes referred to as the Thermal Infrared, part of the electromagnetic spectrum, specifically from 875-1250 cm^{-1}.

One potential issue with using reflectivity or emissivity to classify materials is that these quantities vary with viewing angle. [17, 18, 19, 20, 21] If the viewing angle is varying, this means that a single reference spectrum can no longer adequately describe the target. Instead, a group of target signatures — commonly referred to as a subspace — is used to classify a material. A problem arises, however, when deal-

ing with spectrally similar materials because these subspaces can "overlap" making classification difficult.

Another issue with purely hyperspectral techniques is that the reflectivity and emissivity of a material are dependent on polarization. Unless the hyperspectral sensor is polarimetrically calibrated, which is unlikely, there can be errors in measured reflectances, even with perfect radiometric calibration. This idea will be discussed in detail later.

By combining these two common, but traditionally separate, remote sensing modalities into one polarimetric-hyperspectral (P-HSI) dataset, there is potential to improve on existing material identification techniques. Specifically, the goal of this research will be to determine if index of refraction can be measured remotely without the need for detailed and highly accurate knowledge of scene characteristics, which is required by existing index of refraction retrieval techniques. Index of refraction is a desirable quantity for material identification because, unlike reflectivity or emissivity, it is invariant to viewing geometry for most of materials of interest in remote sensing. This means that not only can a single reference spectrum be used to identify a material regardless of viewing geometry, but additionally multiple viewing geometries can be used to help improve the classification accuracy. Other potential benefits of exploiting this full P-HSI dataset, such as 3D scene reconstruction, are also discussed.

1.1 Document Outline

First, the theory and mathematical framework for this research will be presented. This section will walk through what is essentially the forward model for this research, examining how index of refraction can be used to determine measured polarized radiance values. The goal of this research is to reverse this process, taking polarized radiance measurements and solving for index of refraction, as well as some scene pa-

rameters. Also as part of this section, the current calibration procedure for our P-HSI sensor will be described. Following the theory section, some of the previous work on topics relevant to this work will be discussed. The focus will be on techniques for material identification, but other topics such as target detection, and shape estimation will be touched on as well because they are closely related to this work. Next, the actual retrieval routine will be described showing how P-HSI data is manipulated to estimate index of refraction. Then, results from a variety of both measured and simulated data will be shown and analyzed. Finally, a brief summary of the work will be given in the last section.

II. Theory

The intent of the first part of this chapter is to develop a forward model for how fundamental material, and scene, properties will affect the observed polarized radiance signature from a target. It is important to develop this understanding because the primary goal of this research to follow will be to invert this process, using measured polarimetric radiance values to determine material composition and scene conditions. After this, a brief overview of ellipsometry, which is closely related to this research, will be given. While ellipsometry is traditionally done in a laboratory setting, the goal of this research is to estimate index of refraction from a remote observation platform, without an active illumination source. The final part of the chapter provides a synopsis of the instrument used to collect the data presented in Chapter V, as well as the technique used to calibrate the instrument.

2.1 Dielectric Constant and Index of Refraction

The first step to interpreting the radiance signature of a target is to understand how light interacts with a material. An understanding of fundamental material properties can be developed by starting with Maxwell's equations in matter:

$$
\begin{aligned}
\text{Gauss's Law:} && \nabla \cdot \vec{D} &= \rho_f \\
\text{Gauss's Law for Magnetism:} && \nabla \cdot \vec{B} &= 0 \\
\text{Faraday's Law:} && \nabla \times \vec{E} &= -\frac{\partial \vec{B}}{\partial t} \\
\text{Ampere's Law w/ Maxwell's additon:} && \nabla \times \vec{H} &= \frac{\partial \vec{D}}{\partial t} + \vec{J}_f,
\end{aligned}
\tag{1}
$$

where; $\vec{E}$ is the electric field, $\vec{B}$ is the magnetic field, and ρ_f is the free charge density. $\vec{D} = \varepsilon_0 \varepsilon_r \vec{E}$, $\vec{H} = \frac{B}{\mu_0 \mu_r}$, and $\vec{J}_f$ is the free current density equal to $\sigma \vec{E}$. σ is the conductivity of the material, ε_0 and μ_0 are the permittivity and permeability of

5

free space, ε_r and μ_r are the permittivity and permeability of the material relative to free space. For the purpose of this research, it is assumed that non-magnetic materials are being examined; namely $\mu_r = 1$. ε_r is referred to as the relative dielectric constant of the material [22].

Taking the curl of Faraday's Law gives

$$
\begin{aligned}
\nabla \times \nabla \times \vec{E} &= -\frac{\partial}{\partial t} \nabla \times \vec{B} \\
\nabla^2 \vec{E} &= \sigma \mu_0 \frac{\partial \vec{E}}{\partial t} + \mu_0 \varepsilon_0 \varepsilon_r \frac{\partial^2 \vec{E}}{\partial t^2}.
\end{aligned}
\tag{2}
$$

Note that it is assumed $\rho_f = 0$, which has been previously demonstrated to be a safe assumption [23]. Supposing a plane wave solution for the electric field, that is to say an $\vec{E}$ such that

$$
\vec{E} = \vec{E}_0 e^{i(k\vec{r} - \omega t)},
\tag{3}
$$

it can be derived that

$$
k^2 = \sigma \mu_0 \omega i + \mu_o \varepsilon_0 \varepsilon_r \omega^2.
\tag{4}
$$

The index of refraction is defined as the ratio of the velocity of light in vaccuum to the velocity of light in the material. The speed of light is given as ω/k. Solving Faraday's Law in vaccuum, shows that the speed of light in vaccuum is $c = \sqrt{\frac{1}{\mu_0 \varepsilon_0}}$. With this information, the index of refraction can be determined:

$$
\tilde{N}^2 = \frac{\sigma}{\varepsilon_0 \omega} i + \varepsilon_r = \tilde{\varepsilon}_r.
\tag{5}
$$

$\tilde{\varepsilon}_r$ is referred to as the *complex* relative dielectric constant. For simplicity, an ε_1 can be defined as the real part of the complex dielectric constant and ε_2 as the imaginary part. Similarly, complex index of refraction can be defined in terms of a real and

imaginary component, $\tilde{N} = n + i\kappa$. Expanding Equation (5) shows

$$
\begin{aligned}
\varepsilon_1 &= n^2 - \kappa^2 \\
\varepsilon_2 &= 2n\kappa.
\end{aligned}
\tag{6}
$$

Solving for n and κ gives:

$$
\begin{aligned}
n &= \tfrac{1}{\sqrt{2}}\sqrt{\varepsilon_1 + \sqrt{\varepsilon_1^2 + \varepsilon_2^2}} \\
\kappa &= \tfrac{1}{\sqrt{2}}\sqrt{-\varepsilon_1 + \sqrt{\varepsilon_1^2 + \varepsilon_2^2}}.
\end{aligned}
\tag{7}
$$

These quantities are often useful in characterizing properties of materials such as surface reflectance, which is described by the Fresnel equations.

2.2 Lorentz Oscillator Model

Another classical model of the complex dielectric constant is the Lorentz oscillator model. This model treats the bonds in a lattice as a series of driven, damped springs. The equation of motion for an electron in this configuration is

$$
m_e \ddot{\mathbf{x}} + 2\pi m_e \Xi \dot{\mathbf{x}} + 4\pi^2 m_e \nu_0^2 \mathbf{x} = -e\mathbf{E}_{loc}.
\tag{8}
$$

m_e is the mass and e is the charge of an electron. Bold face is used here to denote a vector instead of an arrow to avoid overlap with the dots, which represent time derivatives. The first and third terms are the classic harmonic oscillator, the second term is the damping term and the final term is the driving force. $\mathbf{E}_{loc}$ is assumed to be equal to the incident electric field perturbing the system. Ξ is a the collision frequency and is defined $\Xi = 1/2\pi\bar{t}$, where $\bar{t}$ is the mean time between collisions of an electron with the lattice. ν_0 is the resonant frequency of the oscillator [24].

Assuming a periodic solution for both $\mathbf{x}$ and $\mathbf{E}$ gives

$$-4\pi^2\nu^2 m_e\mathbf{x} - 4\pi^2 im_e\Xi\nu\mathbf{x} + 4\pi^2 m_e\nu_0^2\mathbf{x} = -e\mathbf{E}, \tag{9}$$

which can be rearranged to give

$$\mathbf{x}_0 = \frac{e}{4\pi^2 m_e}\frac{1}{\nu_0^2 - \nu^2 - i\Xi\nu}\mathbf{E}_0. \tag{10}$$

This means the incident electric field generates an effective dipole, which polarizes the material. The electric displacement can be expressed: $\mathbf{D} = \varepsilon_0\mathbf{E} + \mathbf{P}$, where $\mathbf{P}$ is the polarization. The polarization is defined as the total dipole moment generated:

$$\mathbf{P} = Ne\mathbf{x} = \frac{Ne^2}{4\pi^2 m_e}\frac{1}{\nu_0^2 - \nu^2 - i\Xi\nu}\mathbf{E}. \tag{11}$$

N is the number of free electrons per unit volume. As stated in the previous section, electric displacement can also be expressed $\mathbf{D} = \varepsilon_0\varepsilon_r\mathbf{E}$. Equating these two expressions for displacement and plugging in Equation (11), gives an expression for the dielectric constant:

$$\varepsilon_r(\nu) = \varepsilon_\infty + \frac{Ne^2}{4\pi^2 m_e\varepsilon_0}\frac{1}{\nu_0^2 - \nu^2 - i\Xi\nu} = \varepsilon_\infty + \frac{\nu_p^2}{\nu_0^2 - \nu^2 - i\Xi\nu}, \tag{12}$$

where ν_p is called the plasma frequency. ε_∞ represents the limit of the dielectric constant far away from the resonant frequency. The real and imaginary components are then

$$\begin{array}{rcl}
\varepsilon_1 & = & \varepsilon_\infty + \frac{\nu_p^2(\nu_0^2 - \nu^2)}{(\nu_0^2 - \nu^2)^2 + \Xi^2\nu^2} \\[2mm]
\varepsilon_2 & = & \frac{\nu_p^2\Xi\nu}{(\nu_0^2 - \nu^2)^2 + \Xi^2\nu^2}.
\end{array} \tag{13}$$

From this, the index of refraction can be solved for using Equation (7). The model

8

can also be extended to account for multiple resonances by summation:

$$\varepsilon_r(\nu) = \varepsilon_\infty + \nu_p^2 \sum_{j=1}^{J} \frac{f_j}{\nu_j^2 - \nu^2 - i\Xi_j\nu}. \tag{14}$$

f_j is the relative strength of the jth resonance, and is normalized such that

$$\sum_{j=1}^{J} f_j = 1. \tag{15}$$

The interesting thing about this model is that the dielectric constant for many differ-
ent wavelengths of incident light can be described using only a few parameters. With
this model, a large number of spectral measurements can be described by $3J + 1$
parameters. If J is small enough, this means the index of refraction at every spectral
point measured can be described by fewer parameters than there are measurements,
making the determination of index of refraction an overdetermined problem. Over
the spectral bandwidths measured for this work, it is unlikely that a material will
have more than a couple resonances that will contribute significantly to the dielec-
tric constant. The hope is that this will allow additional parameters, such as surface
temerature and downwelling radiance, to be solved for as well while ensuring the prob-
lem is still overdetermined. To accomplish this, however, it is necessary to determine
how these parameters will affect the radiance arriving at the sensor.

2.3   Fresnel's Equations

The Fresnel equations were derived by Augustin-Jean Fresnel in 1821 to describe
the behavior of a plane wave at a perfectly flat, infinitely large boundary between
two materials. They relate the reflectance and transmittance of an electric field
at the interface, based on the orientation of the its electric field, to the index of

refraction of both materials and the angle of incidence of the incoming light, θ_i. This research focuses on specular materials so the assumptions of the Fresnel equations are valid. For rough surfaces, a more detailed model of the reflection, perhaps a pBRDF, would be necessary. As stated before, it is also presumed that $\mu = \mu_0$. With these assumptions, the Fresnel reflection coefficients are [25]:

$$
\begin{aligned}
r_s &= \frac{\tilde{N}cos\theta_i - \sqrt{1 - \tilde{N}^2 sin^2\theta_i}}{\tilde{N}cos\theta_i + \sqrt{1 - \tilde{N}^2 sin^2\theta_i}} \\
r_p &= \frac{cos\theta_i - \tilde{N}\sqrt{1 - \tilde{N}^2 sin^2\theta_i}}{cos\theta_i + \tilde{N}\sqrt{1 - \tilde{N}^2 sin^2\theta_i}}
\end{aligned}
\tag{16}
$$

Again, $\tilde{N}$ is used to denote the complex index of refraction, as opposed to n, which represents only the real part. Subscript s denotes electric field oscillating perpendicular (*senkrecht* in German) to the plane of reflectance, while subscript p denotes the electric field in the plane of reflectance.

Because the electric field oscillates so quickly, it is impossible for a sensor to directly measure it. Instead, a sensor will measure intensity, which is defined as the modulus squared of the field strength. Thus, the actual reflectivity of a material is the modulus squared of the Fresnel reflection coefficients. Figure 1 shows how the polarized reflectances can vary with angle.

This indicates index of refraction can be determined from polarized reflectance or emissivity measurements, for smooth surfaces, using the Fresnel equations. Because this work is done in the LWIR, most surfaces will appear tolerably smooth relative to the wavelength of light interacting with them. The last step in determining how polarized radiance measurements map to index of refraction is to understand how reflectance and emissivity factor into the measured radiance from a target.
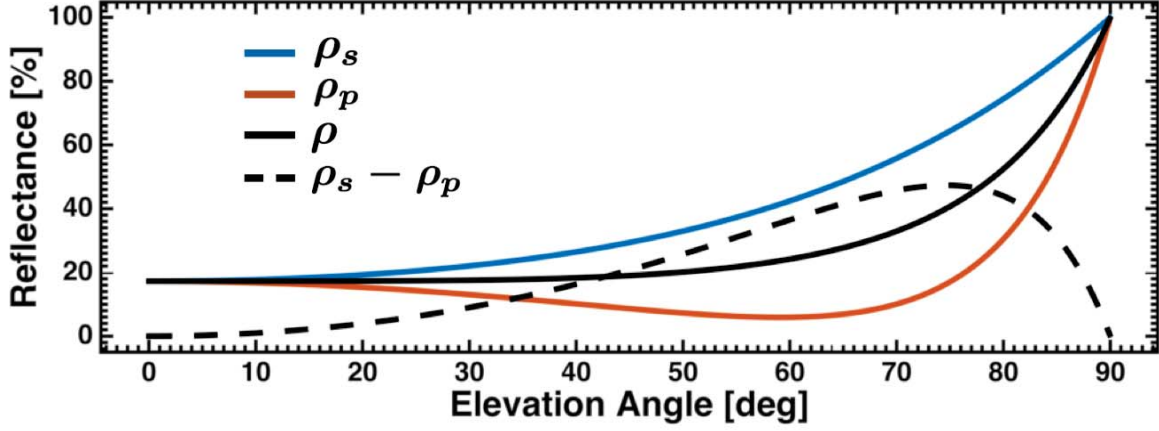
Figure 1. Plot of s- and p-pol reflectances as a function of viewing angle for $n = 1.5$ and $\kappa = 1$. The dip in the p-pol reflectance, and usually the maximum polarization, occurs at Brewster's angle. For a purely real index of refraction, the p-pol reflectance will drop to zero at this angle. Both polarization states will always have identical reflectances at normal viewing angle and unit reflectance at an angle of $\frac{\pi}{2}$.

2.4 Observed Radiance

In the LWIR, radiance measured by the sensor comes from three principal sources: radiance emitted from the surface of the target, downwelling radiance being reflected off the target, and radiance generated by the atmosphere along the line-of-sight to the target. Figure 2 shows a basic schematic of this.
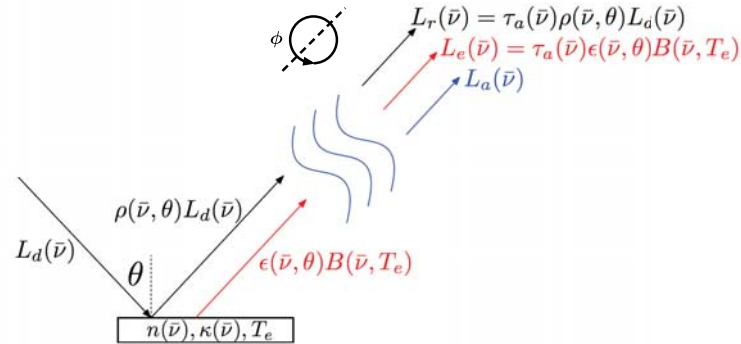
Figure 2. Basic schematic showing the sources of radiance arriving at the sensor.

For this work, it is assumed the object being observed is opaque in the LWIR. There are certain materials which are transmissive in this spectral region; but, the majority of potential targets of interest for remote sensing are not. Radiance from the first two sources must be transmitted through the atmophere. In total, the radiance arriving at the sensor can be expressed:

$$L_{sens}(\bar{\nu}, \theta) = \tau_a(\bar{\nu}) \left[\epsilon(\bar{\nu}, \theta) B(\bar{\nu}, T_e) + \rho(\bar{\nu}, \theta) L_d(\bar{\nu}) \right] + L_a(\bar{\nu}). \tag{17}$$

θ denotes the elevation angle of the sensor relative ot the surface, $\epsilon(\bar{\nu}, \theta)$ is the spectral emissivity of the material, $\rho(\bar{\nu}, \theta)$ is the reflectance, $B(\bar{\nu}, T_e)$ represents blackbody radiance at the temperature of the object, T_e. L_d is the downwelling radiance, L_a is the path radiance, and τ_a is the transmission of the atmosphere along the line-of-sight. For an opaque material in thermal equilibrium, $\epsilon(\bar{\nu}, \theta) = 1 - \rho(\bar{\nu}, \theta)$ [26]. So, Equation (17) can be rewritten as

$$L(\bar{\nu}, \theta) = \tau_a(\bar{\nu}) \left[\rho(\bar{\nu}, \theta) \left[L_d(\bar{\nu}) - B(\bar{\nu}, T_e) \right] + B(\bar{\nu}, T_e) \right] + L_a(\bar{\nu}). \tag{18}$$

This is purely a hyperspectral measurement, however, and polarization has not been accounted for.

As revealed by the Fresnel equations, a surface's reflectance, and thus emissivity, is polarization dependent. A polarimetric sensor will measure both the s-pol and p-pol radiances, which can be expressed

$$
\begin{aligned}
L_s(\bar{\nu}, \theta) &= \tau_a(\bar{\nu}) \left[\rho_s(\bar{\nu}, \theta) \left[\frac{L_d(\bar{\nu})}{2} - \frac{B(\bar{\nu}, T_e)}{2} \right] + \frac{B(\bar{\nu}, T_e)}{2} \right] + \frac{L_a(\bar{\nu})}{2} \\
L_p(\bar{\nu}, \theta) &= \tau_a(\bar{\nu}) \left[\rho_p(\bar{\nu}, \theta) \left[\frac{L_d(\bar{\nu})}{2} - \frac{B(\bar{\nu}, T_e)}{2} \right] + \frac{B(\bar{\nu}, T_e)}{2} \right] + \frac{L_a(\bar{\nu})}{2}.
\end{aligned}
\tag{19}
$$

This presumes that the downwelling radiance, path radiance, and transmittance of

the atmosphere are all unpolarized, which has been shown to be a valid assumption in the LWIR[27].

If accurate information about atmospheric, scene, and object parameters, is available, ρ_s and ρ_p can be directly calculated. In practice this is difficult, but the hope of this research is to estimate these parameters to sufficient accuracy using only the data and reasonable assumptions about the scene. If the angle of the surface relative to the sensor is known, the complex index of refraction of the material can be calculated from one viewing angle, whereas two measurements, at different angles, would be required for an instrument unable to measure polarization.

Another interesting consequence of this derivation is that it demonstrates the potential for a fundamental error to be introduced into the reflectance calculation if polarization effects are not properly accounted for. Hyperspectral material classification approaches often attempt to calculate the unpolarized reflectance or emissivity of a material, given

$$\rho = \frac{\rho_s + \rho_p}{2} \;\;, \;\; \text{or} \;\; \epsilon = \frac{\epsilon_s + \epsilon_p}{2}, \tag{20}$$

where subscript s and p are the polarization states. If a source is polarized, this can introduce an error into unpolarized measurements of reflectance. Any sensor will have some polarimetric bias; that is to say, one polarization state has a larger relative proportion of light transmitted through the system optics. Hyperspectral systems in the LWIR are almost always calibrated using blackbodies, which are unpolarized, so accounting for this polarization-dependent gain is impossible. A polarized sensor allows radiance in each polarization state to be separately calibrated allowing for a more accurate reflectance measurement. This can be illustrated with a simple example.

Assume a noise-free scenario where a $100°C$ blackbody is reflecting off a smooth surface, $n = 1.5$ and $\kappa = 1$, at an angle of 70 degrees. Based on previously

13

measured data, the band-averaged gain of the Telops Hypercam varies from $2.66 *$
$10^9 \frac{DN}{\frac{W}{cm^2 srcm^{-1}}}$ to $2.18 * 10^9 \frac{DN}{\frac{W}{cm^2 srcm^{-1}}}$ depending on polarizer angle. With these param-
eters, a polarization-agnostic gain is used, the measured reflectance would be

$$\rho = \frac{G_s L_s + G_p L_p}{G_{avg} B(100°C)} = \frac{G_s \rho_s \frac{B(100°C)}{2} + G_p \rho_p \frac{B(100°C)}{2}}{G_{avg} B(100°C)} = \frac{G_s \rho_s + G_p \rho_p}{G_s + G_p} = 0.352. \quad (21)$$

The true reflectance for a material with these parameters is 0.329. The error will
impede the ablility of a hyperspectral-only sensor in distinguishing two spectrally
similar materials. By incorporating a polarization component, true reflectance of the
material can be accurately measured in both polarization states leading to more ac-
curate reflectivity or emissivity retrievals. This error becomes particularly important
at far off-nadir viewing geometries as the polarization component is larger relative to
the near-nadir case.

2.5 Stokes Vector

The Stokes vector is a mathematical way of describing the polarization state of
light. In general, there are four quantities: S_0, S_1, S_2, and S_3. Traditionally, these
are represented in vector form, and the collection is known as a Stokes vector. S_0
represents the total radiance regardless of polarization state. S_1 is the difference
between the intensity of vertically (0°) and horizontally (90°) polarized light. S_2
denotes the difference between light polarized at 45° versus -45°. Note that -45° is
equivalent to 135°, in fact, all angles are equivalent to the angles that are multiples
of 180° greater or less than themselves. S_3 represents the difference between right-
and left-handed circular polarization. It is impossible to measure circular polarization
with only a linear polarizer, therefore, the sensor used for this research cannot measure

this quantity. This is not an issue, however, since circular polarization is almost alway negligible in remote sensing [28].

The Stokes parameters can be used to calculate useful terms describing the amount and direction of polarization in a scene. The two most common of these are Degree of Linear Polarization (DoLP) and Angle of Polarization (AoP). The DoLP is expressed:

$$DoLP = \frac{\sqrt{S_1^2 + S_2^2}}{S_0}.$$ (22)

As the name suggests, DoLP is a measure of how linearly polarized something is, which can be useful in identifying the material and/or in determining the elevation angle of a material relative to the sensor. AoP is defined as:

$$AoP = \tan^{-1} \frac{S_2}{S_1}.$$ (23)

This quantity denotes the angle between the plane of reflectance and the zero degree polarizer angle in the instrument reference frame.

Using the description of at-sensor radiance described in the previous section, an equation expected Stokes parameters can be derived.

$$S_0(\bar{\nu}, \theta) = L_s(\bar{\nu}, \theta) + L_p(\bar{\nu}, \theta) =$$
$$\tau_a(\bar{\nu}) \left[(\rho_s(\bar{\nu}, \theta) + \rho_p(\bar{\nu}, \theta)) \left[\frac{L_d(\bar{\nu})}{2} - \frac{B(\bar{\nu}, T_e)}{2} \right] + B(\bar{\nu}, T_e) \right] + L_a(\bar{\nu}),$$ (24)

which simplifies to Equation (18).

In order to solve for reflectance, both $L_d(\bar{\nu})$ and $B(\bar{\nu}, T_e)$ must be determined at every spectral point, but both can be modeled by fewer parameters than the number of spectral measurements. The $B(\bar{\nu}, T_e)$ term is defined solely by the temperature of the surface. The downwelling radiance can either be modeled or measured. Many atmospheric models exist which can be fed weather conditions such as humidity, tem-

15

perature, and atmospheric pressure. These parameters can be left as unknowns and fit using the measured radiance data or potentially measured by weather instruments. These estimates of atmospheric parameters can also be used to calculate $L_a(\bar{\nu})$. With this notation, and assuming $AoP = 0$, S_0 and S_1 can be expressed as

$$S_0(\bar{\nu}, \theta) = \tau_a(\bar{\nu}) \left[\tfrac{1}{2} \left(\rho_s(\bar{\nu}, \theta) + \rho_p(\bar{\nu}, \theta)\right) \left(L_d(\bar{\nu}) - B(\bar{\nu}, T_e)\right) + B(\bar{\nu}, T_e)\right] + L_a(\bar{\nu})$$

$$S_1(\bar{\nu}, \theta) = \tfrac{1}{2}\tau_a(\bar{\nu}) \left(\rho_s(\bar{\nu}, \theta) - \rho_p(\bar{\nu}, \theta)\right) \left(L_d(\bar{\nu}) - B(\bar{\nu}, T_e)\right).$$

$$(25)$$

This derivation can also be expressed in Mueller matrix form. Because it is presumed that the circular polarization is zero for targets of interest, only the 3x3 Mueller matrix is used. The Mueller matrix for Fresnel reflection — again when $AoP = 0$ — is defined as [27]:

$$\hat{F} = \begin{bmatrix} r_s r_s^* + r_p r_p^* & r_s r_s^* - r_p r_p^* & 0 \\ r_s r_s^* - r_p r_p^* & r_s r_s^* + r_p r_p^* & 0 \\ 0 & 0 & 2Re\left\{r_s r_p^*\right\} \end{bmatrix} = \begin{bmatrix} \rho_s + \rho_p & \rho_s - \rho_p & 0 \\ \rho_s - \rho_p & \rho_s + \rho_p & 0 \\ 0 & 0 & 2Re\left\{r_s r_p^*\right\} \end{bmatrix}$$

$$(26)$$

The Stokes vector arriving at the sensor can then be expressed:

$$\vec{S} = \frac{1}{2}\left[\tau_a\left[\hat{F}\begin{pmatrix} L_d \\ 0 \\ 0 \end{pmatrix} + \left(1 - \hat{F}\right)\begin{pmatrix} B(T_e) \\ 0 \\ 0 \end{pmatrix}\right] + \begin{pmatrix} L_a \\ 0 \\ 0 \end{pmatrix}\right].$$

$$(27)$$

This simplifies to Equation 25 with a little algebra. Both of these derivations, however, assume $AoP = 0$. It is also necessary to consider when the sensor zero degree polarizer angle is not aligned in the plane of reflectance. As the sensor rotates about its optical axis, the relative quantites of S_1 and S_2 change. With this consideration the complete

Stokes vector can be described:

$$\vec{S} = \begin{pmatrix} \tau_a(\bar{\nu}) \left[\frac{1}{2} \left(\rho_s(\bar{\nu}, \theta) + \rho_p(\bar{\nu}, \theta) \right) \left(L_d(\bar{\nu}) - B(\bar{\nu}, T_e) \right) + B(\bar{\nu}, T_e) \right] + L_a(\bar{\nu}) \\ \frac{1}{2} \tau_a(\bar{\nu}) \left(\rho_s(\bar{\nu}, \theta) - \rho_p(\bar{\nu}, \theta) \right) \left(L_d(\bar{\nu}) - B(\bar{\nu}, T_e) \right) \cos 2\phi \\ \frac{1}{2} \tau_a(\bar{\nu}) \left(\rho_s(\bar{\nu}, \theta) - \rho_p(\bar{\nu}, \theta) \right) \left(L_d(\bar{\nu}) - B(\bar{\nu}, T_e) \right) \sin 2\phi, \end{pmatrix} \quad (28)$$

where ϕ is the AoP.

2.6 Ellipsometry

Ellipsometry is a technique that seeks to measure material properties, namely the complex index of refraction, by observing changes in the polarization state of light when reflected off the material surface. Ellipsometry can be used for other applications as well, such as estimating the thickness of a thin film of material on a bulk substrate, but these are outside the scope of this project and thus won't be discussed here. The name ellipsometry derives from the ellipse that is formed over time when observing x- and y-components of electric field at a fixed position. Analyzing the polarization ellipse requires that both the phase and amplitude of the components of the electric field be measured. The fundamental equation of ellipsometry is

$$\rho_e = \frac{r_p}{r_s} = \tan \psi e^{i\Delta}, \quad (29)$$

where r_p and r_s are the Fresnel reflection coefficients expressed above. $\tan \psi$ represents the amplitude of the complex reflectance ratio, ρ_e, and Δ is the phase. [29]

There are many different varieties of ellipsometer, one of the most basic is the null ellipsometer. This uses either the PCSA (Polarizer-Compensator-Sample-Analyzer) or PSCA (Polarizer-Sample-Compensator-Analyzer) configuration. The compensator is usually a quarter-wave plate. The polarizer is adjusted such that the sample is

17

illuminated with elliptically polarized light in such a way that the reflected light is linearly polarized. The reflected light can then be completely blocked by the analyzer, giving the "null" condition. It is important to properly search the parameter space, because numerous "pseudo-nulls", i.e. local minima, may be present. Based on the orientation of the polarizer, quarter-wave plate and analyzer at the null condition, ψ and Δ can be calculated. From there, the Fresnel reflection coefficients can be determined and index of refraction can be solved for. [30]

In this work, a JA Woollam [31] rotating analyzer ellipsometer was used to determine the "true" index of refraction to compare against. A rotating analyzer ellipsometer works by illuminating a target with linearly polarized light generate by passing light from an unpolarized source through a linear polarizer. The light reflected off the sample will be elliptically polarized. The analyzer portion of the instrument is continuously rotated to measure the elliptical polarization. A Fourier transform spectrometer (see next section for more information) is used to measure the spectral variations of the polarization signature being analyzed. To mitigate the effects of noise, different models are used to describe the spectral variation of the ellipsometry measurements. The model used will depend on the type of material being observed. Additionally, multiple measurements can be taken from multiple viewing angles to further constrain the solution.

2.7   IFTS

Imaging Fourier Transform Spectrometers (IFTS) capture an image of a scene with spectral information at each pixel. Essentially, the system can be described as a broadband camera viewing a scene through a Michelson interferometer. A Michelson interferometer passes incoming light through a beam splitter, where it is partially reflected and partially transmitted through. Each beam is then reflected off of a

mirror and passes through the beam splitter again. The two beams recombine and interfere with one another. One of the mirrors is fixed while the other is moved and images of the scene are taken at a number of different, equally spaced mirror positions. As the mirror moves, the two beams will travel different path lengths. A schematic of this is shown in Figure 3.
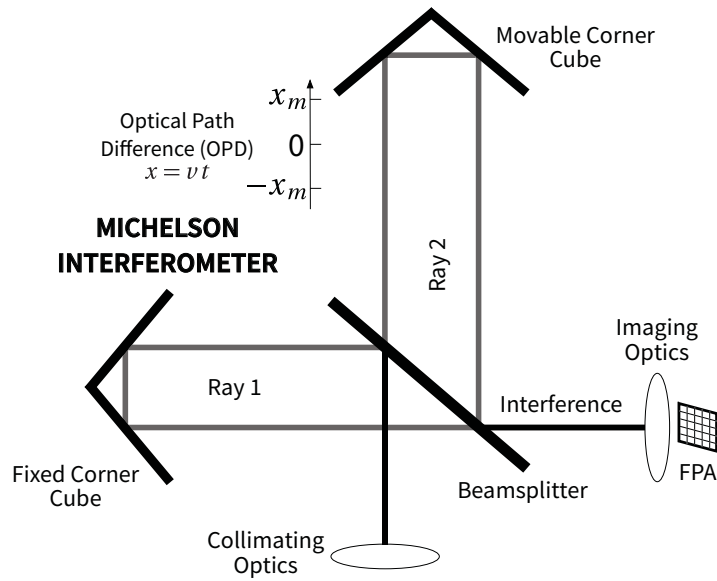
Figure 3. Basic schematic of an imaging Michelson interferometer. Incoming light is split into two beams, then each beam is reflected off a mirror. The difference between the distance the two beams travel determines how they interfere when recombined. A camera image is taken at a number of different optical path differences to generate an interferogram at each pixel.

When the path difference is an integer multiple of wavelength, light at that wavelength will constructively interfere; when path difference is a half integer multiple, light will destructively interfere. For a single wavelength, this will create a sinosoidal pattern in time as the mirror is moved. Broadband light contains a continuum of

different wavelengths each with a different sinosoidal frequency. The combination of these sinosoids generates what is known as an interferogram. Peak intensity occurs when both mirrors are equidistant from the beam splitter. At this point, known as the zero path difference (ZPD) point, light of all wavelengths constructively interfere. The further from ZPD the mirror scans, the greater the spectral resolution that can be measured.

Taking the Fourier transform of this interferogram gives the amplitude of sinosoidal functions, at a number of different frequencies, required to produce the interferogram. This gives the spectrum of the light as measured by the detector. Because the camera responds differently to different wavelengths, this is not necessarily the spectrum of the light arriving at the focal plane. Additionally, in the LWIR, the instrument itself is emitting light that is measured by the camera. To compensate for these effects, and recover the radiance arriving at the instrument aperture, a calibration must be performed.

2.8 Instrument Calibration

To understand instrument calibration, it is first necessary to understand how the detector actually measures radiance. Integrating over the projected area of the source gives a radiant intensity, I, which gives energy arriving at the detector per solid angle. For extended objects, the solid angle is dependent on the optics of the sensor and the size of the pixels on the focal plane array (FPA). Integrating intensity over the solid angle gives the energy flux, Φ_e, on a single pixel. Photon flux, Φ_q, can be related to energy flux via dividing by the energy per photon, $E = \frac{hc}{\lambda}$; where λ represents the wavelength of the light being measured. The FPA is composed of a semi-conductor, in the case of the instrument used in this research, Mercury-Cadmium-Telluride (MCT). When a photon with energy greater than the bandgap of MCT hits the FPA, there's

a probability that it will be absorbed, exciting an electron from the valence band to the conduction band in the process. The camera collects photons for a set amount of time, known as the integration time, and the excited electrons are collected in a potential well. The camera measures the number of electrons collected by each pixel to generate an image of the scene. The Telops instrument used in this research uses 16-bit digitization to turn these electrons into digital counts which are stored in image files. The purpose of calibration is to take this measured signal in terms of digital counts and convert it back to a radiance value.

The method for radiometrically calibrating the Telops Hyper-Cam used in this work is outlined in [32]. A measurement of two blackbodies, set to distinct temperatures, is taken immediately after measuring a scene. The blackbody temperatures are chosen so the band-integrated radiance of one blackbody is lower than the scene radiance, while the radiance of the second blackbody is greater. This enables the determination of each pixel's spectral response (G for gain), as well as the self emitted radiance of the instrument ($\mathcal{O}$ for offset):

$$G = \frac{Y_{BB2} - Y_{BB1}}{L_{BB2} - L_{BB1}}$$
$$\mathcal{O} = \frac{Y_{BB2}}{G} - L_{BB2}. \tag{30}$$

Y signifies the digital counts measured by a single pixel and L represents the radiance of the blackbody source being observed. Note that either blackbody can be used in calculating the radiance, but the hotter blackbody is usually chosen because greater radiance generally means a higher signal-to-noise ratio (SNR). The scene radiance can then be expressed:

$$L_{SCN} = \frac{Y_{SCN}}{G} - \mathcal{O}. \tag{31}$$

Figure 4 shows what the image of a sample scene looks like before and after radiometric calibration.
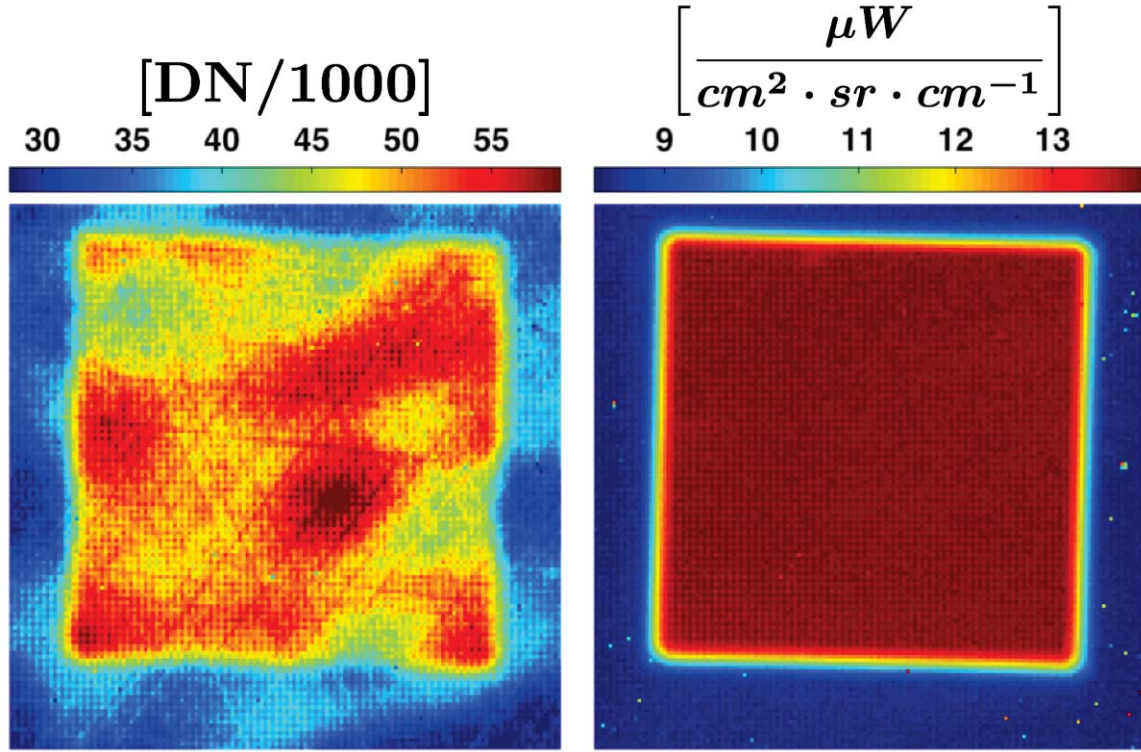
Figure 4. Band-averaged radiance image before (left) and after (right) radiometric calibration using two blackbodies.

Because of the nature of MCT FPA manufacturing, there are a number of "bad" pixels on the array. These pixels may have no response to incident radiation, or they may always be saturated. Additionally, pixels can have brief periods where their gain randomly spikes or dips. To correct for this, pixels that are more than six standard deviations from the mean of the entire image when observing the on-board blackbodies are flagged as bad and corrected. The correction replaces these pixels with an average of their eight nearest neighbor pixels. If one of the nearest neighbors is also a bad pixel, then that pixel is ignored in the averaging. Figure 5 shows a band-averaged radiance image after the bad pixel correction has been applied.

Due to unknown effects, potentially from the Read-out Integrated Circuit (ROIC), a checkerboard-like pattern is visible in broadband radiance images, shown in Figure 4. This effect is magnified when observing polarimetric quantites, because differences
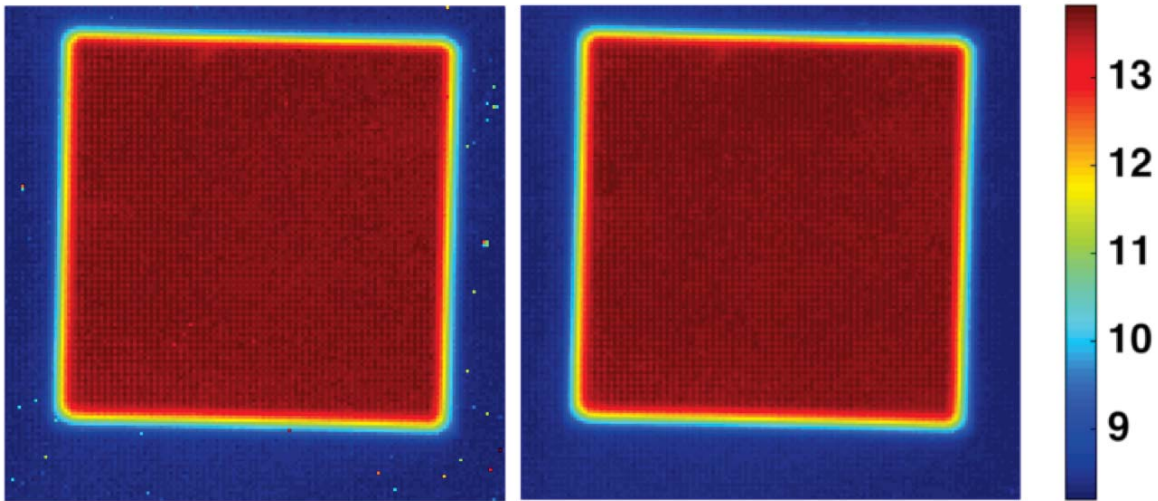
Figure 5. Band-averaged radiance image before and after bad pixel correction.

of radiance measurements are taken, meaning small relative changes in radiance can become large relative to the polarimetric signature of objects being observed. In order to mitigate this issue, a Gaussian notch filter is applied to the radiance images. The 2-D FFT of the image is multiplied by a filter which reduces the effects of high frequency vertical, horizontal, and diagonal components. Then, the inverse FFT is taken to recover the original image without the checkerboard. This does reduce the spatial resolution of the image, but for most applications in this research, spatial resolution is not the primary concern. Figure 6 shows the original image, 2-D FFT of the original image, filter used, and the corrected image.

Because the back surface of the polarizer used in the sensor is not perfectly flat, the image of a scene moves on the FPA as the polarizer rotates. The effect is small, usually only a couple pixels, but without correction, this creates a large, artificial polarization signature near the edges of objects in a scene. To correct for this, an image registration technique is implimented which minimizes the difference between
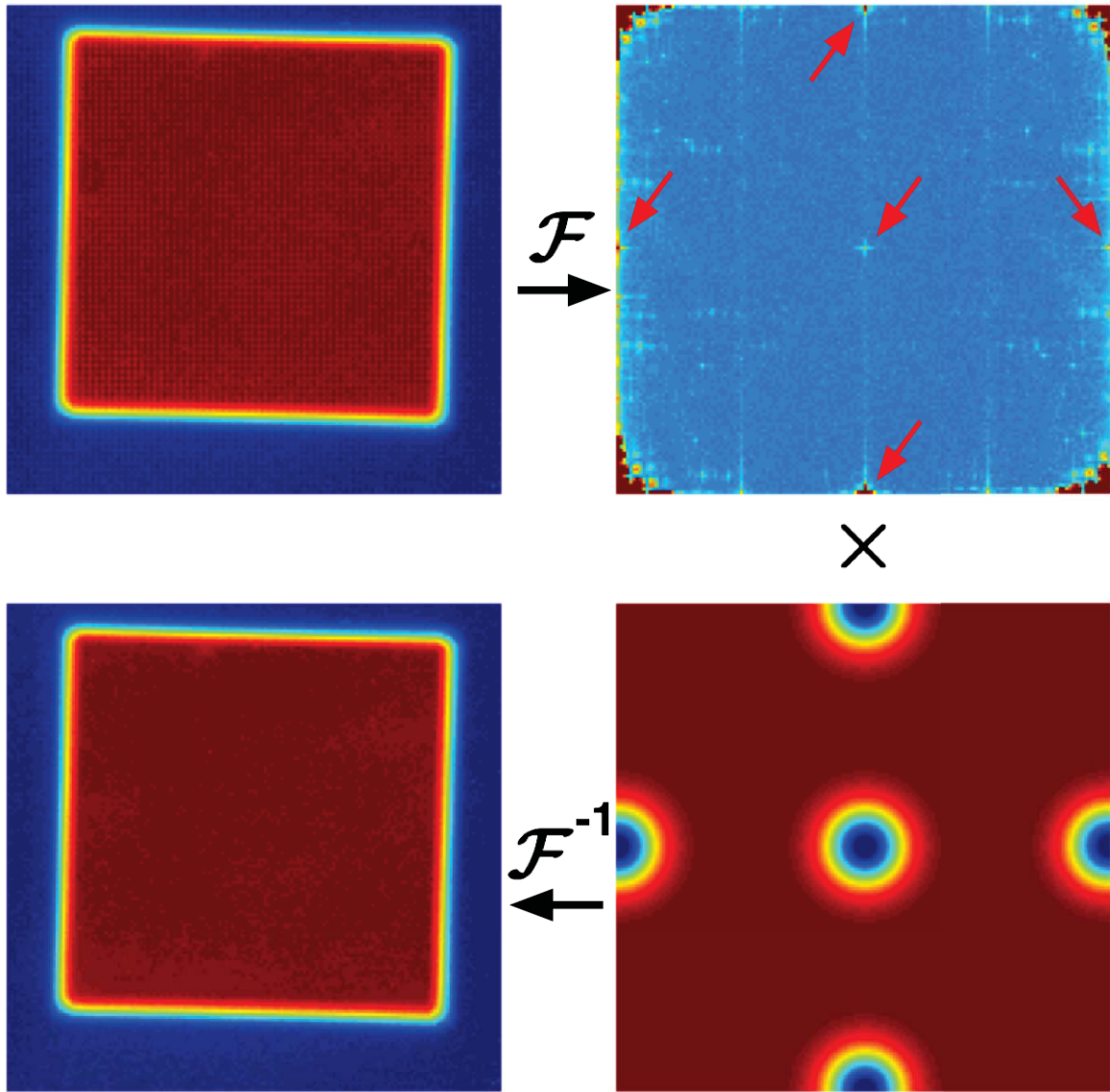
Figure 6. Band-averaged radiance image with checkerboard is shown in the upper left. The 2-D Fourier transform of the image is shown in the upper right. The red arrows denote peaks which are artifacts of the checkerboard pattern. The lower right shows the mask (blue is zero, red is 1) that is multiplied by the Fourier transform of the original image. The inverse Fourier transform is then taken to get the final image with the checkerboard pattern removed shown in the lower left.

two S_0 measurements. As the polarizer rotates, a particular point in the scene should trace out a circle on the FPA. By solving for how much to shift the S_0 images, in order to minimize the difference between the two, the radius and phase of this shift can be determined. This is used to register each polarizer angle image back to the 0 degree polarizer angle image. Figure 7 shows what the S_1 image of a scene looks like before and after image registration.

In addition to a radiometric calibration, the polarimetric response of the instrument must also be calibrated. Assuming the linear polarizer mounted to the front of the instrument is ideal, the radiometric calibration described above, performed at each polarizer angle measured, is sufficient [33]. The polarizer is not ideal, however, so an additional calibration is needed. Unlike the radiometric calibration, which is done for every test, polarimetric calibration only needs to be done once. This work was partially completed by Capt. Joel Holder [34] using a method for calibrating polarimeters outlined in [35].

The concept is to send known polarization states into the instrument and determine the polarization state measured by the instrument. Measurements of N unique, and known, scenes are taken at M different polarizer angles. The measured radiances are collected into an $M \times N$ "channel" matrix, L_m. The true Stokes vectors for each scene are collected into a $3 \times N$ matrix, L_s. Note again that the circular polarization component is ignored. The system matrix, W is defined $W = L_m L_s^+$, where L_s^+ is the psuedo-inverse of L_s. The psuedo-inverse of W gives the data reduction matrix R, which is used to calibrate measured channel vectors into calibrated scene Stokes vectors. While this calibration has been done for portions of the FPA, it has yet to be completed for the entire image.
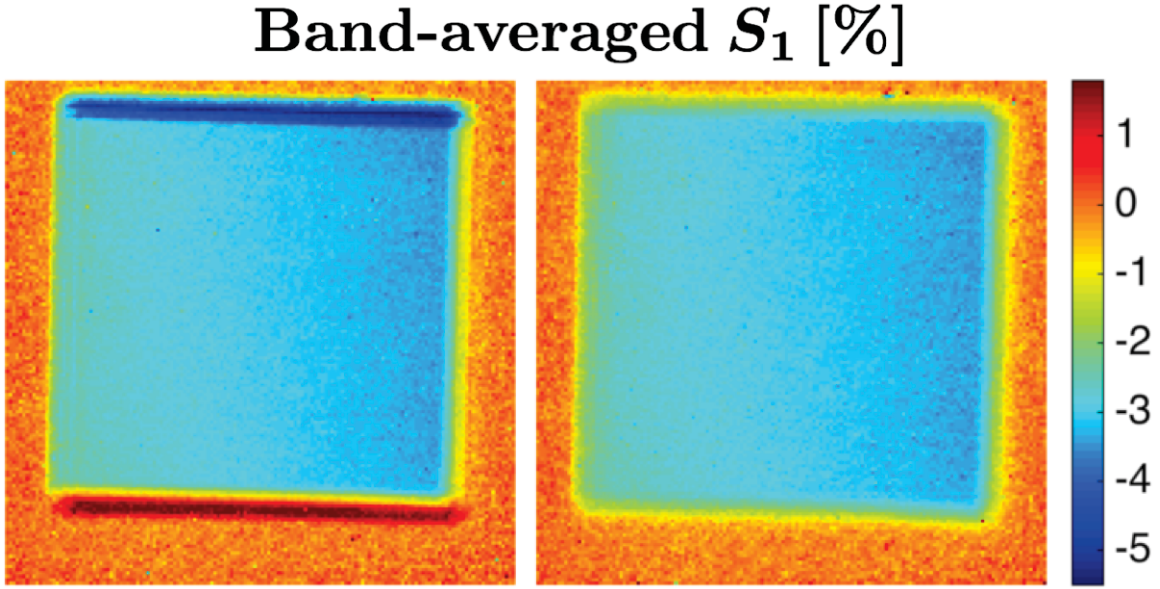
Band-averaged S_1 [%]

Figure 7. Band-averaged S_1 image of a sample scene before (left) and after (right) registering each polarizer angle image together. Note the artificial polarization at the edges of the object in the first image.

2.9 Summary

In this section, the theoretical basis for this work was presented. The primary concept of this work is that by using physics-based models to describe the spectral variation of the index of refraction, the polarimetric-hypspectral radiance can be described using far fewer parameters than the number of spectral bands measured. This work focuses exclusively on smooth surfaces so the Fresnel equations can be used to relate index of refraction to reflectance and emissivity. For rough surfaces, a more detailed reflectance model would be required. Information about the sensor as well as the procedure for calibrating it were also presented in this section.

III. Literature Review

Hyperspectral and polarimetric imaging are both fields which have been extensively studied, with thousands of papers available. Almost all of this work, however, has examined these two modalities independently. The intent of this chapter is to give an overview of some of the most common techniques in both fields, as well as some of the limitations. The chapter starts with a brief overview of disturbed earth detection. This is included because there is another effort, using the same instrument, underway to use the spectral-polarimetric signature of soils to detect recent disturbances. After that is a section reviewing the use of polarimetry for surface normal estimation and 3D scene reconstruction. While the primary focus of this research will assume that scene geometry is known, it is important to understand how scene geometry can affect polarization. Because of the interplay between index of refraction and surface normal angle on the polarimetric signature, this research could be adapted to improve 3D scene reconstruction as well.

Next, some of the common target detection techniques, using hyperspectral or polarimetric imaging, will be reviewed. Target detection can thought of as the first step in material classfication, and work related to this research may enhance target detection. Then, common material classification techniques, again using either hyperspectral or polarimetric imaging, will be described. Finally, some of the existing methods for estimating index of refraction will be discussed. Each of these methods include pieces which will be useful in the index of refraction retrieval technique presented here, but none contain all of the elements incorporated into this research. The primary goal of this research will be to retrieve an index of refraction spectrum without the impractical, and sometimes impossible, *a priori* constraints required by these methods.

3.1 Disturbed Earth

One area of interest for combining polarimetric and hyperspectral imaging has been detecting buried mines and IEDs. Some methods focus on how the spectral and polarimetric signature of ground that has been recent dug up differs from undisturbed soil [36]. It was found that fine grain silicates become less reflective and more emissive in the LWIR silicon dioxide reststrahlen band, which is a spectral feature due to a Lorentz oscillator resonance (see Section 2.2). As a result, smaller grains have a lower thermal contrast, which decreases the polarization. Larger grained soils are characteristic of undisturbed soil, so this contrast is useful in detecting soil that has recently been disturbed.

El-Saba and Bezuayehu demonstrated that fusing radiance images with angle of polarization images significantly improved the probability of detecting landmines. For a 10% probability of false alarm, the S_0 image yielded a probability of detection of 30%, examining angle of polarization increased this to 60% and looking at the fused image gave a probability of detection of 70%. Finally, they looked at using different proportions of S_0 and angle of polarization in the fused image and found that probability of detection could be increased to 80% by optimizing the relative amounts of the two factors [37].

Another effort used hyperspectral and polarimetric information to improve contrast between partially or fully exposed mines and the background. Overall, the soils they examined had a very low polarization, so they used polarization to detect the mines themselves. They also used a few decoy targets such as a frisbee. Their results showed that the combination of polarimetric and hyperspectral information significantly improves the effectiveness of their technique [38].

3.2   Surface Normal Estimation

Another area of recent interest has been using polarization for 3D scene reconstruction. The basic postulate is, if the index of refraction is known, the elevation angle of the sensor, with respect to the surface normal, can be determined using the Fresnel equations. The vast majority of work available in the literature has been done in the visible, and at one wavelength. An issue with using only a single wavelength is there can potentially be two different surface normal angles with the same polarization signature. Figure 8 shows an example of how DoLP can vary with angle. Virtually all scenarios exhibit this shape which clearly demonstrates that two angles can produce identical DoLP. Including multiples spectral points with different n and κ will constrain this problem providing a unique solution. Additionally, incorporating additional spectral points may help to mitigate error due to noise in the DoLP measurement.
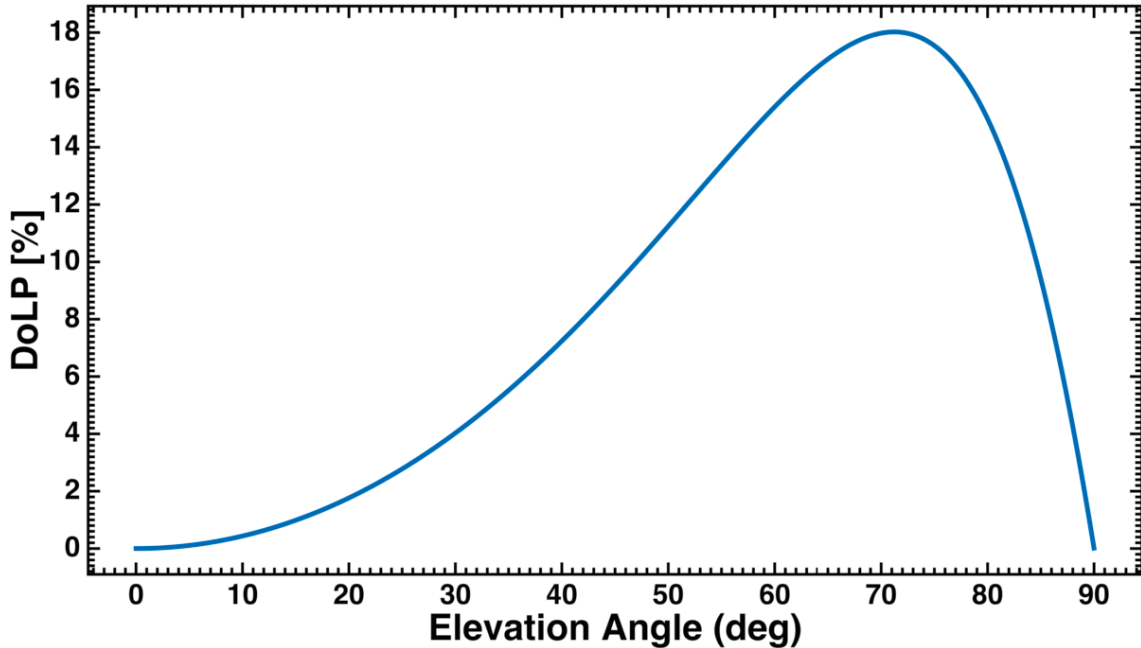
Figure 8. DoLP as function of surface normal angle for $n = 1.5$ **and** $\kappa = 1.$

Atkinson and Hancock developed a method that combined shape-from-shading and polarimetry to estimate shape [39], [40]. Their method images a smooth dielectric surface at two different angles, with a known illumination source position. The reflectance function, essentially a simplified version of a BRDF, is estimated from image statistics. With the reflectance function estimated, and with a known index of refraction, the polarimetric signature can be predicted as a function of angle. Any light that penetrates the surface before being reflected back out is assumed to be completely depolarized. An algorithm is then employed to find the angle that best matches the measured signature from the two views. Because of the constraints needed, this method would be difficult to implement on a remote sensing platform.

Miyazaki and Saito, et. al. proposed a way to deal with internal reflections when observing a partially transparent material using inverse raytracing [41], [42], [43], [44]. Raytracing uses the surface normal and index of refraction to determine how a ray of light would pass through a material. There is no closed-form solution to the inverse problem, but an iterative technique was proposed. As with the previously mentioned method, the surfaces are assumed to be optically smooth. Another assumption is that the back surface of the material is flat. To start, an initial shape is assumed and the gradient of the surface at each point is calculated. An error function is measured based on two-norm of the difference between the predicted and measured polarization across the surface. New gradients are calculated by subtracting, from the previous iterations calculated gradients, a factor proportional to the partial derivative of the error function with respect to the original gradients. These new gradients are used to calculate a new object shape. The iteration stops when the error function integrated over the entire surface is minimized.

Gartley et. al. attempted to use polarimetry to determine pose information of unresolved (sub-pixel) targets, using a broadband sensor in the LWIR [45]. In this

work, a car was modeled using previously measured polarimetric reflectance functions for paint, metal, rubber and glass. The car was modeled in DIRSIG to determine the predicted polarimetric signature. The vehicle was modeled at a number of different zenith and azimuth angles. This was linearly interpolated to generate a target space as a function of these viewing angles. Their results, however, were disappointing, which they attributed to not properly accounting for adjacency effects of other objects in the scene.

A LWIR model was developed by Reid et. al. to determine how errors in the assumed values for surface roughness and index of refraction affected the surface normal estimation [46]. Their model used the Torrance and Sparrow BRDF model, adapted to include polarization [47]. They found that in order to estimate angles to within a couple degrees, surface roughness and index of refraction had to be known to within 5% of their true value.

Other uses of shape estimation using polarimetry found in the literature include: quality assurance of optical elements [48], active illumination techniques [49], extending this concept to out-of-plane scattering for rough surfaces [50], and using two camera stereo imaging [51], [52]. All of these works, however, only deal with broadband polarimetry. By including hyperspectral information, additional constraints can be placed on the estimations of surface normal.

3.3 Hyperspectral Target Detection

While the primary focus of this research will be classifying and identifying materials, rather than detecting them, the principles used in characterization can also be useful in detection, and vice versa. Detecting an object can be thought of as the first step in characterizing it, so detection techniques are of interest to this research. Both

polarimetry and spectroscopic techniques can be of use in detection; to start, some hyperspectral methods are discussed.

One of the most widely used hyperspectral target detection techiniques is the RX algorithm proposed by Reed and Xiaoli as a way to detect anomalies in a scene. [53] The algorithm works by examining two groups of pixels, called windows, and computing the mean spectra of pixels within each window. One window is chosen to be the expected size of the target in the image, while the second larger window surrounds the first and is used to estimate the local background. The background covariance matrix is calculated from the statistics of the local background pixels. This is assumed to be the same as the target covariance matrix. The result of the RX-algorithm is

$$RX(\mathbf{r}) = (\mathbf{r} - \mu_b)^T \mathbf{C}_b^{-1} (\mathbf{r} - \mu_b), \tag{32}$$

where $\mathbf{r}$ is the pixel spectra, μ_b is the mean spectra of the background, and $\mathbf{C}_b$ is the covariance matrix. If this gives a result greater than some pre-defined threshold, the pixel is flagged as a target. [54]

Subspace matched detectors represent a step up in complexity from the RX algorithm. The central concept underlying subspace matched detectors is that there may be some variability in the signature of a target based on scene geometry, illumination conditions, weathering, etc. To account for this, a target subspace is developed where the basis vectors represent different types of variance. The key is to have some understanding of the potential variations in the target signature and model them well enough so the subspace is small enough to limit false alarms, but large enough to detect the target under all conditions. Note that one potential variation in the signature could be changes in reflectivity or emissivity with viewing angle as discussed in the previous section. This variablity will increase the size of the subspace needed

32

to describe a material making it more difficult to detect without increasing the false alarm rate. [55]

One example of a subspace matched detector was developed by Healey and Slater, using a physical model to attempt to extract material reflectance from radiance data, which is then compared to some exemplar of a material. The atmosphere was modeled with four separate standard atmosphere profiles, four different water vapor profiles, four different profiles for other gases, and four aerosol profiles, for a total of 256 different atmospheric models. There were also eight different solar zenith angles, seven sensor altitudes considered, and a binary parameter for whether the object was in shade or not. This gave 28762 different conditions, but only 17920 were physical feasible. For each of the 17920 conditions, an expected radiance was calculated based on the reflectance exemplar. For each pixel in the scene the maximum likelihood it belongs to a class is calculated and if it exceeds some threshold, the pixel is identified as the material from which the reflectance exemplar was taken. [56]

Another class of popular techniques are spectral change detectors, which seek to find differences in a scene based on two or more observations. This seems fairly simple, but it is important to discriminate changes that are actually of note from changes that are due to natural variation in the scene from one time to the next. Additionally, changes in atmospheric parameters can make it appear that there are changes in a scene when there really are not. Finally, it can be very difficult to take two consecutive images of the same scene from the same position, so image registration is necessary. Any misregistration will be observed as a difference in the two scenes [57].

One way to account for some of these effects is to incorporate a model to detect changes in reflectance or emissivity at a pixel, rather than simply radiance. Meola *et al* proposed a model based approach for visible and NIR imagery [58]. They modeled

33

the sensor radiance at a pixel as

$$L(\lambda) = \rho(\lambda) \left[\alpha \tau(\lambda) L_s(\lambda) \cos \theta + \beta \tau(\lambda) L_d(\lambda) \right] + L_p(\lambda) + n(\lambda), \tag{33}$$

where ρ is the material reflectance, τ is the transmission of the atmophere, L_s and L_d are the direct and indirect solar illumination on the target respectively, L_p is the path radiance, and n is the sensor noise. α and β are shadowing terms meant to account for variations in illumination from image to image. Objects in the scene are assumed to be Lambertian, so there is no angular dependence of reflectance.

This problem has more unknown parameters than available measurements, however, so MODTRAN is used to model the spectral behavior of atmospheric transmission, path radiance, as well as direct and indirect solar illumination. Modeling the atmosphere allows these quantities to be calculated spectrally based on a handful of quantities related to weather conditions, solar and sensor positions. With this and a model of sensor noise, all the parameters can be solved for using two images of a scene.

The two hypotheses to test at each pixel, m, are:

$$\begin{aligned} H_0 &: \quad \rho^{(1)}[m] = \rho^{(2)}[m] \\ H_1 &: \quad \rho^{(1)}[m] \neq \rho^{(2)}[m]. \end{aligned} \tag{34}$$

The likelihood a pixel is a target is expressed

$$D^{(t)}[m|\mathbf{x}] = \left(L^{(t)}[m] - \mu_0^{(t)}[m|\mathbf{x}] \right)^T \left(\Gamma_0^{(t)}[m] \right)^{-1} \left(L^{(t)}[m] - \mu_0^{(t)}[m|\mathbf{x}] \right). \tag{35}$$

$L^{(t)}[m]$ is the measured radiance at time t for a pixel, $\mu_0^{(t)}[m|\mathbf{x}]$ is the expected mean radiance based on the model parameters, $\mathbf{x}$, and $\Gamma_0^{(t)}[m]$ is the noise covariance matrix which is assume to be known. The system is then optimized to minimize the sum

34

of the likelihood function across all pixels and times. Note that in order for the optimization to work, even with only one atmopheric parameter, at least five spectral bands are needed. In practice, more are required to accurate model the atmospheric effects. Once the optimization is performed, the likelihood is calculated for each pixel and if it results in a value above some threshold, the pixel is flagged as a target.

The class of techniques which are most related to this research are signature matched detectors. As the name suggests, signature matched detectors attempt to find spectra in a scene that resemble a reference signature for some target. The basic principle is to create two classes which obey gaussian statistics; one for the null hypothesis, i.e. no target present, and another for the alternative, target present, hypothesis. The probability that a given spectra belongs to either class can be calculated and if it is above a certain threshold, the corresponding pixel is flagged as a target.

One of the earliest of these methods was the spectral angle mapper (SAM), which treats the target and measured spectra as vectors in a space with dimensionality equal to the number of spectral points. The angle between these two vectors is then calculated

$$\cos(\alpha) = \left(\frac{\mathbf{t} \cdot \mathbf{r}}{\|\mathbf{t}\| \cdot \|\mathbf{r}\|} \right). \tag{36}$$

$\mathbf{t}$ and $\mathbf{r}$ represent the assumed target and measured spectra. If this value is sufficiently close to unity, the two spectra are similar enough and the pixel is flagged as a target. [59]

There are problems with the spectral angle mapper, however. First, SAM cannot distinguish between negative and positive correlation. For example, if the expected target spectra is [7 , 6 , 5 , 6 , 7] and the measured spectra is [5 , 6 , 7 , 6 , 5], the SAM value would be 0.97. These spectra clearly are not close to the same, however, because they are inversely correlated. Additionally, the SAM cannot distinguish

intensity differences between spectra. Sometimes this is an advantage as the same target under varying illumination conditions will always be detected. At other times, however, different intensity levels can be an indication of two different materials.

One proposed improvement was the spectral correlation mapper. This relied on the a varient of the Pearsonian correlation coefficient, expressed

$$R = \frac{\sum_{i=1}^{N}(t_i - \bar{t})(r_i - \bar{r})}{\sqrt{\sum_{i=1}^{N}(t_i - \bar{t})^2 \sum_{i=1}^{N}(r_i - \bar{r})^2}}. \tag{37}$$

This does not change the ability to distinguish intensity differences, but it does allow the correlation value to go negative indicating an inverse correlation. For the case presented in the previous paragraph, the correlation coefficient would be negative one, so the spectra in question would not be incorrectly identified as a target. [60]

The spectral match filter (SMF) accounts for both spectral and overall intensity differences. In this case, the detection metric is

$$d_{SMF}(\mathbf{r}) = \frac{(\mathbf{t} - \mu)^T \Sigma^{-1}((\mathbf{r} - \mu)}{(\mathbf{t} - \mu)^T \Sigma^{-1}((\mathbf{t} - \mu)}. \tag{38}$$

$\mathbf{t}$ and $\mathbf{r}$ again represent the expected target and measured spectra respectively. $\mathbf{r}$ is equal to the background, $\mathbf{b}$, for the null hypothesis, and $\mathbf{r} = \alpha\mathbf{t} + \mathbf{b}$ when a target is presents. α denotes the abundance of the target in the pixel. μ and Σ represent the mean vector and covariance matrix of the background. The background can be calculated using either the entire image or pixels in a smaller window centered around the pixel being interrogated [23].

Possibly the most commonly used signature matched detector is the adaptive cosine/coherence estimator (ACE) [61]. This is very similar to the SMF, but is adapted so target pixels are modeled to have some abundance of background as well

as target signatures. The detection metric is

$$d_{ACE}(\mathbf{r}) = \frac{\left[(\mathbf{t} - \mu)^T \Sigma^{-1}((\mathbf{r} - \mu)\right]^2}{\left[(\mathbf{t} - \mu)^T \Sigma^{-1}((\mathbf{t} - \mu)\right]\left[(\mathbf{r} - \mu)^T \Sigma^{-1}((\mathbf{r} - \mu)\right]}. \tag{39}$$

Again, $\mathbf{t}$ and $\mathbf{r}$ represent the expected target and measured spectra respectively. Now, however, $\mathbf{r} = \alpha\mathbf{t} + \beta\mathbf{b}$, where β is the background abundance, when a target is present.

3.4 Polarimetric Target Detection

Because most natural materials display relatively little polarization, polarimetry can be particularly useful in detecting man-made targets. There are numerous examples in the literature, [28, 62, 63, 64, 65, 66, 67, 68, 69] to name a few, demonstrating how polarimetry can aid in target detection. In the interest of time, these will not be discussed in detail, but a few others will be focused on here to give a general idea of what these techniques entail.

The fringe-adjusted joint-transform correlation algorithm attempts to detect targets by comparing an image of the scene to a reference image. To start, the scene image is resized to match the scale of the reference image, then the two images are registered together. $r(x, y + y')$ is used to denote the reference, while $t(x, y - y')$ represents the input image. The input joint image is expressed

$$f(x, y) = r(x, y + y') + t(x, y - y'). \tag{40}$$

The 2-D Fourier transform of this joint image is taken yielding

$$F(u, v) = |R(u, v)|e^{\phi_r(u,v)}e^{-iuy'} + |T(u, v)|e^{\phi_t(u,v)}e^{-juy'}, \tag{41}$$

where $|R(u, v)|$ and $|T(u, v)|$ are the amplitudes of the Fourier transform of r and t,

while ϕ_r and ϕ_t represent the phases. The joint power spectrum is the magnitude squared of $F(u,v)$. A fringe-adjusted factor is defined

$$H_{faf}(u,v) = \frac{B}{A + |R(u,v)|^2},$$

(42)

where A and B are constants adjusted to improve the correlation. $H_{faf}(u,v)$ is multiplied by $|F(u,v)|^2$ to give the fringe-adjusted joint power spectrum. The inverse 2-D Fourier transform is then taken. If the scene and reference image are identical, there will be peaks at $\pm 2y'$, any other peak in the image represent potential targets. Results have shown that performance metrics are significantly improved by incorporating polarization images into the algorithm. [70]

Another category of polarimetric target detection in the literature uses fusion images. The high-boost fusion method assigns varying weights to different information about an image before fusing the images together and running a detection algorithm on the fused image. One example was proposed by El-Saba and Sakla [71] which weighted polarization-based images of the scene more heavily than the total radiance. Two different boosted images were used: one which added two times the S_1 image to the S_0 image, and another was composed of five times the angle of polarization image added to two times the S_0 image. The factors for each bit of information which yielded the best performance metrics were used. The FJTC algorithm was then applied as above, however the fringe-adjusted factor was changed to a "Mexican-hat wavelet" which is the second derivative of the Gaussian function. It was found that the angle of polarization and S_0 fused image performed the best, significantly improving the detection metrics over the S_0 image alone. [71]

Another fusion detection algorithm is the spectral/polarimetric integration (SPI) decision fusion algorithm, which combines two previously developed algorithms. [72] The first is the constrained energy minimization (CEM) algorithm, which is a modified

version of the SMF algorithm discussed in the previous section. For a measured spectra $\mathbf{x}$, the CEM score is given

$$CEM(\mathbf{x}) = \frac{(\mathbf{t} - \mathbf{m})^T \mathbf{S}^{-1} (\mathbf{x} - \mathbf{m})}{(\mathbf{t} - \mathbf{m})^T \mathbf{S}^{-1} (\mathbf{t} - \mathbf{m})}. \tag{43}$$

$\mathbf{t}$ is the spectra of the target; $\mathbf{m}$ and $\mathbf{S}$ represent the mean spectra and covariance matrix of the background [73].

The second algorithm used is the topological anomaly detection (TAD) algorithm, which first normalizes the image so the brightest 10% of pixels have a Euclidean two-norm equal to two, while the darkest 1% of pixels have a norm equal to one. Then, a random sample of pixels is taken and the distance between every pair of chosen pixels is computed. Large groups of points are designated as background, while small groups or isolated pixels are identified as potential targets. The TAD score for each pixel is the sum of the distances to its third, fourth, and fifth nearest neighbors [74].

The SPI algorithm uses the CEM score of the spectral information and the TAD score of the polarimetric information. The total SPI score for a pixel x is given

$$SPI(x) = CEM(\mathbf{x}) \left[CEM(\mathbf{x}) + TAD(\mathbf{x}_s) \right], \tag{44}$$

where $\mathbf{x}$ is the measured spectra and $\mathbf{x}_s$ is the measured Stokes vector. It has been shown that incorporating the polarization dramatically improves detection performance in visible imagery when the sensor is near the specular lobe for solar reflection. Performance degraded as the sensor moved away from the specular lobe, however. [72]

The adaptive polarimetric target detector seeks to improve existing target detection algorithms by determining the optimal set of polarizer angles for target detection in a given scene. First, a Stokes vector image of the scene is measured using some standard method, such as the modified Pickering method. The mean Stokes vector

39

and covariance matrix can then be calculated from the data. The measured scene intensity covariance matrix, Σ_I, can then be estimated

$$\Sigma_I = M^T \Sigma_S M + \Sigma_I^n, \tag{45}$$

where M is a matrix whose rows are $m_i = 0.5[1 , \cos 2\theta_i , \sin 2\theta_i]$ and Σ_I^n is the covariance matrix for the noise in the instrument. θ_i is the polarizer angle. A target mean Stokes vector is assumed to be known, and the Stokes covariance matrix, Σ_S, can be calculated based on an assumed knowledge of the scene intensity covariance matrix, Σ_I. The detectability of the target is estimated

$$SCR_V^2 = (\mu_t - \mu_b)^T \Sigma_V^{-1} (\mu_t - \mu_b). \tag{46}$$

Subscript v represents the vector space in which the detection is performed. μ_t and μ_b represent the mean vector of the target and background respectively. The combination of polarizer angles that maximizes SCR_V is then found and another set of images of the scene is taken at those polarizer angles. From here, some target detection algorithm can be used to find targets in the scene. [75]

The final polarimetric target detection technique discussed here is the M-Box covariance equality test which attempts to find targets by comparing the covariance matrix for some part of the image to a reference covariance matrix. Romano and Rosario applied this method to a scene with three tanks at different orientations. [76] They chose a seven pixel square window to use. They found that natural clutter tended to have the smallest variance, so they chose the reference window to be the 7x7 window across the entire image with the smallest covariance. The discriminate function is

$$-2 \log M = v \log |\Sigma_1| + v \log |\Sigma_2| - 2v \log \left| \frac{\Sigma_1 + \Sigma_2}{2} \right|, \tag{47}$$

where Σ_1 is the covariance across the test window and Σ_2 is the covariance across the reference window. A window with an identical covariance to the reference will give a value of zero. Some threshold is defined and if the M-value for a given window exceeds this, the pixel at the center of the window is idenified as a target. This algorithm was shown to out-perform a version of the RX algorithm adapted to polarimetry. [76]

3.5   Temperature-Emissivity Separation Algorithms

While detecting a target based on differences from its surroundings is useful, identifying something often requires information more fundamental to the material, such as its reflectivity or emissivity. Two primary factors describe the emitted radiance from a material: the temperature of the material surface and the emissivity. For a hyperspectral sensor with N spectral channels, this means there are $N+1$ unknowns, assuming all other variables in the scene are known. Consequently, determining the temperature and emissivity of a target is a fundamentally underdetermined problem. The purpose of temperature-emissivity separation (TES) algorithms is to estimate one or both of these parameters by imposing some constraint on the data. Several of these approaches will be discussed, but note that there are numerous others available in the literature: [77, 78, 79, 80, 81] to name a few.

The earliest approach, found by this author, to solving the TES problem was the reference channel method [82]. It is assumed that the emissivity value in one spectral band is known, and from this a temperature is calculated. The temperature value is then used in conjunction with measured radiance values to calculate the emissivity in the rest of the bands. The obvious issue with this routine is if emissivity in one band is already known, there often isn't a lot of utility in determining emissivity in the rest of the bands. This method is only useful for distinguishing groups of materials that have known, and similar, emissivity values in a given spectral band.

Another early technique was the normalized emissivity method (NEM) [83], which also assumes one spectral emissivity value is known. Unlike the reference channel method, it is not assumed which spectral band this known emissivity value represents. First, an emissivity value is chosen and temperatures are calculated using the radiance data in each band and assuming this emissivity. The largest calculated temperature is taken to be the temperature of the scene. Finally, emissivity values in all bands are calculated using this temperature and the measured spectral radiance values. Clearly the band which calculated the highest temperature will then have the same emissivity value as the input guess, which effectively reduces the dimensionally of the problem by one. This works in regions where *a priori* knowledge of the scene is available, for example, the class of minerals likely to be observed. It is of limited use, however, in applications where spectrally diverse targets need to be identified.

The alpha residual method [84] uses Wien's approximation, which neglects the -1 in the denominator of the planckian radiance equation, in order to derive a linear set of equations to solve for emissivity. The radiance equation, after compensating for atmospheric effects and downwelling radiance, becomes

$$L_j = \epsilon_j \frac{C_1}{\lambda_j^5 \pi e^{\frac{C_2}{\lambda_j T}}}; \tag{48}$$

where C_1 and C_2 are constants which depend on the speed of light, Boltzmann's constant, and Planck's constant. j indexes the specific waveband being measured. Taking the natural log of both sides and multiplying by λ_j gives

$$\lambda_j \ln L_j = \lambda_j \ln \epsilon_j + \lambda_j \ln C_1 - \lambda_j 5 \ln \lambda_j - \lambda_j \ln \pi - \frac{C_2}{T}. \tag{49}$$

Then, the average of over all spectral points is taken and subtracted from Equation 49. It's clear to see that since the temperature dependent term is not wavelength

dependent, it will drop out. The equations are rearranged so the emissivity dependent terms are on one side of the equation and a new parameter, α_j, is introduced:

$$\lambda_j \epsilon_j - \frac{1}{N} \sum_{j=1}^{N} \lambda_j \ln \epsilon_j = \alpha_j = \lambda_j \ln L_j - \frac{1}{N} \sum_{j=1}^{N} \lambda_j \ln L_j + K_j. \tag{50}$$

K_j has no dependence on measured radiance values, and is defined as

$$K_j = -\lambda_j \ln C_1 + \frac{\ln C_1}{N} \sum_{j=1}^{N} \lambda_j + \lambda_j 5 \ln \lambda_j - \frac{5}{N} \sum_{j=1}^{N} \lambda_j \ln \lambda_j + \lambda_j \ln \pi - \frac{\ln \pi}{N} \sum_{j=1}^{N} \lambda_j. \tag{51}$$

α_j can be calculated using the right-hand side of Equation 50 and measured values of L_j. This can either be compared to lab calculated α values or used to solve for the emissivity. Using this method, the spectral shape of the material emissivity can generally be recreated quite accurately. The complication with this routine is, because the mean is subtracted from Equation 49, the absolute values of emissivity are lost. In applications where accurate emissivity values and temperatures are necessary, this method is far less useful. Additionally, using Wein's approximation will lead to small, but potentially significant, errors in calculated emissivity values.

The temperature emissivity separation algorithm described in [85] uses a hybridization of a few of the methods discussed above. First, the surface temperature is estimated using the NEM. The ground emitted radiance is calculated

$$R = L' - (1 - \epsilon_{max})L_d, \tag{52}$$

where L' is the measured radiance compensated for atmospheric transmission and path radiance effects and L_d is the downwelling radiance. A temperature is calculated using the initial guess, ϵ_{max}, as the emissivity. Again, the maximum temperature calculated is taken to be the temperature of the scene. With this temperature, a new

emissivity is calculated

$$\epsilon_b = \frac{R_b}{B_b(T_{NEM})}.$$

(53)

The calculated emissivity values are then used to re-calculate the temperature and the process is repeated until R converges, or the maximum number of iterations is reached. The second module utilizes the spectral ratio method, which gives relative emissivities defined

$$\beta_b = \frac{N\epsilon_b}{\sum_{b=1}^{N} \epsilon_b}.$$

(54)

The third step uses the Min-Max Difference (MMD) method described in [86]. This uses the relative emissivities to solve for the minimum emissivity, which is then used to solve for emissivity in each band:

$$\begin{aligned}
MMD &= \max(\beta_b) - \min(\beta_b) \\
\epsilon_{min} &= 0.994 - 0.687 * MMD^{0.737} \\
\epsilon_b &= \beta_b \left(\frac{\epsilon_{min}}{\min(\beta_b)} \right)
\end{aligned}$$

(55)

The MMD is modified, however, to account for noise

$$MMD' = \left[MMD^2 - 1.52NE\Delta\epsilon^2 \right]^{-1},$$

(56)

where $NE\Delta\epsilon$ is determined from the Noise-Equivalent Temperature Difference (NEΔT) of the sensor. The final step is to repeat the above steps once using the improved ϵ estimates to recalculate the downwelling radiance used to solve for L'.

With error-free inputs, this algorithm was capable of measuring emissivity to within 0.015, and temperature to within 1.5 K when five spectral bands were used. The accuracy of the atmospheric inputs, however, is the limiting factor on the accuracy of the algorithm. [87]

To this point, the TES algorithms discussed have been designed for multi-spectral

data, hyperspectral data introduces more information that can potentially be used to constrain this problem. One of the most common modern TES techniques is the maximum smoothness method developed by Borel [88, 89]. The premise of this technique is that the emissivity spectra of solid targets tend to be smoothly varying, specifically when compared with atmospheric spectral features. An initial temperature estimate is either provided or calculated based on the state of the atmosphere as solved for by the atmospheric correction. From this, an effective emissivity can be calculated for a number of temperatures around this temperature. The smoothest emissivity is selected to be the correct answer. The smoothness metric is

$$\sigma(\epsilon) = STDEV\left(\epsilon_m - \frac{\epsilon_{m-1} + \epsilon_m + \epsilon_{m+1}}{3}\right) \qquad m = 2, ..., M-1 \qquad (57)$$

where M is the number of spectral channels, indexed by m. A TES method based on this algorithm will be used as a basis for comparison later in this document.

3.6   Hyperspectral Material Classification

Material classification and identification are two of the primary uses for hyperspectral information. Classification involves grouping pixels in a scene into categories, while identification goes a step further and seeks to identify the material each of these categories represent. In this section, some of the basic classification techniques will be covered first, then some papers with applications to material identification will be discussed.

Principle component analysis (PCA) is a way to reduce the dimensionality of a hyperspectral data set. Hyperspectral measurements tend to have many data points which are highly correlated. PCA works by taking the correlated original basis set of spectral points and expressing in terms of a new set of orthogonal "principle compo-

nents," which are linear combinations of the original set. I It is useful when performing this analysis to think of the hyperspectral data as a matrix with each pixel forming one dimension of the matrix and the spectral points forming the other dimension.

Performing the singular value decomposition on this matrix, X, gives $X = U\Sigma W^T$. If X is an n-by-p matrix, then U is an n-by-n matrix of orthonormal column vectors and W is a p-by-p matrix of orthonormal column vectors. These column vectors are called the left and right singular vectors of X, respectively. Σ is an n-by-p rectangular diagonal matrix of positive numbers, where the singular values of X form the diagonal. The product $U\Sigma$ represents the hyperspectral data in terms of the principle components. This means W is a projection matrix that projects X onto the principle components [90]. PCA can also be thought of as diagonalizing the covariance matrix, where Σ has the eigenvalues along the diagonal and the columns of U are the eigenvectors [23].

Σ is customarily rearranged into descending order, and the corresponding vectors in U and W are rearranged accordingly. The singular values are a representation of how important each principle component is to reconstructing the true data set. Often, the first few principle components contain the majority of the information about a scene. If this is the case, the dimensionality of the data set can be greatly reduced by truncating the matrices, keeping only the first few singular values and their corresponding vectors. [91]

K-means is one of the oldest and simplest classification algorithms. First, a number of classes is assumed and an initial class mean vector is defined; either based on *a priori* knowledge, or chosen at random. Each spectrum, in our case the measured spectra at each pixel is assigned to the class with the smallest Euclidean distance between itself and the class mean vector. Other distance metrics are also available such as the spectral angle, which normalizes all the spectra to look at only relative spectral

differences instead of absolute intensity differences. Once all of the spectra have been designated, new class mean vectors are defined based on the average spectrum of all the pixels assigned to that class. This process is applied iteratively until either the number of spectra switching classes or the change in the class mean vectors between iterations is below some threshold. [92]

One issue with this algorithm is that it requires the number of classes to be defined beforehand. In many applications, the number of different materials is something the user is seeking to learn from the data, not something available in advance. Additionally, this algorithm only solves the classification problem, as it does not assign identities to the classes. With some calibration, spectral signatures can be matched to a database of materials, but this requires some knowledge of atmopheric conditions and/or object temperatures.

The Stocastic Expectation Maximization (SEM) algorithm starts by either randoming, or based on some initial classification, assigning the spectra to one of a pre-defined number of classes. The initial number is considered an upper bound on the number Benefits of P-HSI over HSI More accurate reflectivity at off-nadir viewing likely to be in the scene. For each of the classes, a mean vector and covariance matrix is calculated. The "prior" for each set is defined as the percentage of the total number of spectra contained within a given set. If this is less than some threshold, the class is eliminated. Based on the class priors, covariance matrices, and mean vectors, a probability that each spectra belongs to a class is calculated. The spectra are then randomly assigned to classes again, but this time with weighted probabilities based on the calculated probability of belonging to a certain class. New priors, covariance matrices, and mean vectors are then calculated and the process is repeated until changes in the probability values are sufficiently small. One drawback of this

technique is that the solution has been found to be highly dependent on the initial conditions. [93]

The Improved Split and Merge Clustering (ISMC) algorithm seeks to segment an image into the number of pattern classes that best represents the data. At first, the algorithm assumes that every spectra belongs to the same class. The class is searched through to find the two spectra with the greatest Euclidean distance between them, which are dubbed $\mathbf{y}_{min}$ and $\mathbf{y}_{max}$. If this distance is greater than some user-defined threshold, the class is split and the remaining spectra are divided into classes based on their Euclidean distance to the reference spectra. This step is applied to each subsequent class until no class is split. Once this is completed, the mean vector for all the classes is computed. Classes are merged together if the distance between their mean vectors is less than some defined threshold. All of the spectra are then assigned to classes based on their distance to the class mean vectors. The class mean vector is then updated based on the average of all the spectra assigned to that class. A "scatter" matrix is defined

$$S_b = \sum_{k=1}^{K} n_k(\mathbf{m}_k - \mathbf{m})(\mathbf{m}_k - \mathbf{m})^T, \tag{58}$$

where $\mathbf{m}$ is the mean vector of all the spectra, $\mathbf{m}_k$ is the mean vector of the kth cluster, and n_k is the number of spectra in the kth cluster. The trace of this scatter matrix is taken and then the entire process is repeated until the percent change in the trace of the scatter matrix is below some tolerance. [94]

Support vector machines (SVM) are a binary classification which seeks the maximum separation between two classes. The binary classifier is defined $y_i \in [-1, 1]$ which assigns each spectra a -1 or 1 value depending on the class it belongs to. For a linear classifier of spectra with N measurements, this can be thought of as maximizing the distance between two N-dimensional hyperplanes, such that no spectra lie in

between the planes. These hyperplanes are defined

$$\mathbf{w} \cdot \mathbf{x} - b = \pm 1. \tag{59}$$

The distance between the planes is $\frac{2}{\|\mathbf{w}\|}$, so the goal is to minimize $\|\mathbf{w}\|$. This is subject to the constraint that $y_i [\mathbf{w} \cdot \mathbf{x}_i - b] \geq 1$ for all spectra. [95]

Non-linear classifiers can also be used by incorporating a kernel, K. The optimization problem then become maximizing

$$\sum_{i=1}^{N} \alpha_i - \frac{1}{2} \sum_{i=1}^{N} \sum_{j=1}^{N} \alpha_i \alpha_j y_i y_j K(\mathbf{x}_i, \mathbf{x}_j), \tag{60}$$

such that $\sum_{i=1}^{N} \alpha_i y_i = 0$ and $0 \leq \alpha_i \leq C$, where C is a regularization parameter. There are many different kernels available, but one common one is the Gaussian radial basis function

$$K(\mathbf{x}_i, \mathbf{x}_j) = e^{-\gamma \|\mathbf{x}_i - \mathbf{x}_j\|^2}, \tag{61}$$

where γ is inversely proportional to the width of the gaussian. [95]

There are also a variety of different methods for applying this to more than just a binary classification. The one-against-all strategy attempts to create maximum separation between one class and all the others. The one-against-one strategy considers every combination of class pairs and uses an SVM for each. There are also hierarchical based approachs that split the original set into classes, then split those subclasses, etc. [95]

The algorithms discussed above assume that each pixel contains only one material. In reality, one spectra may have a mixture of different contributions, especially if the ground sampling distance of a single pixel is large. To account for this, mixing models attempt to decompose the mixed spectra into pure spectral "endmembers." This way

the dataset can be reduced to a few spectra with relative abundances defined at each pixel. The simplest of these methods is the linear mixing model.

The fundamental problem can be expressed

$$\mathbf{x} = \sum_{i=1}^{M} a_i \mathbf{s}_i + \mathbf{w} = \mathbf{Sa} + \mathbf{w}, \tag{62}$$

where $\mathbf{S}$ is a matrix whose columns represent the endmembers spectra, $\mathbf{a}$ is the fractional abundance vector, $\mathbf{w}$ represents noise, and $\mathbf{x}$ designates a measured spectra. Note that the summation over $\mathbf{a}$ cannot be greater than 1. Before endmembers are determined, the dimensionality of the data is usually reduced using PCA, or something similar, to make the subsequent computations less time consuming. One way to determine endmembers is to assign them based on previously measured spectra representative of different types of materials expected to be found in the scene. For example, if observing a forest, there may be endmembers associated with different varieties of tree leaves, bark, soil, etc. [96]

There are also automated methods for determining endmembers. Endmembers can be determined using some of the previously mentioned clustering algorithms like K-means, SEM, ISMC, or SVM. They can also be determined geometrically using a process known as "shrinkwrapping". This can be thought of by considering a number of pixels with only two spectral components, though the idea can be extended to many dimensions. Each measured spectra would be plotted with one component on the x-axis and the other on the y-axis. Then, the area of a triangle is minimized, such that the triangle still contains all measured spectra. The vertices of this triangle represent the endmember spectra. Often in visible images where different illumination conditions are present, one of the endmembers will be set as a "dark" point at 0,0. Note that these vertices may not correspond to an actual measured spectra, indicating that no single pixel is purely that one material. For this process to work in higher

dimensions, however, there has to be more endmembers then spectral points, which is why dimensionality reduction is often useful. The final step is known as inversion, where the relative abundances are calculated from the endmembers. This is usually done by constrained least squares fitting, ensuring **a** cannot sum to greater than 1, and cannot have any members less than 0. [96]

Heiden *et al* applied a linear unmixing technique to characterize urban surface materials [97]. Measured endmembers were compared to a spectral library of materials based on more than 21000 spectra of common construction materials. Material classification and identification is complicated in urban settings by the wide variety of potential illumination conditions, as well as weathering of materials. They examined a number of different features, such as the position and height of reflectance peaks, the ratio of specific spectral points, and the mean and standard deviation of the data. They found materials could be accurately characterized, so long as they contained two or more spectral features. They also found that classification with hyperspectral imagery performs significantly better than simply gray-scale imagery, as expected.

The technique for target detection developed by Healey and Slater (see Section 3.3) can also be used for material identification. They demonstrated this technique on a hyperspectral image of Fort Hood measured by the HYDICE sensor. 11 different material classes were selected: nine different roofing materials, asphalt, and vegetation. From this, different atmospheric permutations were used to calculate a maximum possible radiance for a given material class. Any spectra above this intensity was automatically ruled out from that class. Then, the likelihood each pixel belonged to a certain class was determined and the pixel was assigned to the class with the maximum likelihood. They compared their algorithm to a spectral matching algorithm based on the Euclidean distance and found theirs to be far more accurate, specifically at correctly classifying the dark sides of roofs. [98]

51

Vaughan *et al* used LWIR multi- and hyper-spectal imagery to identify mineral distributions. Many common mineral types have spectral features in the LWIR, so it is an ideal spectral band for identifying minerals. First, an atmospheric correction, based on models, was applied to the measured radiance to calculate the radiance at the surface. The TES algorithm described above was used to solve for the emissivity. Endmembers were determined using either spectral libraries, manually choosing pixels in the scene that represented pure spectra, or unsupervised techniques such as those discussed earlier in this section. The classification was done using both the SAM and spectral matched filtering. They found that multi-spectral data could determine whether an area was silica- or clay-rich, but to accurately identify specific minerals, hyperspectral data was needed. [99]

3.7 Polarimetric Material Classification

While hyperspectral techniques are used far more extensively, there have been some attempts at using polarimetry for material classification and identification.

Polarization of Water.

Shaw examined the polarimetric properties of water in the LWIR, finding that the degree of polarization is between 6 and 12% when viewed under a dry, clear atmosphere [100]. He found several things of interest to this research. First, radiance from water in the LWIR appear vertically polarized; as opposed to radiance in the visible and NIR, which appears horizontally polarized. This is because the dominant radiance source is the self-emission of the water, as opposed to solar reflection. The idea that the direction of polarization can be used to determine whether a signature is reflection- or emission-dominated is something that will be exploited later in this document. The second conclusion of interest is that the degree of polarization depends

on the radiometric contrast between emission and reflection. Water viewed under a clear sky was more polarized than water viewed under a cloudy sky. As shown in Section II, this is a result that is expected based on the theory. Finally, when solar glint is in the image, the polarization becomes horizontally polarized again. Solar reflectance is generally considered to be small in the LWIR, but in the case of specular reflection, it still must be considered.

Classifying Metals and Dielectrics.

In the late 80s and early 90s, Wolff developed a method for distinguishing metals from dielectric materials using polarization [47, 101, 102, 103]. His approach was based on the assumption that dielectric surfaces polarize light more strongly than metal surfaces. This is generally a good assumption as the reflectance of metals, at wavelengths longer than the UV, is usually very high for both polarization states. This leads to a minimal contrast between polarization states and thus a minimal polarization signature. By measuring a surface at a number of different linear polarizer angles, he found the maximum and minimum intensity passing through the polarizer. Then, a "Fresnel ratio" is defined as I_{max}/I_{min}. Anything with a ratio above 2.0 is classified as a dielectric, while anything below 2.0 is considered a metal. This procedure was shown to be effective for a variety of different scenes, however, it does not seek to actually identify the materials in the scene, it only classifies them into two categories.

Tominaga and Kimachi proposed another technique for distinquishing metals from dielectrics using imaging polarimetry [104]. They examined how the degree of polarization varied spatially around a specular highlight from cylindrical metal and dielectric surfaces. They found that for dielectrics, the degree of polarization maps were convex around the specular highlight, while for metals they were flat or concave.

From this, they were able to create a binary classifier to determine whether a material was metal or dielectric in nature. Again though, while this is useful to obtain basic information about a surface, identifying a material usually requires more information than solely whether it's a metal or not.

Mueller Matrix Classification.

A group at the AFRL Munitions Directorate characterized the polarimetric reflectance properties of six common building materials: rubber, shingle, plywood, drywall, brick, and concrete [105]. They started by measuring the Mueller matrices and BRDFs of the materials at several different wavelengths between 700 nm and 2.3 μm. From the Mueller matrices, they extracted information about material reflectance, degree of polarization, and retardance. They used this information to form feature vectors, which was passed through a support vector machine classifier (See previous section) to determine material classes. Measurements of an unknown material are then classified according to the class that their feature vector most closely resembles. When using all three parameters of the feature vector, they were able to correctly classify all six materials at least 89% of the time. In remote sensing applications, however, it will may be difficult to obtain *a priori* knowledge of material BRDFs and Mueller matrices. Basic materials, such as concrete, can have many different compositions, which will change their reflectance properties. Additionally, the BRDF may change with how the material surface is finished.

Zallat et. al. proposed another technique using Mueller matrices to classify a material [106]. Instead of measuring the matricies before hand, they used an active, polarized, illumination source. They measured the Mueller matrix of the target on a pixel-by-pixel basis and then cluster the image based on the measured Mueller matrix components. Classification based strictly on the components of the Mueller matrix

proved fruitless because certain elements are highly correlated with one another. So, they used a number of different techniques to decompose the Mueller matrix to extract information useful to classification. They did not present a quantitative assessment of the success for their method, but based on the figures in their paper, it appears to be about 75 % accurate. This method would be much more difficult to implement in the LWIR, however, because other sources of radiance would have to be decoupled first. Additionally, is not passive technique, so it requires an active source to evenly illuminate an entire scene, which may be impractical.

Goldstein and Cox measured the spectral and polarimetric properties of many different varieties of vegatation in the near-infrared (NIR) [107]. They examined both reflection and transmission properties at various angles. A full Mueller matrix was measured by illuminating the sample with different polarization states and measuring the polarization of the reflected or transmitted light. They found that in spectral regions where water absorption is strong, the surface looked more mirror like and the spectral behavior of the leaf were more apparent in the Mueller matrix. They attributed this to there being a greater portion of the radiance reflected from the surface as opposed to scattered within the leaf, then reflected back. This scattering depolarized the light, which makes all but the first element of the Mueller matrix zero. While they did not seek to classify actual images, they found differences between plants in some spectrally resolved Mueller matrix components.

Zhao et. al. classified materials based on measuring the Mueller matrix reflectance of materials relative to some known reference material in the scene [68], [108], [109]. Their work was done in the visible, with only the sun and sky used as an illumination source. Because of this, they assumed the incident radiance was unpolarized, which means only three terms of the Mueller matrix need to be solved for. The three spectrally resolved elements and two derived elements, degree and angle of polarization, as

used to classify materials. A support vector machine classifier is used to group pixels into classes. Classification based solely on the multispectral data is over 99% accurate in sunny conditions, but drops to 55% under cloudy conditions and under 50% in the dark. Classification based on both spectral and polarimetric Mueller matrix reflectances greatly improve the accuracy under cloudy and dark conditions, 91 and 83% respectively, though accuracy in sunny conditions is reduced to 95%. While this demonstrates the utility of combining hyperspectral and polarimetric classification parameters, in a typical scenario, it is unlikely there will be perfectly diffuse target, with known reflectance, in a scene for to use for calibration. Working in the LWIR will also likely provide better night-time classification performance.

3.8 Remotely Measuring Index of Refraction

With additional analysis, polarization can be used to determine the index of refraction of a material, as well as other information about the scene. Index of refraction is a convenient quantity to use for classification because it does not depend on illumination conditions, look angle, or other factors than can complicate classification. One common theme with all work presented in this section is that index of refraction retrieval tends to be very noisy. The index of refraction retrieval method presented in this document improves on this by using a fitting model which utilizes the correlation between index of refraction at different wavelengths.

Hong.

Hong measured the index of refraction of water from ultraviolet to microwave wavelengths using emissivity measurements [110]. He used an approximation for the

relationship between the s- and p-polarization reflectances,

$$\rho_s = \rho_p^{1/\cos^2\theta}. \tag{63}$$

The polarized reflectance is related to the unpolarized emissivity by

$$\epsilon = 1 - \frac{\rho_s + \rho_p}{2}, \tag{64}$$

which, in conjunction with Equation 63, can be used to solve for the polarized reflectance terms using unpolarized emissivity measurements. The Fresnel equations for reflectance are then inverted to solve for index of refraction. The approximation, however, introduces a bias into the measured index of refraction values. Including polarimetric information eliminates the need for this approximation.

Thilak et. al..

Thilak et. al. explored simultaneously estimating both index of refraction and surface normal angle [111, 112, 113, 114, 115, 116, 117, 118, 119]. It was assumed that the sensor was in the plane of reflectance and the angle between source and observer was known. The Priest-Meier (pBRDF) was used to account for rough surfaces. Experiments were done by moving the source to a variety of different angles of incidence. An imaging polarimeter was used to generate Stokes vector image by taken ten images through a linear polarizer rotated in 15 degree steps. Spatial averaging was also employed to reduce noise.

Their method first estimated the index of refraction, then used this effective index of refraction to calculate the surface normal angle. Results for surface normal angle were very accurate, usually within a few tenths of a degree. Measured index of refraction values, however, were generally far less accurate, varying from the true value

by as much as 45% for the real component and 400% for the imaginary component. Additionally, while the estimated index of refraction was often robust to changes in reflection angle, there were certain materials where it varied by 30% going from a reflection angle of 45 degrees to 60 degrees.

Moreover, because this work was done in the visible (650 nm), self emission from the target could be neglected. This is not the case in the LWIR, which adds an additional complication to deal with, but also allows for night-time applications. The research presented in this document extends this work to the LWIR, while getting more accurate estimates for index of refraction. Because surface normal can be measured accurately using other techniques, such as LIDAR, it is assumed for most of the research presented here that the surface normal is known *a priori* and only attempt to estimate index of refraction. The other addition made to this past work is to incorporate hyperspectral information, measuring at many wavelengths and thus providing additional utility in material identification.

Hyde.

Hyde extended this work to consider images which were degraded by atmospheric turbulance [120], [121]. The LeMaster-Cain polarimetric maximum-likelihood blind deconvolution algorithm was modified and used to remove atmospheric distortions in order to better classify unknown materials. The algorithm gives the object radiance, DoLP, AoP, and the image point spread function (PSF) based on polarized radiance measurements which have been distorted by the atmophere. The index of refraction is fit to best minimize the difference between measured and theoretical DoLP. Because the reflectance of metals is very high for both polarization states, even in the NIR, DoLP values were small and noisy, making index of refraction retrieval difficult. Again, this work was done at a single wavelength in the NIR, where self-emission

can be neglected, whereas the research presented in this document uses hyperspectral imagery in the LWIR.

Huynh et. al..

Huynh *et al* used multispectral imagery from a single viewing angle to extract both surface normal and index of refraction [122]. As with some previously reviewed papers, they fit a sinosoid to the intensity measured at a number of different polarizer angles to solve for I_{max}, I_{min}, and the angle of polarization. While only three polarizer angles are needed to solve the problem, they used more to make the system overdetermined and reduce the effect of noise. The azimuthal angle of surface normal with respect to the sensor is given by the angle of polarization. To reduce noise in this quantity, they perform the weighted average of the spectrally resolved angle of polarization. The weights are determined by the residual amounts in the sinosoidal fit to measurements at different polarizer angles.

To solve for index of refraction and zenith angle, they utilize Fresnel's equations to find

$$\frac{I_{min}}{I_{max}} = \left[\frac{\cos\theta\sqrt{n(\lambda)^2 - \sin^2\theta} + \sin^2\theta}{n(\lambda)} \right]^2. \tag{65}$$

Notice that they ignore the imaginary component of index of refraction. Since they are working with various glasses at visible wavelengths, this can be a safe approximation, but it will not always be the case. Even so, however, there are still more unknowns than measurements as n must be solved spectrally. To eliminate this issue, they use the Cauchy dispersion equation

$$n(\lambda) = \sum_{k=1}^{M} C_k \lambda^{-2(k-1)}, \tag{66}$$

where C_k are now the coefficients to solve for. For their measurements, they use five coefficients.

They tested this on a set of synthetic data using 30 equally spaced bands between 430 and 720 nm measured at five different polarizer angles. They tested their method at a variety of different illumation positions, on a variety of different targets, and for each they calculated the spectral angle between the measured and true index of refraction as their performance metric. For all targets and illumination conditions, the error in spectral angle was never greater than two degrees. Shape estimation was less accurate, however, with errors exceeding 20 degrees for some targets.

There are many similarities between this work and the proposed research, but they use several assumptions that will not always hold true. First, they ignore the imaginary component of index of refraction, which can play an important role in the polarization signature of many materials. Another difference is that, while they incorporate a model to reduce the dimensionally of the spectrally varying index of refraction, their model is a simple polynomial fit to the data as opposed to something based in real physics. This polynomial fit works well where index of refraction is relatively smooth, but in regions near resonances, the index of refraction is hard to model with a simple polynomial. Finally, they only determine the effective index of refraction stating that it may be off by some scaling factor, which is why they use the spectral angle as a metric. In many applications this may be sufficient, but when using an intensity-based classification metric this would yield an inaccurate result.

Fetrow et. al..

A group from AFRL and Applied Technology Associates demonstrated that index of refraction can be estimated in the LWIR, using two different techniques. First, they measured the S_3/S_2 ratio for glass, metallic, and painted surfaces in the LWIR [123].

Their data was not hyperspectral, instead measuring an effective index of refraction band-averaged over the 8.5-9.5 μm spectral range. Additionally, the source used was blackbody radiance passing through a linear polarizer, such that $\vec{S}_{in} = [1 \ 0 \ -1 \ 0]^T$, making this an active technique. In most natural scenes $S_3 \approx 0$ [28], however, so this technique would be difficult to implement without an active source.

Their second technique is more relevant to the work presented here. They created a model to predict index of refraction based on polarized radiance measurements assuming knowledge of downwelling radiance being reflected off a sample, with known temperature and surface roughness. They first tested their model in laboratory conditions using a hemispherical dome to control the radiance being reflected off the target. Careful measurements of the dome and sample surface temperatures were taken. Two glass plates, one smooth and the other with a roughened surface were used. The samples were measured, using a single pixel FTS with a quarter waveplate and linear polarizer mounted in front, at 12 different angles relative to the sensor ranging from normal to $80°$. It was found that S_0 decreased with increasing angle, while S_1 became increasingly negative. This is expected because the dominate radiance source was self-emission of the target. S_2 and S_3 were negligible for this setup. They considered two cases, one for a smooth surface, the other incorporating the Torrance and Sparrow BRDF to account for roughened surfaces. To solve for index of refraction, they used a fitting algorithm to minimize the error metric

$$\chi^2(n, \kappa, \sigma, \lambda) =$$
$$\frac{1}{2N_v-1} \sum_{\theta_v} \left(\frac{S_{0,data}(\theta_v) - S_{0,T-s}(n,\kappa,\sigma,T_d,T_s,\theta_v)}{\Delta S_0(\lambda)} \right)^2 + \left(\frac{S_{1,data}(\theta_v) - S_{1,T-s}(n,\kappa,\sigma,T_d,T_s,\theta_v)}{\Delta S_1(\lambda)} \right)^2.$$
$$(67)$$

N_v is the number of different angles measured. $S_{0,T-S}$ and $S_{1,T-S}$ are those quantities as predicted by the Torrance and Sparrow model for a given index of refraction, surface roughness (σ), dome temperature (T_d), sample temperature (T_s), and angle

(θ_v). It was assumed that a surface roughness parameter, σ, was known. ΔS_0 and ΔS_1 are varied to weight either S_0, S_1, or different wavelengths [124].

In order to get all wavelengths to fit to a realistic value, the constraints on the fit had to be loosened. This lead to very large error bars, exceeding ± 1 for both n and κ at some wavelengths. Additionally, while the index of refraction of the material should not, in principle, change with surface roughness, their predicted values did, especially at longer wavelengths [124].

They then measured the same targets outside. The samples were set to an angle of $40°$ and their measured temperature was $50.5°$C. MODTRAN was used to model the atmospheric downwelling radiance. Their results generally showed good agreement between the measured and predicted values of S_0 and S_1 for most wavelengths. The one exception was the predicted S_1 signature for the smooth glass showed consistantly more polarization than was measured. Interestingly, the amount of polarization measured did not seem to change much between the smooth and roughened glass [124]. The authors don't offer an explanation of this, but other unrelated work [125] has shown that it can be difficult to highly roughen surfaces, relative to LWIR wavelengths.

Finally, they ran simulations of how the predicted signatures are expected to change with varying atmospheric parameters, sample temperatures, and viewing angles. First, they varied the downwelling radiance by assuming three different atmospheric models, midlatitude summer standard clear, midlatitude winter standard clear and midlatitude summer standard with cumulus clouds. As expected, the highest S_0 is measured with cumulus clouds, which act as a blackbody in the LWIR, the lowest S_0 is measured for the winter atmosphere. Because thermal contrast is one of the important factors in the amount of polarization observed, the atmopheres with larger downwelling radiance showed less polarization. The second simulation varied

the temperature of the sample to 47, 50, and 53°C. Again, since thermal constrast is important, the warmer the sample, the larger the polarization signature, as well as the total radiance. The final simulation examined sensor declination angles of -40°, -30°, -25°, and -20°. Again, as expected the total radiance drops, but the polarization increases as the angle relative to the target surface normal increases [124].

There are many similarities between this and the proposed research, but there are some key differences. One issue was that their calculated values for index of refraction were shown to be highly suceptible to errors in the input parameters [124]. In many applications, these parameters, specifically surface temperature and roughness, will not be known. The research presented in this document will estimate material parameters without the need for *a priori* knowledge of the surface temperature. Finally, even with accurate inputs, their retieved values were very noisy. To mitigate this issue, in the work presented here, physics-based models are used to fit index of refraction. In addition to reducing some of the noise effects that were observed in this group's reasearch, it will also reduce the number of parameters needed to fit index of refraction. This will enable adding additional parameters to the fit, such as surface temperature and downwelling radiance, so these parameters may need not be determined with high accuracy in advance.

IV. Index of Refraction Fitting Routine

With the forward model developed, a fit can be performed solving for parameters describing the reflectance, downwelling radiance, and object temperature which best replicate the measured Stokes parameters. For most of this research, it is assumed that the elevation angle, θ, is already determined by some other method such as LIDAR, stereo imaging, etc. Often times, multiple viewing geometries are used to further constrain the index of refraction retrieval. An error metric is defined in terms of the Frobenius norm of the difference between measured and modeled:

$$E(\mathbf{x}) = \sqrt{\sum_i \sum_j |S_{0,mea}^{ij} - S_{0,mod}^{ij}(\mathbf{x}))|^2} + \sqrt{\sum_i \sum_j |P_{0,mea}^{ij} - P_{0,mod}^{ij}(\mathbf{x})|^2} \qquad (68)$$

$\mathbf{x}$ is a vector containing the parameters of the fit describing index of refraction, object temperature, and downwelling radiance. P is a quantity describing the total polarization which will be discussed in more detail later in this section. There is also an option in the code to only use S_0 or P when calculating the error function but the default is to use both. The rest of this section will elucidate some of the finer details of how index of refraction is solved for in this research.

4.1 Modeling Index of Refraction

One of the key aspects of this fit is reducing the number of parameters needed to describe the index of refraction. This is done by incorporating physics-based models. As discussed above, the Lorentz oscillator model describes the spectal dielectric constant as one, or a number of, "oscillator(s)." Mathematically, this can be expressed as:

$$\varepsilon(\nu) = \varepsilon_\infty + \bar{\nu}_p^2 \sum_{j=1}^{J} \frac{f_j}{\bar{\nu}_{0,j}^2 - \bar{\nu}^2 - i\Xi_j \bar{\nu}} = \varepsilon_1 + i\varepsilon_2. \qquad (69)$$

64

ε_∞ is a real-valued constant representing the value of ε as frequency goes to infinity. ν_p is the plasma frequency of the material, f_j is the relative strength, ν_j is the resonant frequency, and Ξ_j is the damping coefficient of the jth oscillator. From this expression for the dielectric constant, the index of refraction can be solved for using Equation (5). The refractive index can be used to describe the reflectivity of the material using Equation (16).

While the Lorentz oscillator model does very well describing pure crystalline materials, amorphous materials tend to have broader, more slowly varying refractive indices that are difficult to describe with a sharp oscillator. A number of different models exist to better describe amorphous materials, see [126, 127, 128] for some examples. Many of these have been tested as part of this research but tend to be either slow and/or inaccurate. Instead a method is proposed to solve for the imaginary component of index of refraction at a few equally spaced points (or knots) in the band and then use MATLAB's [129] PCHIP (Piecewise Cubic Hermite Interpolating Polynomials) function to interpolate between these points. The Kramers-Kronig relationship is then used to solve for the real component of index of refraction.

In principle, the Kramers-Kronig relationship requires knowledge of the spectrum from zero to infinity in frequency space. Features in the imaginary component far away from the band, however, have only a small effect on the behavior of the real component in-band so assuming the imaginary component is zero far out-of-band is a reasonable approximation. Forcing the imaginary component to be zero everywhere out of band produces errors near the band edge, however, so a linear extrapolation is used, extending 5 knot spacings out-of-band on either end of the spectra. If the extrapolation leads to negative values, the imaginary component is set to zero at these points. Figure 9 shows the results of fitting a sample index of refraction both with and without doing this extrapolation. This clearly shows a dramatic improvement in the

65

fit when extrapolation is used. There are still some errors near the instrument band-edge, but these are unavoidable since the out-of-band index can't be truly known.

To enforce Kramers-Kronig, the imaginary component of the Hilbert transform is used as shown below:

$$\mathrm{n}(\bar{\nu}) = -\mathrm{Im}\left\{ \frac{1}{\pi} \int_{-\infty}^{\infty} \frac{\kappa(\bar{\nu}')}{\bar{\nu} - \bar{\nu}'} d\bar{\nu}' \right\} + n_{\infty}. \tag{70}$$

where

$$\kappa(\bar{\nu}') = \begin{cases} 0 & \bar{\nu}' < \bar{\nu}_{min} - 5 \cdot \Delta\bar{\nu} \\ \text{Extrapolate (set to 0 if negative)} & \bar{\nu}_{min} - 5 \cdot \Delta\bar{\nu} < \bar{\nu}' < \bar{\nu}_{min} \\ \mathrm{pchip}(\boldsymbol{\kappa}) & \bar{\nu}_{min} < \bar{\nu}' < \bar{\nu}_{max} \\ \text{Extrapolate (set to 0 if negative)} & \bar{\nu}_{max} < \bar{\nu}' < \bar{\nu}_{max} + 5 \cdot \Delta\bar{\nu} \\ 0 & \bar{\nu}' > \bar{\nu}_{max} + 5 \cdot \Delta\bar{\nu} \end{cases} \tag{71}$$

n_{∞} is a constant that is solved for in the fitting routine and is nominally the value of the real component as frequency goes to infinity. $\boldsymbol{\kappa}$ is a vector of the value of κ at each knot point. Using this, the Stokes vector expression in Equation (28) can be described in terms of variables n_{∞}, $\boldsymbol{\kappa}$, T_e, ϕ, and parameters describing L_d. Figure 10 shows a schematic what this looks like for a sample index of refraction.

This fitting model works well for amorphous materials, but results show it does not perform as well as the Lorentz oscillator model for crystalline materials. Because of this, a method was developed to automatically determine which fitting model to use based on the measured data. The basic concept is that materials with very sharp spectral features in S_0 and P are better described by the Lorentz oscillator model, while materials with broader spectral features can be better described using the PCHIP interpolation method. To test the sharpness, the slope of P is taken at

66
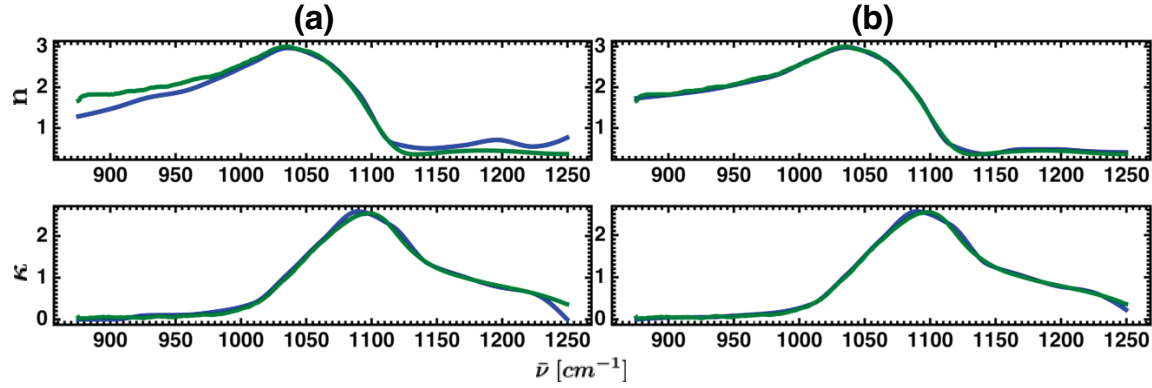
Figure 9. Fitting a sample index of refraction using (a) no out-of-band extrapolation compared with (b) extrapolating out 5 knot points. The effects of truncating the spectra with no extrapolation are clearly visible near the band edge. There is still some error near the band edge but some of this is unavoidable since the index can't be truly known out-of-band.

$$n(\bar{\nu}) = -\mathrm{Im}\left\{\frac{1}{\pi}\int_{-\infty}^{\infty}\frac{\kappa(\bar{\nu}')}{\bar{\nu}-\bar{\nu}'}d\bar{\nu}'\right\} + a$$
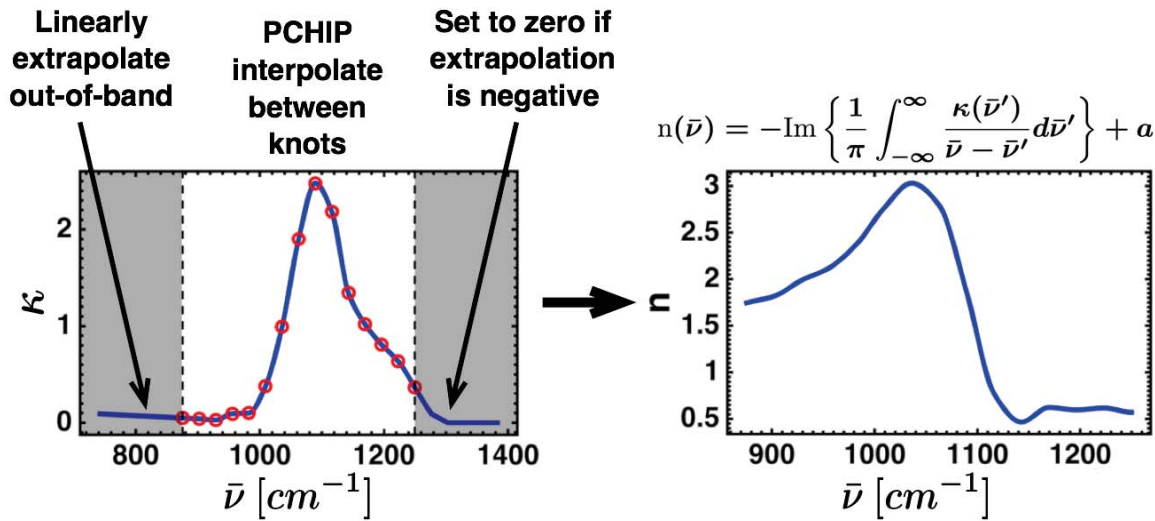
Figure 10. Schematic of how the index of refraction of amorphous solids is modeled for this research.

every spectral point.

$$\frac{P(i) - P(i-1)}{\Delta\bar{\nu}} \qquad \forall i. \tag{72}$$

If this exceeds some threshold, $0.1 \ \frac{\mu W}{cm^2 \cdot sr \cdot cm^{-1} \cdot cm^{-1}}$ is used for the analysis presented here, the Lorentz oscillator model is used, otherwise the PCHIP interpolation is used. This value was found to be a good threshold based on simulated data generated by the system model described below. Atmospheric features may cause this to choose the wrong model so for this research the model and number of oscillators is manually defined when working under atmospheric downwelling conditions. Because the location of these atmospheric features is well known, however, this could be easily corrected in the future.

4.2 Choosing Number of "Oscillators"

In addition to choosing the right model, it is also important, when using the Lorentz oscillator model, to choose the number of oscillators. Choosing too many oscillators increase computational time and can cause the fit to get stuck in local minima. If too few oscillators are used, the fit may not be able to accurately replicate the spectral shape of the index of refraction. To solve for the number of oscillators, the number of peaks in the absolute value of S_1 is used, the supposition being that one oscillator will lead to one sharp peak in S_1. To avoid noise being characterized as a peak, a minimum peak prominence of $0.1 \ \frac{\mu W}{cm^2 \cdot sr \cdot cm^{-1}}$ is used. This value was chosen to be well above the noise of the instrument (see next section) but still small enough to account for relatively weak polarimetric features. The location of each peak is chosen as the starting guess for the oscillator center $\bar{\nu}_0$ as well. The number of oscillators can also be manually set, in which case they are equally spaced between 700 and 1350 cm^{-1}.

Based on experience using the PCHIP interpolation model, it seems that around

15 knot points work best. For this work, it does not appear using more knots provides any significant improvement in the retrieval compared to the increase in fitting time so no automatic means of determining number of knots has been developed.

4.3 Total Polarization

Equation (28) shows the relative amount of energy in S_1 and S_2 depends on ϕ, which is the azimuthal angle of the sensor relative to the plane of reflectance. Because targets in the LWIR are rarely illuminated by a single dominant point source, the plane of reflectance can be a rather ambiguous term, making it desirable to eliminate the ϕ term. Adding S_1 and S_2 in quadrature gives a "total polarization", P, where:

$$P = \frac{1}{2}\tau_a(\bar{\nu})\left(\rho_s(\bar{\nu}, \theta) - \rho_p(\bar{\nu}, \theta)\right)\left(L_d(\bar{\nu}) - B(\bar{\nu}, T_e)\right). \tag{73}$$

This quantity is very similar to DoLP, but without using S_0 to normalize. Having a normalized quantity is not a necessity to the fitting routine so dividing by S_0 only adds an additional source of noise.

An issue arises when calculating P from measurements of S_1 and S_2. Adding S_1 and S_2 in quadrature means the measured P will always be positive, while the modeled P, given by Equation (73) can be either positive or negative. To mitigate this issue, the sign of the largest in magnitude between the spectrally-averaged S_1 and S_2 is applied to P. For example, if S_1 is positive and S_2 is negative, and the magnitude of S_2 is greater than S_1, then P will be negative. For outdoor scenarios, the signature will almost always be emission dominated so this sign ambiguity becomes virtually irrelvant. In this case, however, the sign of P and more specfically the AoP introduced earlier can give information about the orientation of an object.

Another potential problem with using P is that, since it is strictly positive before

the sign is applied, any noise as the S_1 and S_2 measurements approach zero will be additive. As P approaches zero, this produces a biasing to the measured P values which is dependent on the sensor noise. Figure 11 shows this effect and how it can bias spectral measurements for various noise levels.
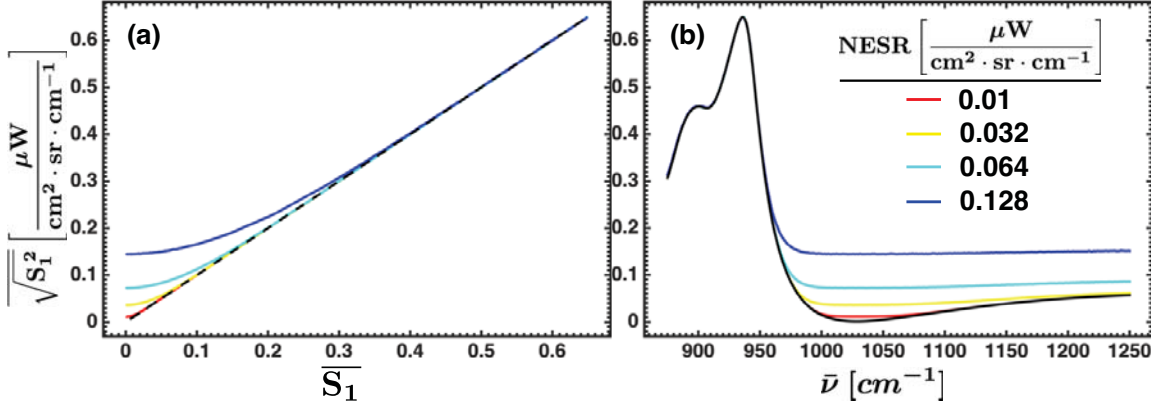
Figure 11. (a) As P approaches and goes below the noise level of the instrument, a bias is introduced into the measurement. (b) shows shows the effect this can have on a measured total polarization spectrum.

One possible way to address this is to ascribe a sign to each spectral channel of P. As was shown earlier in this section, whenever P is positive the downwelling radiance must be greater than blackbody radiance at the temperature of the object and when P is negative the opposite is true. This leads to a dramatically different solution when P is positive as opposed to negative, even if the magnitude of P is very small. Essentially, if the sign of P is wrong, the fit will try to make the reflectance spectra look like the emissivity spectra for the material and vice-versa which drastically changes the index of refraction. Noise may cause a sign flip when P is near 0. Because of how important it is to get the sign correct, the same sign is applied to each P value at every spectral point and angle used in the fit. Additionally, in order to do this one must be very sure that there is no appreciable scene drift that could bias S_1 and S_2 measurements to change from positive to negative or vice-versa. The simplest solution is to simply

70

ignore P values that fall below some threshold and at these points only use S_0 in the fit as described above. The threshold value will depend on the noise characteristics and settings of the sensor being used. Results using some of these corrections will be shown later in this document, but most of the analysis presented forces P to have the same sign for all spectral points/viewing angles and does not threshold these values.

4.4   Defining Temperature Limits

It is also important to have a reasonable starting estimate for surface temperature and, when dealing with indoor measurements, a downwelling temperature. For indoor measurements, Equation (73) can be exploited to automatically determine temperature limits from the data. In this case $L_d = B(T_d)$, where T_d is the downwelling temperature. The Fresnel equations dictate that $\rho_s \geq \rho_p \ \forall \ n \geq 0, \kappa \geq 0, \theta$; so if P is positive, $T_d > T_e$ and vice-versa. From here, it can be derived that when $T_d > T_e$, S_0 must be greater than a blackbody at T_e and less than a blackbody at T_d. The lowest spectral brightness temperature of S_0 defines the upper limit for T_e and the highest spectral brightness temperature defines the lower limit for T_d. Likewise, in the case where $T_e > T_d$, a lower limit for T_e and upper limit for T_d can be defined. The other temperature limits are defined as 50 K greater than a lower bound, or less than an upper bound. The initial estimate for temperature is set to be in the middle of the bounds.

When measurements are taken under atmospheric downwelling conditions, $B(T_e)$ will almost always be greater than L_d. The temperature limits on T_e, described above for the case where P is negative, can still be used. Right now, no limits from the raw data are placed on the lookup table of atmospheres used to describe L_d. There is, however, an option to manually fix one, multiple, or all of the atmospheric parameters used in fitting. There is also the option to manually define a downwelling

71

spectrum not described by any of the atmospheres used in fitting. If L_d is greater than $B(T_e)$, this is an indication that adjacency effects may be contributing significantly to the observed radiance and assuming a blackbody-like downwelling may be the more appropriate model.

4.5 Fitting Algorithms

It is also worth considering how best to search the parameter space to minimize the error function given in Equation (68). Three search options have been incorporated into this method, one gradient-based, one non-gradient-based, and a hybrid of the two. Gradient-based methods are relatively fast but susceptible to getting stuck in local minima. For this work, the gradient-based technique is the quasi-newton method from MATLAB's nonlinear least squares fitting toolbox. Non-gradient-based methods are slower but far less susceptible to local minima, for this work a bounded version of the Nelder-Mead simplex maximization method is used as implimented in MATLAB's *fminsearch* function. A potential solution is to use a hybrid of the two approaches. The search starts with a non-gradient-based search, then after some stopping criteria is met, the parameters obtained from this fit are used as the starting estimate for a gradient-based method. The idea being that the non-gradient-based method will get close enough to the global minimum to allow the gradient-based method to avoid local minima. To save time, the stopping criteria of the non-gradient-based method must be relaxed. In the case of this code, a maximum number of iterations (200) is set after which the gradient-based method will take over.

Figure 12 shows the minimum value of the objective function found for each of the three methods applied to the beaker data described later. This shows that the quasi-newton fitting method generally performs best, but occasionally gets caught in local minima. Bounded fminsearch is usually worse, but it is far less susceptible

72
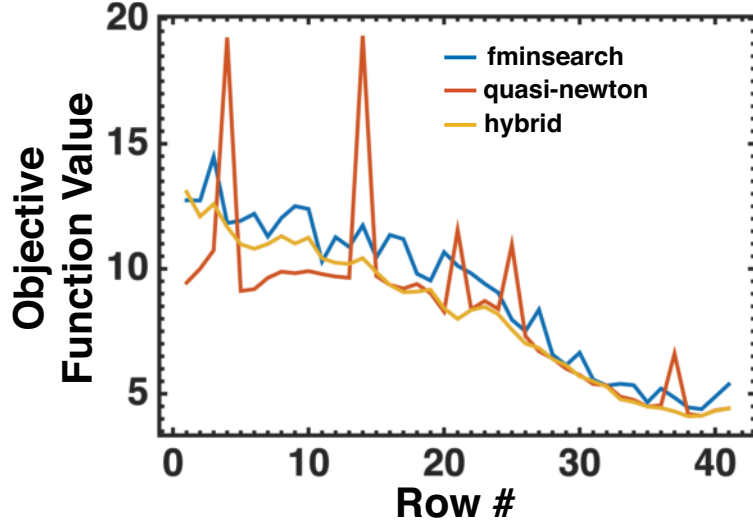
Figure 12. Comparison of the objection function value when the fit has arrived at a solution for the three fitting routines used in this work.

to converging to wildly inaccurate solutions. The hybrid method seems to strike a balance between these two. As a general rule, it seems best to use the quasi-newton method when using the PCHIP interpolation model and bounded fminsearch when using the Lorentz oscillator model. The hybrid fit is also used occasionally where noted.

4.6 Solving for Downwelling Radiance

For this research, there are two cases to consider when fitting the downwelling radiance: first, measurements taken in a lab and second, measurements taken outdoors. In the first case, it is assumed that most objects in the room are at the same temperature, making the downwelling radiance blackbody-like. In some instances, a blackbody is used to illuminate the object to enforce this assumption. If the downwelling radiance is blackbody-like, one variable, a "downwelling temperature," is all that is needed to describe the downwelling radiance reflected off an object. This

downwelling temperature is added as a parameter into the fitting routine and solved for.

The second scenario is more complicated. Atmospheric downwelling is too complex and spectrally structured to properly describe using only one parameter. There are, however, atmospheric models that can reasonably predict downwelling radiance based on a few inputs describing the state of the atmosphere. This work utilizes MODTRAN [130], which is one of the most common atmospheric radiative transfer models. There are hundreds of different inputs into this model, but many have either no or very little effect on the downwelling radiance in the LWIR. In total, four parameters were chosen as they seem to have the greatest effect on the downwelling radiance: air temperature at ground level, temperature lapse rate, water vapor concentration at ground level, and the ozone concentration scaling factor.

Ground temperature, water vapor concentration, and ozone scaling were all varied in 20 equally spaced steps. The temperature lapse rate was varied more coursely with 5 values. A range of resonable values for each of these parameters was found by examining 10 years of atmospheric radiosonde profiles for the NOAA weather station in Wilmington, Ohio.

From these radiosonde datasets, it was determined that ground temperature should vary from 0 to 35°C, water vapor from 1000 to 9999 ppmv, and temperature lapse rate from 4 to 7 K/km. Instead of equally spacing the temperature lapse rate values, integer steps were taken from 4 to 7, then 6.5 was included as it corresponds to the temperature lapse rate of the 1976 US Standard Atmosphere. The maximum value for the water vapor concentration was chosen because MODTRAN doesn't allow for values over 9999 ppmv. This corresponds to a dewpoint of about 7°C at standard ground atmospheric pressure. The lowest water vapor concentration corresponds to a dewpoint of -20°C, which is around the lowest value seen in at ground level in the

NOAA radiosonde data. Figure 13 shows the altitude profile of temperature and water vapor concentration for every radiosonde profile measured from 2005-2015 as well as the pressure profile. Pressure is not included as a fit parameter because it is relatively constant day-to-day. The ozone scaling factor was varied from 0.5 to 2. This was chosen as a reasonable range based on a paper describing the seasonal and daily variations in ozone [131].
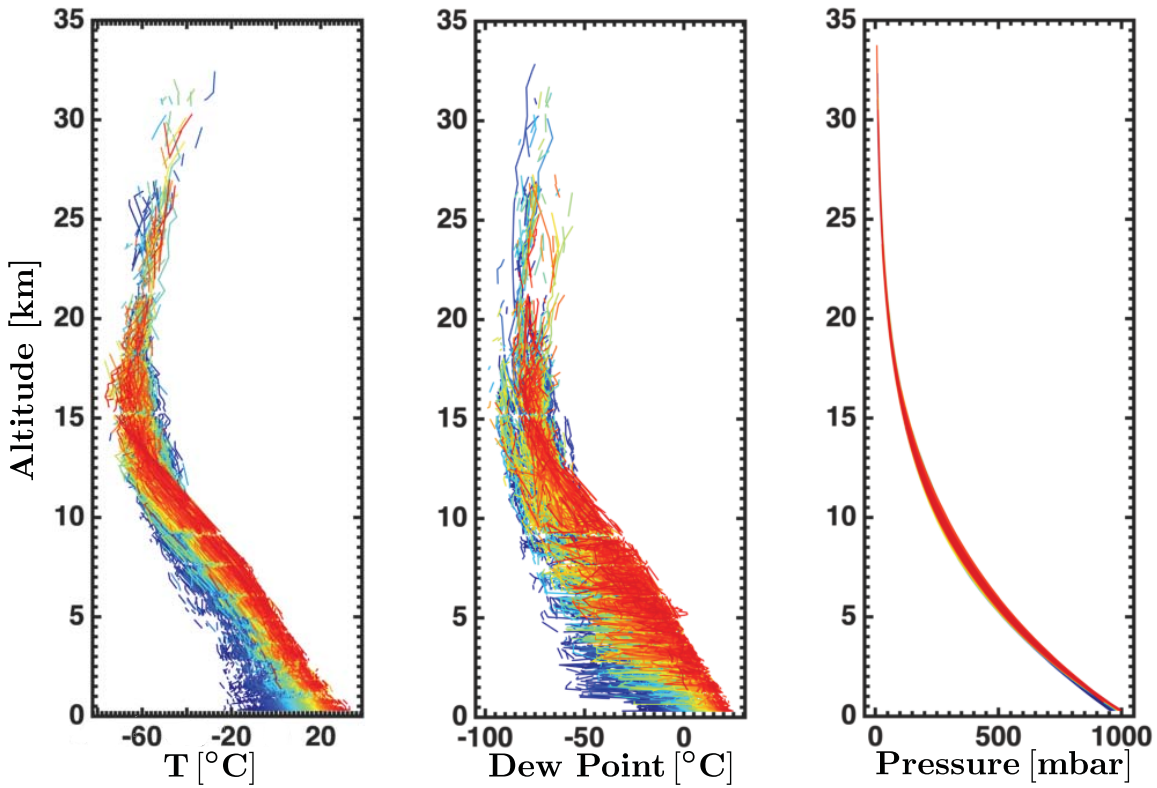
Figure 13. Plot of the altitude profile of temperature, dew point, and pressure for every sounding profile taken between 2005 and 2015 from the Wilmington, OH NOAA site. The temperature and dew point can vary significantly day-to-day meaning they have to be fit to accurately describe the state of the atmosphere on a given day. Pressure will also have an effect on the atmospheric transmission, path radiance, and downwelling radiance, but this figure shows that the pressure profile is very consistent day-to-day so pressure is not included as a parameter.

It is important to determine how both temperature and water vapor concentration vary with altitude. The temperature is somewhat straight-forward as both a ground

75

temperature and a lapse rate are fit. The atmosphere, however, starts to warm again starting around an altiude of 20 km, meaning a single lapse rate cannot fully define the temperature profile. To fix this, the temperature is fit using the determined ground temperature and lapse rate up to an altiude of 20 km, then the 1976 US Standard Atmosphere values for temperature as a function of altitude are used for everything above 20 km. It is also evident from Figure 13 that the temperature seems to reach a minimum value and plateau there regardless of ground temperature and/or temperature lapse rate. In order to account for this, all temperature values below 20 km altitude and below 216.7 K were set to 216.7 K. This corresponds with the lower bound set by the ISAC atmospheric correction algorithm [132]. The other important piece is to determine how water vapor scales with altitude. For this, pieces of the ISAC algorithm are again used. Their work determined a function describing the water vapor profile as a function of altitude, z, and water vapor concentration at ground level, C_0:

$$
C_{H2O}(z) = \begin{cases} C_{std}(z) \left[1 + \left(\frac{C_0}{7330} - 1 \right) \left(1 - e^{-0.8(16-z)} \right)^6 \right] & z \leq 16 \, \text{km} \\ C_{std}(z) & z > 16 \, \text{km} \end{cases} \tag{74}
$$

C_{std} denotes the water vapor concentration as a function of altitude given by the 1976 US Standard Atmosphere. Each of the four parameters are varied independently and MODTRAN is run for each of these settings generating a 5-D tensor, 4 dimensions for the variables and one for the spectral axis. A total of 40000 different atmospheric downwelling profiles are generated. This same treatment can also be used to solve for atmospheric transmission and path radiance, but this research is done at short ranges so atmospheric tranmission is presumed to be one and path radiance is presumed to be zero.

V. Results

5.1 Simulated Data

To start, a series of simulated datasets were created to test how the index of refraction retrieval technique described in the previous section performs under a variety of different laboratory conditions. Under laboratory conditions, the downwelling radiance is modeled as a blackbody at some temperature. For these datasets, the temperature contrast between target and background, sensor noise, and spectral resolution are varied, as well as using different combinations of viewing geometeries. Table 1 shows a summary of the different settings used to generate each of the synthetic datasets. An exemplar index of refraction is forward modeled to S_0 and P using these settings. Normally-distributed random noise, based on the noise-equivalent spectral radiance (NESR) setting, is then added to these truth spectra and the retrieval is performed on these noisy spectra. In total, 500 Monte Carlo simulations were performed for each setting. For these datasets, the hybrid search algorithm described in Section 4.5 was used. True quantitative metrics would be highly dependent on sensor characteristics and the engagement scenario. Instead, the goal here is to develop a good qualitative understanding of how some of these parameters affect the retrieval.

Table 1. Summary of simulated datasets used to test the index of refraction retrieval. Here, $[\text{r.u.}] = \left[\frac{nW}{cm^2 \cdot sr \cdot cm^{-1}}\right]$

T_d [K]	T_e [K]	NESR [r.u.]	Viewing Angles	Res. [cm^{-1}]
295.5, 297, 301, 309, 324	294	32	20, 40, 60	1
250	294	32, 45, 64, 128, 181	20, 40, 60	1
250	294	32, 45, 64, 128, 181	20, 40, 60	16, 8, 4, 1, 0.5
250	294	32	{20, 40, 60}, {30, 40, 50}, {50, 60, 70}, {30}, {60}	1

Reducing the contrast, ΔT, between downwelling and object temperature has two primary effects on the data. First, it reduces the overall polarization. In the limit where the $\Delta T = 0$, Equation 73 dictates that $P = 0$. The other effect reducing the temperature contrast has is to mute the spectral features in both S_0 and P. Again in the limit where the temperatures are equal, S_0 will look exactly like a blackbody regardless of the material. It is interesting to consider how the fit performs under both of these conditions. For this and all subsequent synthetic datasets, the retrieval-to-retieval variability, measured by the standard deviation across all retrievals, is used as the comparison metric. The error in the median retrieval is not necessarily an effective metric because the noise is normally distributed. Taking the median across 500 retrievals provides a huge boost to the effective SNR of the measurement, so for almost all settings, the rms error of the median retrieved value is nearly identical. The variability between retrievals is a better metric of the uncertainty in the retrieved value for a single measurement. Figure 14 shows the rms standard deviation in both n and κ as a function of the temperature contrast and the average value of P. It appears that there is an exponential relationship between the temperature contrast — and average value of P — and the retrieval variability.

Another factor to consider is the NESR of the instrument being used to measure the signature. Essentially this leaves both the magnitude of P and depth of the spectral features in both S_0 and P fixed, but varies their weight relative to the noise level of the instrument. This mimics the effect of going from a high-fidelity, low NESR sensor to one with worse noise performance. The 250K downwelling temperature is a very rough approximation of clear sky downwelling. Decreasing the NESR will certainly improve the fit, but it is good to develop a sense of how much fit performance improves relative to NESR differences. Figure 15 shows the results of changing the NESR. The relationship with NESR appears to be roughly linear in this domain.
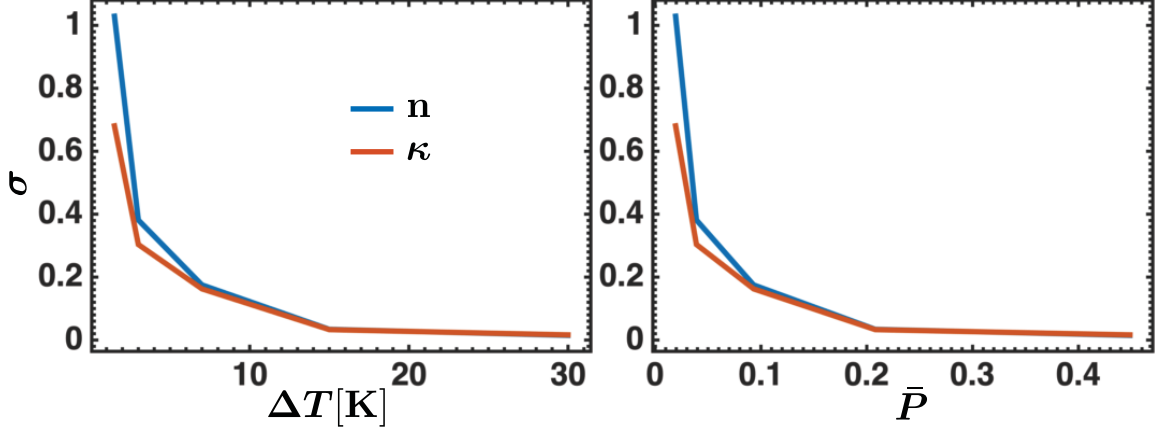
Figure 14. Standard deviation in both the real (blue) and imaginary (red) component index of refraction across all 500 Monte Carlo simulations as a function of contrast between downwelling and object temperature and the average value of P.

Obviously at some point this relationship will break down as variability can't go negative, but this synthetic dataset covers a wide range of reasonable NESR values. It is also evident — based on the standard deviation values — that the sensor NESR has less of an effect on fit performance than the temperature contrast over reasonable ranges.

Spectral resolution is an interesting factor to consider because there are two competing consequences of changing spectral resolution. First, increasing the spectral
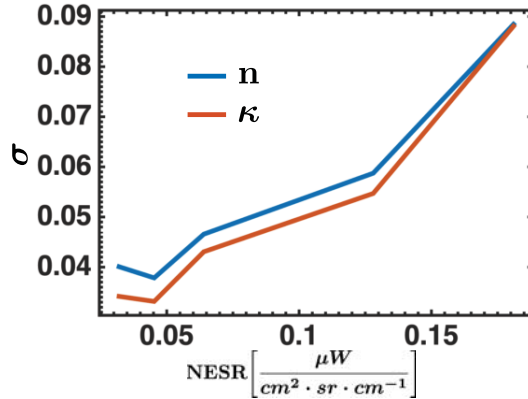
Figure 15. Standard deviation in both the real (blue) and imaginary (red) component of index of refraction across all 500 Monte Carlo simulations as a function of sensor NESR.

resolution increases the number of points used in fitting which in theory should increase the performance of the fit. On the other hand, increasing the number of spectral bands decreases the spectral bandwidth over which each point is integrating thus decreasing the NESR. The settings summarized in Table 1 mimic this effect. Figure 16 shows that spectral resolution seems to have little effect — at least when the downwelling radiance is blackbody-like — on the retrieval over a reasonable range of different spectral resolutions.

The final factor considered in these simulated datasets is various combinations of viewing angle. The primary topics considered are: multiple viewing angles compared to only using a single viewing angle, the effect of changing the relative differences between multiple views, and the effect of increasing the magnitude of the viewing angle (i.e. going further off-nadir). From these datasets it appears that going further off-nadir generally leads to a better fit and multiple viewing angles significantly improves the fit. The spread of angles is also important although it has less of an effect than the overall average magnitude of the angles. For the first case with viewing angles of $20°$, $40°$, and $60°$, the variability was 0.038 and 0.034 in n and κ. When the overall spread of angles used in fitting was reduced — i.e. the second case where viewing
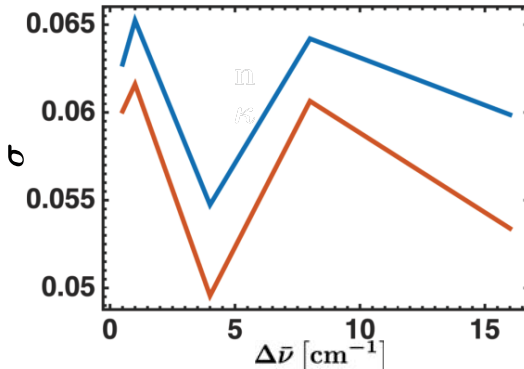
Figure 16. Standard deviation in both the real (blue) and imaginary (red) component of index of refraction across all 500 Monte Carlo simulations as a function of spectral resolution.

80

angles are 30°, 40°, and 50° — the variability increases to 0.080 and 0.074. When the spread is held constant but the overall magnitude of the angles is increased — viewing angles of 50°, 60°, and 70° — the variability drops to 0.029 and 0.028, below both of the previous cases. Finally, when only a single angle is used, the fit performs significantly worse. When only a 30° viewing angle is used, the variability is 0.326 and 0.251. When only a 60° viewing angle is used, the variability is 0.208 and 0.250.

All of these datasets used the index of refraction of quartz glass, which is used later. This material is not well modeled by the Lorentz oscillator model so instead the interpolation method described in the previous section is used. The index of refraction of SiC, also used later, on the other hand does obey the Lorentz oscillator model quite well. Simulated datasets where also created and analyzed using SiC as the material of interest. Identical trends were seen in these SiC datasets, however, that data isn't presented for the sake of brevity.

5.2 Laboratory Data

To start testing this index of refraction retrieval method on real data, a series of experiments were conducted under laboratory conditions. This allowed for a reasonable amount of control over many of the variables that can affect the radiance signature of a target. It is important to have a good understanding of the effect some of these factors might have on the retrieval before moving on to more complicated scenarios.

Pyrex Beaker.

The first dataset collected to test the index of refraction retrieval method was of a Pyrex beaker on a hot plate. Eight datacubes, collected at 8 cm^{-1} spectral resolution, were averaged together. The hot plate provided a contrast between the beaker and

background, without which the beaker would simply look like a blackbody. The hot plate also created a temperature gradient going up the beaker, which changes the relative importance of the reflected versus emitted components of radiance. Finally, going horizonatally across the beaker provides a full range of surface normal angles going from -90° to 90°. In practice, because of image blur, pixels near the edge of the beaker cannot be used, so the usable surface normal angles vary from about -55° to 55°. In total, the usable parts of the beaker in the image is 40 pixels across and 41 pixels high. From this, index of refraction, surface temperature, and the effective temperature of the background reflecting off the beaker are fit.

Figure 17 shows the measured and expected S_0 and P for various points on the beaker. As expected, S_0 is significantly higher at the bottom of the beaker than at the top. S_0 also decreases with surface normal angle because as surface normal increases, reflectivity increases. Also of note is that S_0 spectrum changes significantly going from the center of the beaker to the edge. This change is not a simple linear offset either, further illustrating how emissivity can change with viewing angle in a way that may be difficult to compensate for. The P spectra also help give a qualitative understanding of the problem. Again as expected, P is greater towards the bottom of the beaker because there is a greater temperature contrast from the background. Also, near the center of the beaker when surface normal angle goes to zero, there is very little polarization, consistent with what is expected. There appears to be some biasing in the P measurements which will be discussed later.

From these measurements, the index retrieval is performed one of two ways, either fitting the angle for each pixel independently or fitting each row of the image using all surface normal angles in conjuction with one another as described earlier. First, Figure 18 shows the results of performing the retrieval on each pixel independently. Because of the geometry of the beaker, the index of refraction could not be measured

82
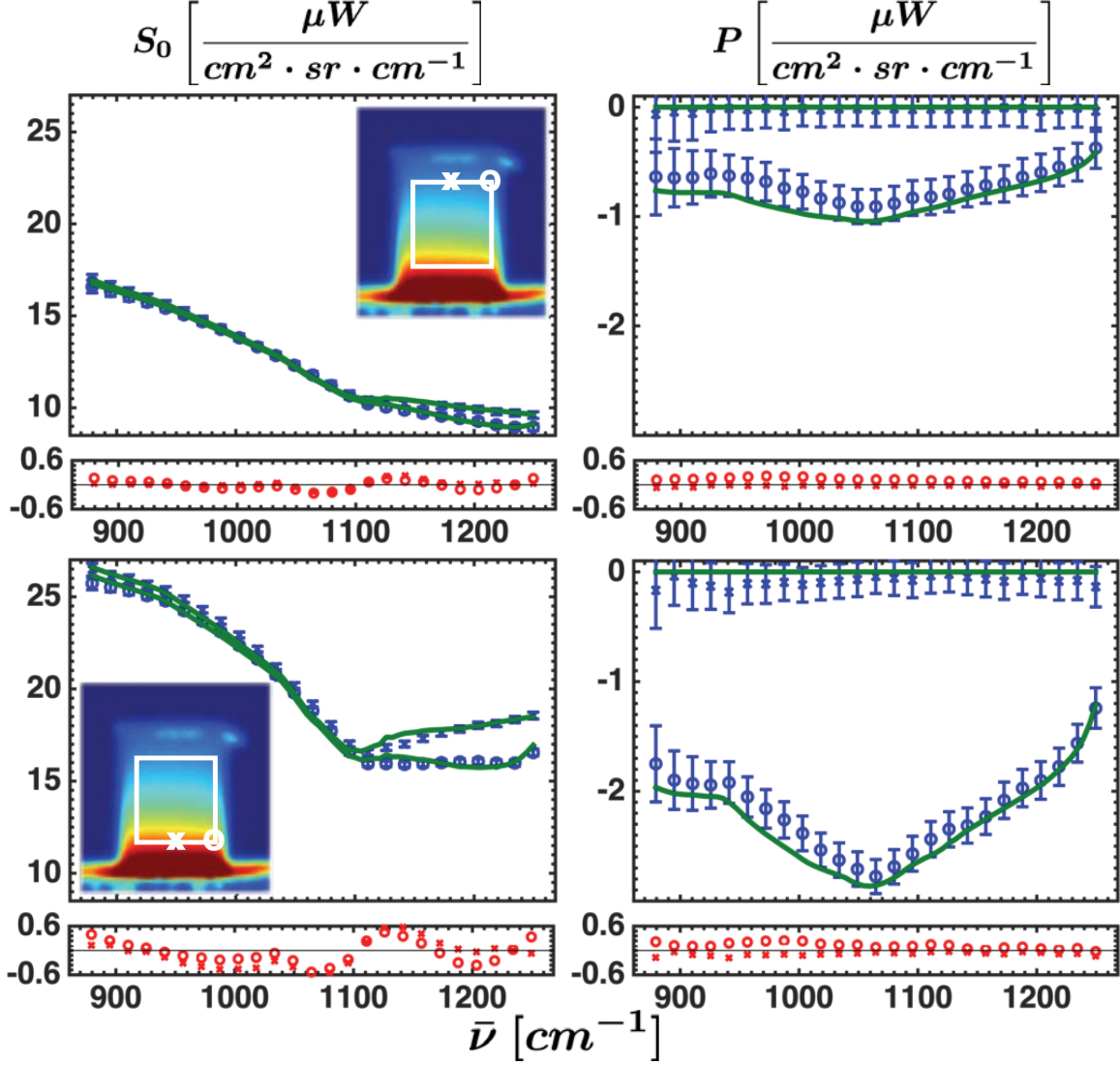
Figure 17. Measured S_0 and P spectra (blue) compared with expected (green) for various pixels of a heated Pyrex beaker. Expected values are generated based on forward modeling the index of refraction of Pyrex taken from [133]. The white symbols on the inlay images show the location of the spectra with the corresponding symbol on the plot. The error bars represent two times the expected noise based on the previously measured NESR of the instrument. [34] The plots in red below each pane represent the residual error between measured and expected. As expected, S_0 increases towards the bottom and decreases towards the left/right edges. P increases with both temperature contrast, i.e. going down the beaker, and surface normal angle, going towards the left/right edge of beaker. Some potential causes for the errors between measured and expected, especially in P will be discussed later.
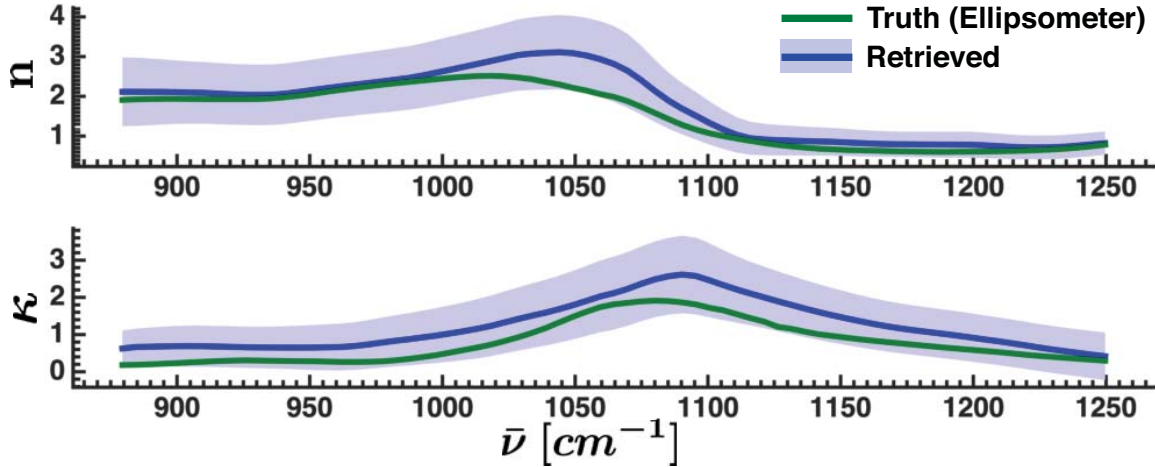
Figure 18. Retrieved (blue) and true (green) index of refraction for each pixel of the Pyrex beaker. The solid blue line represents the median retrieval across all pixels and the shaded blue region represents plus/minus one standard deviation. The green line is taken from ellipsometry measurements. In this fit, P at every angle and spectral point is forced to be negative.

using ellipsometry. Instead, this retrieved index of refraction is compared to one presented in the literature for the index of refraction of Pyrex. [133] The rms error between the retrieved and expected index is 0.339 for the real component and 0.464 for the imaginary component. It is also of interest to see how self-consistent the fit is. The error bars on the plot represent plus/minus one standard deviation across the index retrieval for all pixels. The rms standard deviation, i.e. size of the error bars, is 0.671 in n and 0.744 in κ.

One of the major drivers of this error is scene drift creating an artificial polarization signature. This has an especially large effect at near-normal viewing angles, near the center of the beaker. Scene drift is a major problem for division of time polarimeters like the instrument used for this work. If the object or background is significantly changing temperatures between measurements for each polarizer angle, an artificial pseudo-polarization is added to the data. Because this work uses the modified Pickering method to calculate the Stokes vector, two S_0 measurements can be calculated: $L_0 + L_{90}$ and $L_{45} + L_{135}$. The difference between these calculated S_0
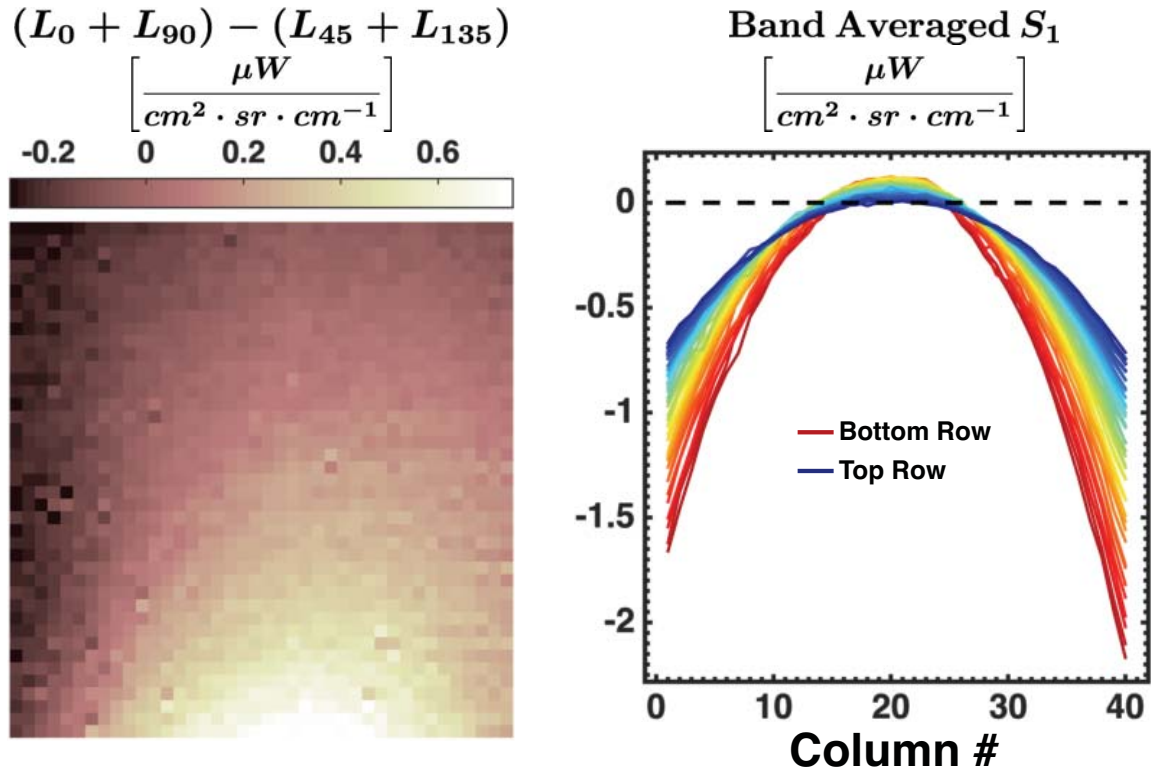
Figure 19. (left) Image of the band-averaged radiance difference between the two S_0 estimates for the Pyrex beaker dataset. (right) Band-averaged S_1 measurements across each row of the image. As shown earlier, S_1 should always be negative for an emission-dominated radiance signature. This positive biasing is greater towards the bottom of the beaker where scene drift is greatest indicating that scene drift is the source of this error.

value is an indication of scene drift. Figure 19 shows the band-averaged difference between these two S_0 estimates along with the band-averaged S_1 measurements across all rows. It was shown in Section 2.5 that, for an emission dominated signature, S_1 should always be negative but at near normal viewing angles it is positive. This effect is greater towards the bottom and center of the beaker, where scene drift is the greatest, indicating that temperature drift of the scene, most likely in the temperature of the beaker, over the course of the data collect is the source of this error. Using only the retrievals for the outer 10, and upper 20 pixels of the beaker, where scene drift is least and has the least effect, the rms error is reduced to 0.091 and 0.259 in n and κ, respectively. Additionally, the pixel-to-pixel standard deviation is reduced to 0.487 in the real component and 0.502 in the imaginary component.

Another factor that may be affecting this data at near-normal viewing angles is the bias created due to noise as P approaches zero which was discussed in Section 4.3. One way to mitigate this effect is to allow the sign of P to vary, based on the sign of S_1, in each spectral channel. Figure 20 shows the results of performing the retrieval on every pixel while allowing P to change sign. In this case, the RMS error in n and κ is reduced to 0.090 and 0.222, respectively. The pixel-to-pixel variance, while slightly lower, still remains high at 0.549 and 0.435 in the real and imaginary components.

The chief issue with allowing P to change sign is even a small amount of error or scene drift can cause P to switch signs as the true P approaches 0. As was shown in Section 4.3, the only way for P to be positive is if the downwelling temperature is greater than the object temperature. This causes a contrast reversal where the fit attempts to make the downwelling radiance match what is actually the emitted radiance and vice-versa. The index of refraction that produces a certain reflectivity spectrum is significantly different than that which produces the same spectrum in
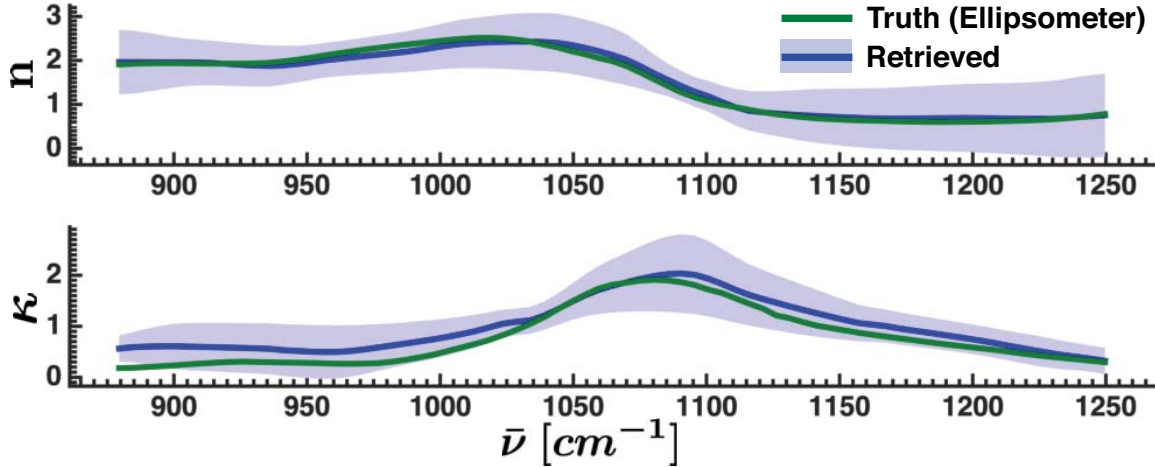
Figure 20. Retrieved (blue) and true (green) index of refraction for each pixel of the Pyrex beaker. The solid blue line represents the median retrieval across all pixels and the shaded blue region represents plus/minus one standard deviation. The green line is taken from ellipsometry measurements. In this fit, P is assigned the same sign as S_1 for each angle and spectral point.

emissivity. It was already shown that scene drift caused several pixels to have positive S_1 values. The index retrieval for these pixels is significantly different which is one of the main factors in the high pixel-to-pixel variability. When only the outer 10 and upper 20 pixels are considered as before, the error in n and κ is reduced to 0.085 and 0.179. The standard deviation is also significantly reduced even more significantly from 0.549 and 0.435 to 0.128 and 0.126.

Another way to analyze this dataset is to fit the index of refraction across every row of the image, using all surface normal angles in conjunction with one another in the fit. This is akin to a sensor flying over and viewing the same target from multiple angles. Figure 21 shows the results of this fit. The rms error in the real and imaginary components is 0.135 and 0.180, respectively, the fit-to-fit variability is 0.220 and 0.238. Interestingly, the RMS error in n is actually slightly greater than the pixel-by-pixel fit, but given the error bounds this difference is not statistically significant. As expected, the fit-to-fit variability is far less doing the row-by-row fit.

While there is significant variance between individual retrievals in all these cases,
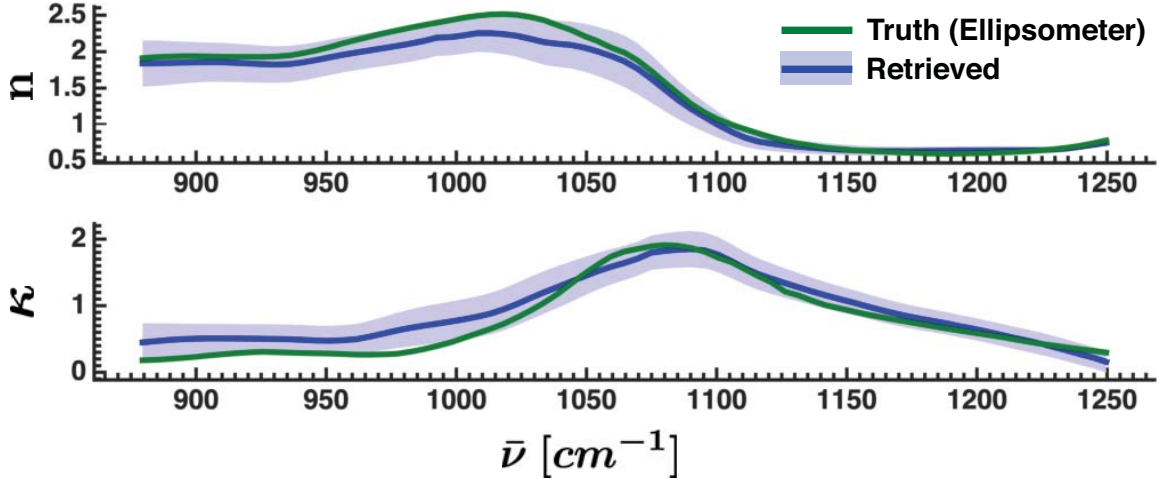
Figure 21. Retrieved (blue) and true (green) index of refraction for each row of the Pyrex beaker image. The solid blue line represents the median retrieval across all rows and the shaded blue region represents plus/minus one standard deviation. The green line is taken from ellipsometry measurements.

it is important to note that these are uncorrelated with temperature. It has been previously shown that the change in index of refraction with temperature for various glasses is very small (on the order of $10^{-4} \frac{1}{K}$) [134] so the retrieved index should not change significantly with temperature. The average coefficient of determination (r^2) between temperature and the fitted index, across all spectral bands, is 0.07 for $n(\bar{\nu})$ and 0.02 for $\kappa(\bar{\nu})$. This indicates that, as required, the retrieval method is robust to changes in object temperature, at least in this case.

Another issue with this experiment is that the downwelling is not controlled. It is assumed that the downwelling radiance is blackbody-like, but this may not be strictly true. This makes it difficult to verify what the "expected" S_0 and P actually should be. Additionally, when fitting each row simultaneously, it is assumed that each pixel in a given row is seeing the same downwelling radiance. Even if the downwelling radiance is truly blackbody-like, each pixel might be seeing a blackbody at a different temperature, depending on from where in the room the reflection is actually origi-

nating. Because of these effects, the next two experiments were conducted using a controlled illumination source, specifically a blackbody.

Silicon Carbide Wafer.

The beaker represented a signature dominated by emission with the reflected component being ambient background. It is also interesting to examine the case where reflected radiance is the dominant component of the signature. Having a controlled illumination source also makes it easier control the experiment discussed in the previous section. For this test, a blackbody set to 50°C was used to illuminate a Silicon Carbide (SiC) wafer. The index of refraction of SiC is well represented by the Lorentz oscillator model making it a good test case for dealing with crystalline materials. The wafer was observed from angles of 20, 40, and 60° off of the surface normal. For each viewing angle, the blackbody was moved so the specular reflection off the wafer landed on the sensor. Data was collected at 1 cm^{-1} spectral resolution and 8 datacubes were averaged.

Figure 22 shows the measured and expected S_0 and P for all three angles measured. The white boxes on the inlay images show the pixel window used in fitting. The error bars represent two times the standard deviation across all pixels. It is clear that there is significant difference between the expected and measured values for both S_0 and P. The error in S_0 appears to be a spectral shift which could be explained by a slight error in the expected oscillator location. The measured P is also significantly higher than expected near the peak at both 40° and 60°. One possible reason for this is birefringence which will be discussed in more detail later.

Even with these differences between measured and expected, index of refraction can still be accurately retrieved. Figure 23 shows the retrieved index compared with the expected. The shaded blue region represents plus/minus two standard deviations
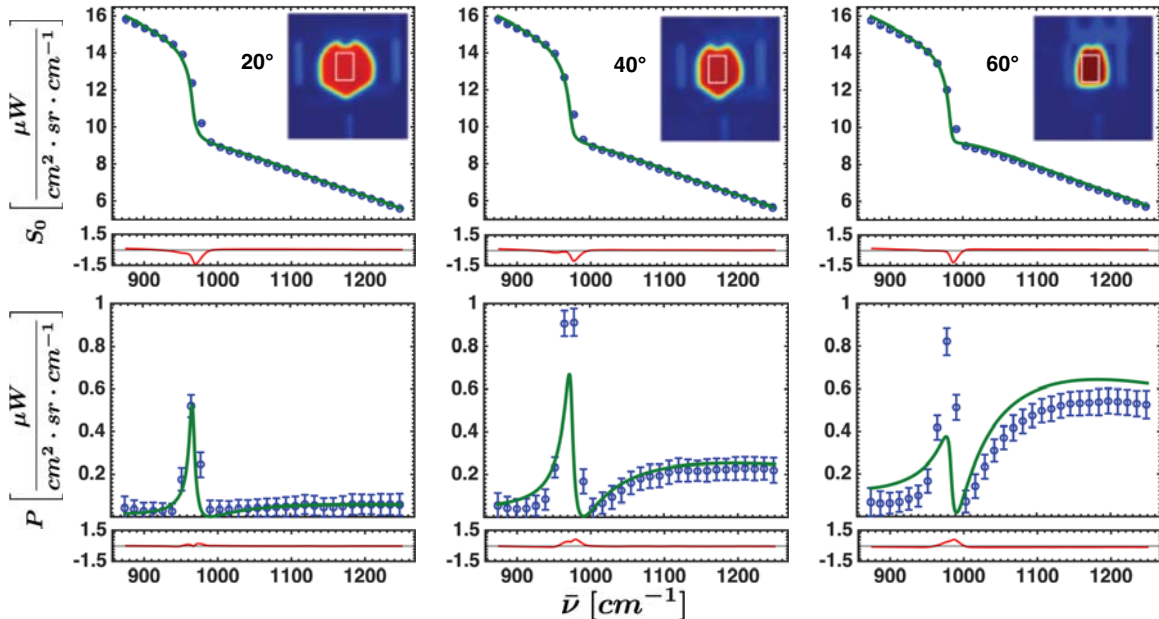
Figure 22. Measured S_0 and P spectra (blue) compared with expected (green) for all pixels of a SiC wafer. Expected values are generated based on forward modeling the index of refraction measured by an ellipsometer. The white boxes on the inlay images shows the pixel window used in fitting. The error bars represent two times the standard deviation across all pixels. The plots in red below each pane represent the residual error between measured and expected. Some potential causes for the errors between measured and expected, especially in P will be discussed.
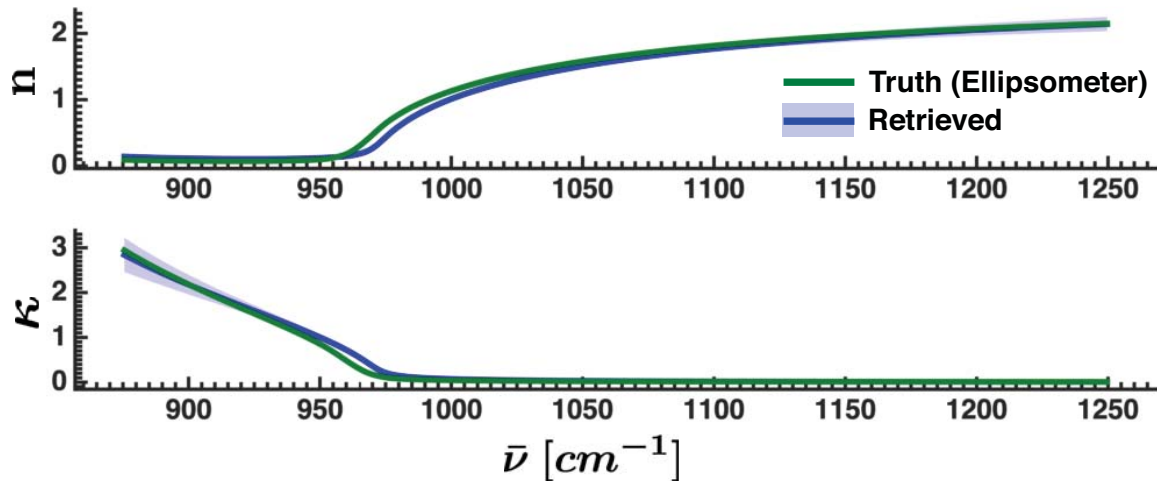

Figure 23. Retrieved (blue) and true (green) index of refraction for a SiC wafer. The solid blue line represents the median retrieval across all pixels and the shaded blue region represents plus/minus two standard deviations. The green line is taken from ellipsometry measurements.

90

across all pixels. The rms error between expected and retrieved is 0.073 in n and 0.067 in κ. The rms standard deviation across all retrievals is 0.027 in n and 0.046 in κ. The retrieved downwelling and object temperatures are 321.7 $\pm$ 0.3 K and 293.9 $\pm$ 0.1 K, respectively, compared with the expected 323.2 and 294.1 K.

Despite this reasonable fit to the index, however, the S_0 and P spectra are not well described by the retrieved values, as shown in Figure 24. This indicates that there is something wrong with the model being used to describe the SiC. Because this wafer was a highly pure crystalline sample of SiC, it was suspected the birefringent nature of SiC may play a role in this discrepency. Essentially, birefringence means that the index of refraction depends on the polarization of the light either being reflected off of or emitted from the surface. The two polarization states are referred to as the ordinary and extraordinary, or o- and e-, rays.

A potential way to account for this is to simply solve for two indices of refraction, one for the s- and one for the p-pol radiance. The ellipsometer used to measure the index of refraction also has built-in models describing both the ordinary and extraordinary ray indices of refraction for SiC. Figure 25 shows the retrieved indicies using the method of solving for separate indices of refraction describing the s- and p-pol radiances. Results are compared with the ellipsometer expected values. The rms error in the real and imaginary components are 0.043 and 0.067 for the ordinary ray and 0.066 and 0.114 for the extraordinary ray. The rms standard deviation (i.e. the pixel-to-pixel consistency) is 0.024 and 0.043 in the real and imaginary components of the o-ray and 0.064 and 0.062 for the e-ray. The retrieved downwelling temperature is 321.4 $\pm$ 1.2 K and the retrieved object temperature is 294.1 $\pm$ 0.2 K.

Figure 26 shows the retrieved S_0 and P compared with the measured when birefringence is acconted for. This produces a much better fit to the measured data, especially for P. Without accounting for birefringence, the rms difference between
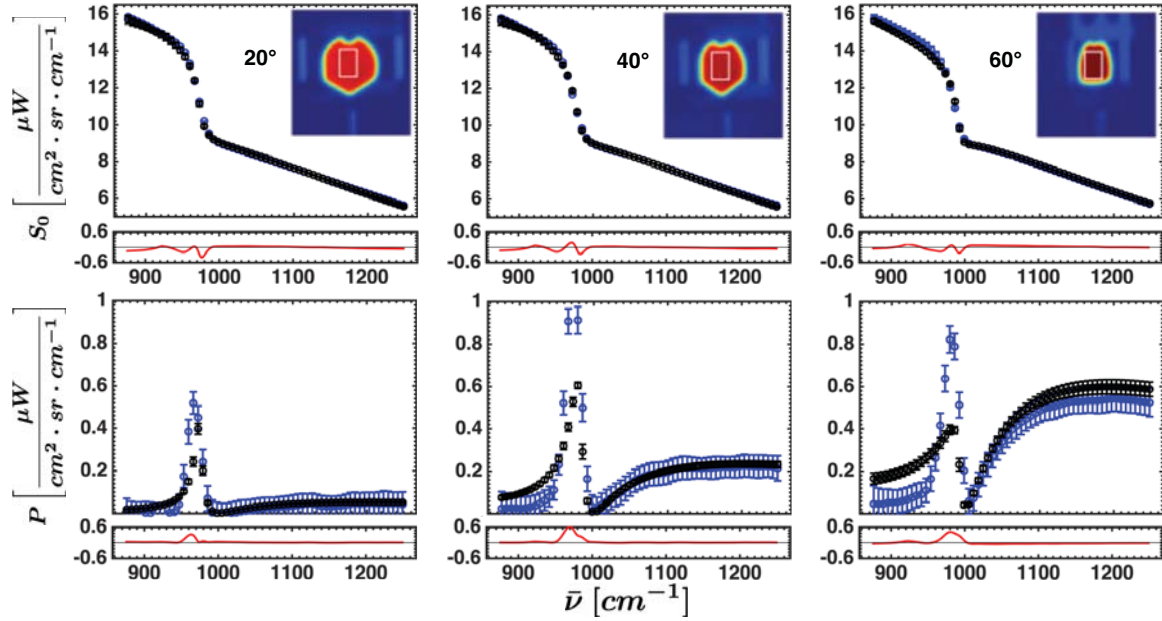
Figure 24. Retrieved S_0 and P spectra (black) compared with measured (blue) for all pixels of a SiC wafer. The retrieved values are generated by forward modeling the retrieved index of refraction, object temperature, and downwelling temperature. In both case, the error bars represent two times the standard deviation across all pixels. The plots in red below each pane represent the residual error between measured and retrieved. There are still significant differences between the retrieved and measured values, especially in P, which are discussed below.
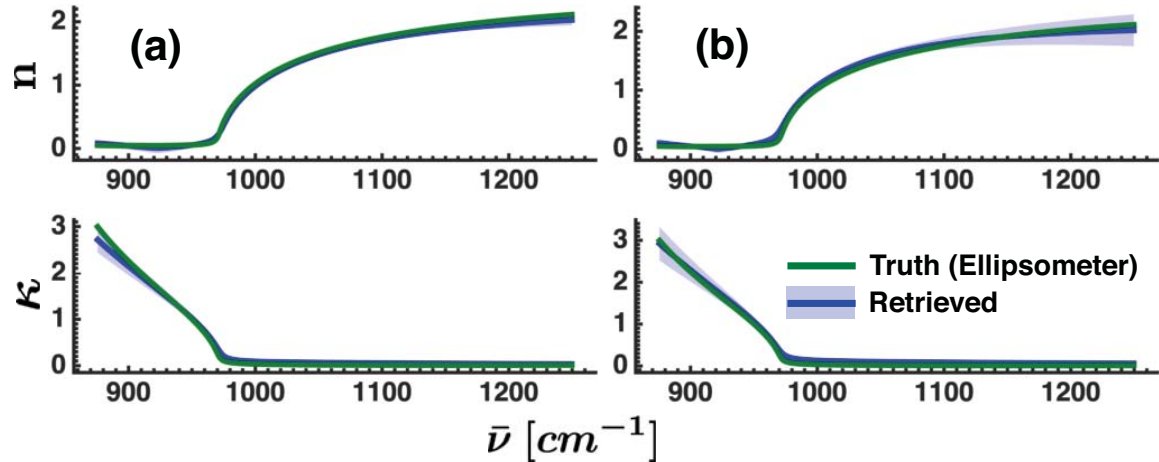
Figure 25. Retrieved (blue) and true (green) index of refraction for both the o- (plot a) and e-ray (plot b) of a SiC wafer. The solid blue line represents the median retrieval across all pixels and the shaded blue region represents plus/minus two standard deviations. The truth values were taken from existing models used in the JA Woollam IR-VASE ellipsometry software package for both the o- and e- ray indices of refraction for SiC.
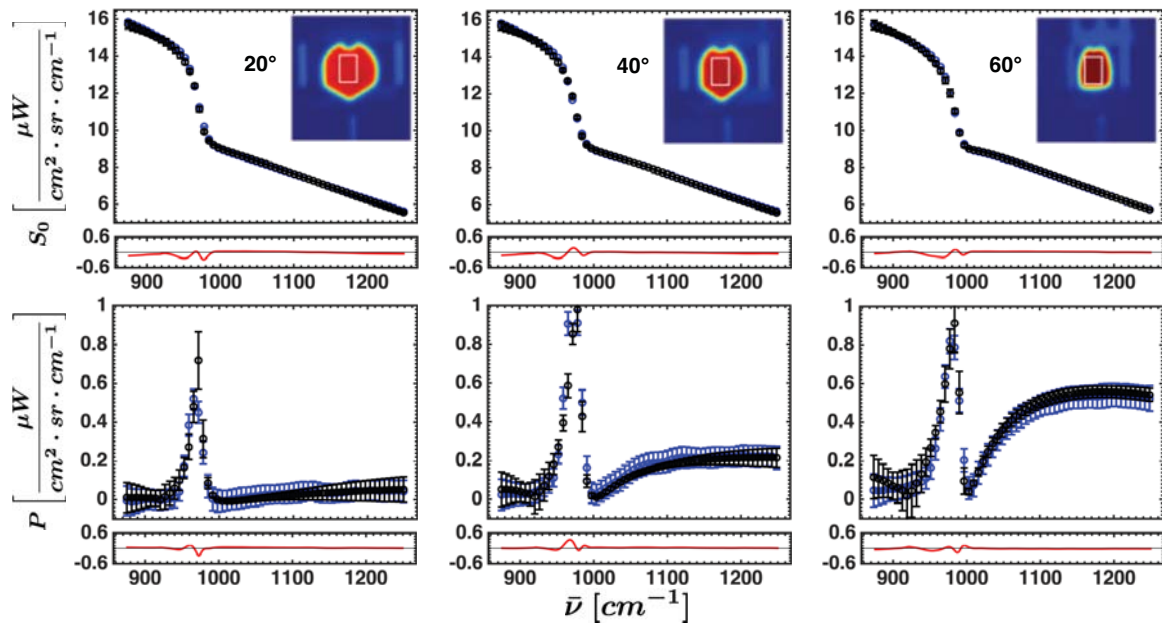
Figure 26. Retrieved S_0 and P spectra (black) compared with measured (blue) for all pixels of a SiC wafer when incorporating birefringence into the fit. The retrieved values are generated by forward modeling the retrieved index of refraction, object temperature, and downwelling temperature. In both case, the error bars represent two times the standard deviation across all pixels. The plots in red below each pane represent the residual error between measured and retrieved. The difference between the measured and retrieved spectra is significantly reduced, especially in P, compared to the fitted model when not accounting for birefringence.

measured and retrieved S_0 and P was 0.072 and 0.098 $\frac{\mu W}{cm^2 \cdot sr \cdot cm^{-1}}$, respectively. When birefringence is added to the fit, the error between measured and retrieved is reduced to 0.048 and 0.069 $\frac{\mu W}{cm^2 \cdot sr \cdot cm^{-1}}$ in S_0 and P, respectively.

Quartz Window.

For this test, a blackbody set to 115°C was reflected off of quartz glass block window. The temperature of the window was assumed to be the ambient temperature of the room, 21.5°C. The block was rotated to three different angles (nominally 20°, 40°, and 60°) and the blackbody was aligned so the sensor would always be in the direction of specular reflection. 16 cubes were averaged at 1 cm^{-1} spectral resolution. This represents a scenario similar to the SiC wafer dataset, the key difference being that quartz glass is an amorphous material and is not modeled well by the Lorentz oscillator model. A small sample of the material was used and ellipsometry measurements were taken to determine the true index of refraction.

Figure 27 shows the measured and expected S_0 and P. Again, the expected values are calculated based on forward modeling the ellipsometer-measured index of refraction along with the known blackbody and object temperatures. There are some differences between the measured and expected, but in general there is good agreement. One potential error in the 60° P data is uncertainty in the true viewing angle. The quartz block was aligned using a protractor and ruler which gives some relatively large uncertainties. Results from Section 5.2 indicate that the true surface normal angle may have been slightly less than 60° which could be why the expected overestimates the amount of polarization.

From this data, the index retrieval is again performed independently on each pixel. For the sake of simplicity, only pixels that viewed the window at all three angles are used (see the inlay images in Figure 27). The results of the retrieval are shown in
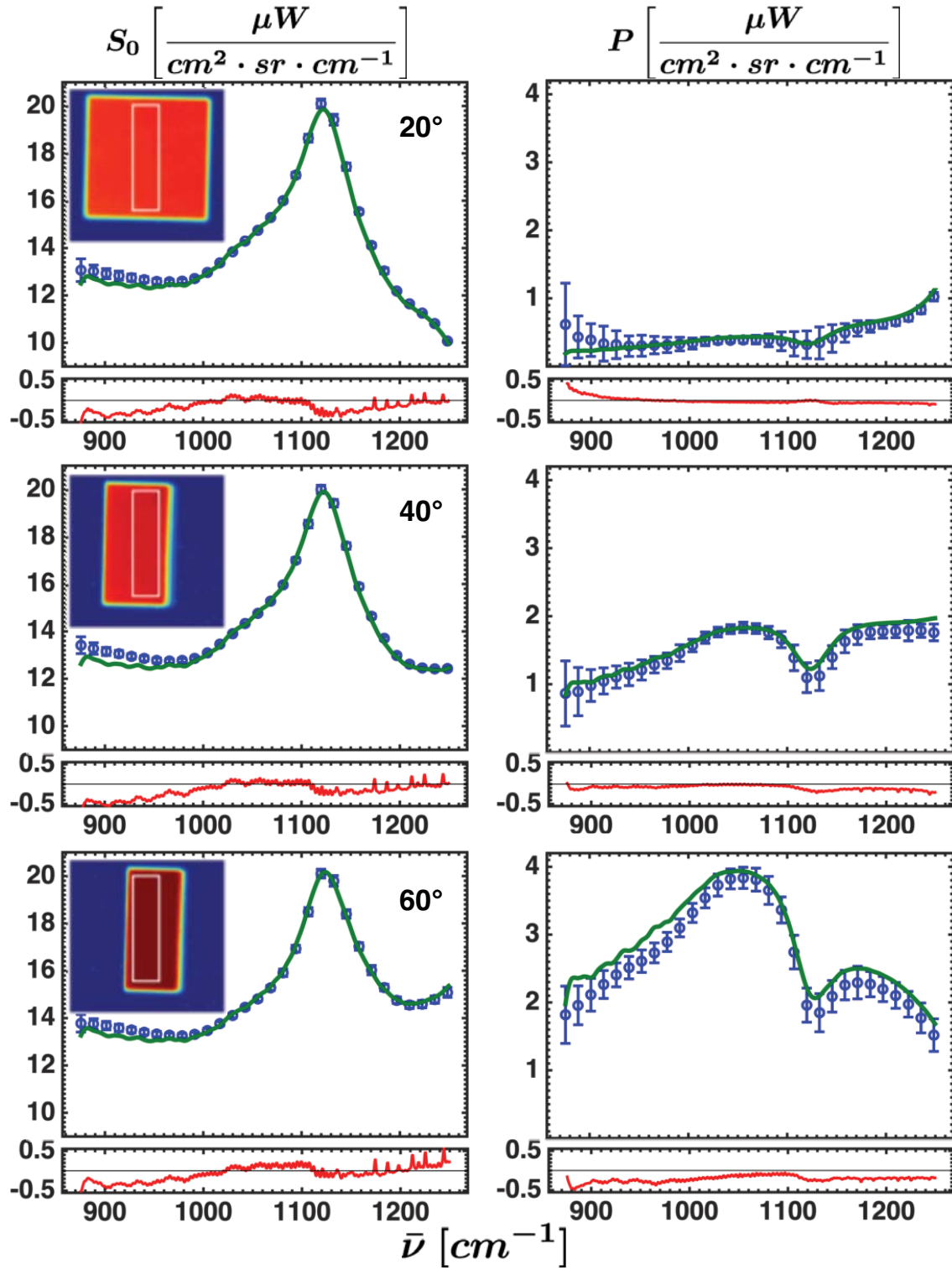
Figure 27. Measured S_0 and P (blue) compared with expected (green) for a quartz glass block window with heated blackbody radiance reflecting off of it. The error bars represent plus/minus one standard deviation across all pixels. The white box on the inlay images show the pixels used in the fitting for each viewing angle. The plots in red below each spectra represents the error between measured and expected.

95
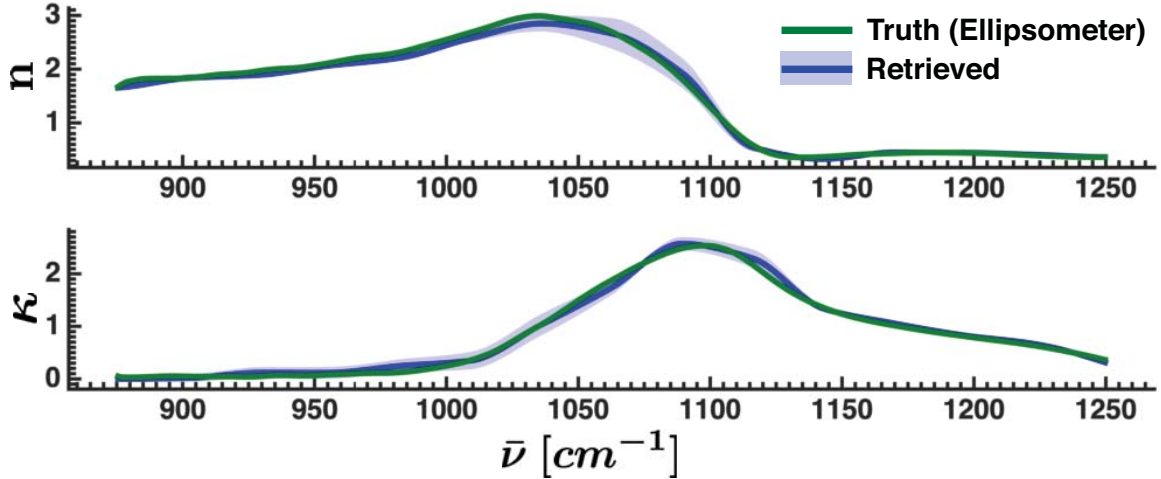
Figure 28. Retrieved (blue) and true (green) index of refraction for a quartz glass window. The solid blue line represents the median retrieval across all pixels and the shaded blue region represents plus/minus two standard deviations. The green line is taken from ellipsometry measurements.

Figure 28. The rms error between the retrieved and expected index is 0.072 for the real component and 0.062 for the imaginary component. The rms standard deviation across all retrievals, i.e. the size of the retrieval errorbars, are 0.060 for the real component and 0.057 for the imaginary component. The retrieved downwelling and object temperature were 386.4 ± 1.4 and 298.1 ± 1.2 K, respectively, compared with the expected 388.2 and 294.7 K. The error bounds represent two standard deviations across all pixels.

Figure 29 shows how these retrieved parameters forward modeled to S_0 and P compare with the measured values. The rms error between the median retrieved S_0 and median measured S_0 is 0.133 $\frac{\mu W}{cm^2 \cdot sr \cdot cm^{-1}}$ or approximately 1% of the average S_0 value. The rms error in P is 0.079 $\frac{\mu W}{cm^2 \cdot sr \cdot cm^{-1}}$ which is approximately 5% of the average P value. In almost all cases, the retrieved values lie well within the error bars of the measurements indicating that the measurements are well described by the model. For comparison, when the Lorentz oscillator model is used to describe this

data, the error in n and κ increases to 0.366 and 0.367. The error difference between the retrieved S_0 and P and measured are 0.507 and 0.165 $\frac{\mu W}{cm^2 \cdot sr \cdot cm^{-1}}$, respectively.

One of the common material identification techniques in the LWIR is temperature-emissivity separation; see Section 3.5 for more information. One popular TES algorithm is the method of maximum smoothness described in Section 3.5. It is interesting to see how the index of refraction retrieval method here compares to TES algorithms. To do the comparison, the retrieved index of refraction is forward modeled to emissivity. The TES algorithm is applied to the same data. There are still a couple key differences between these two methods though. First, all angles are used in conjunction with one another when fitting the index of refraction. The ability to effectively average multiple angles is one of the chief advantages of estimating index of refraction. Because emissivity is changing with viewing angle, concatenating multiple viewing angles is not advisable for TES algorithms. The other main difference is that the index of refraction retrieval is also solving for the downwelling radiance while the TES algorithm requires *a priori* knowledge of the downwelling radiance as an input. For this comparison, the true blackbody temperature and emissivity are used as inputs for the TES algorithm.

The results of the comparison are summarized in Figure 30. To make this a fair comparison, the average of two pixels is used for the TES algorithm. Because TES does not utilize polarization, the data TES would be performed on would not be polarimetric. The linear polarizer cuts out approximately half of the light reaching the sensor so a non-polarimetric sensor would have approximately twice as much signal. This is the effect that is mimicked by performing the TES on a two-pixel average. The rms error across all spectral points in the TES retrieved emissivity at 20°, 40°, and 60° viewing angles is 0.0429, 0.0357, and 0.0452, respectively. Using the method presented here, the error is reduced to 0.0132, 0.0127, and 0.0153. The pixel-to-pixel
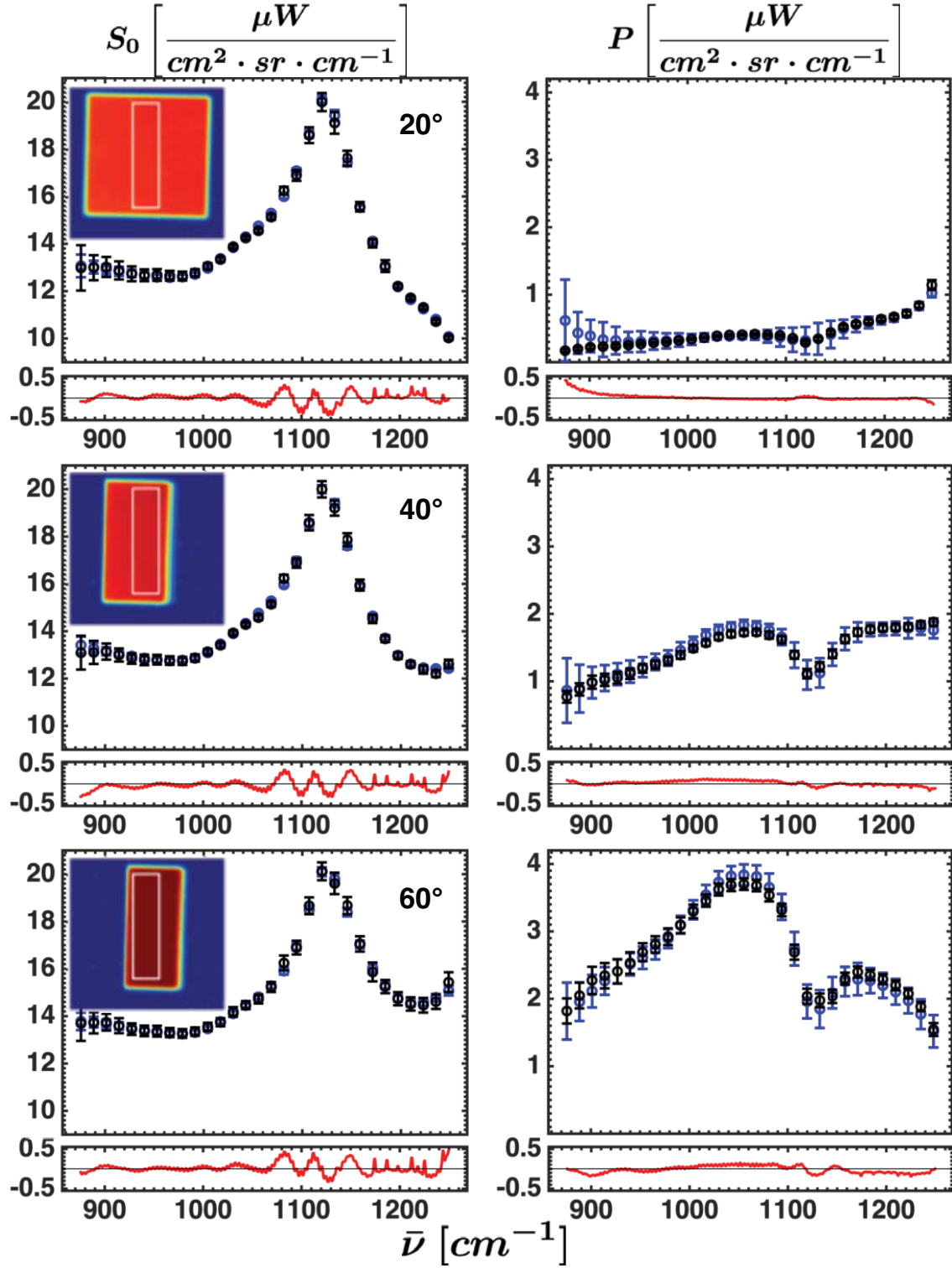
Figure 29. Measured S_0 and P (blue) compared with retrieved (black) for a quartz glass block window with heated blackbody radiance reflecting off of it. The blue (measured) error bars represent plus/minus one standard deviation across all pixels. The black (retrieved) error bars represent plus/minus two standard deviations. The white box on the inlay images show the pixels used in the fitting for each viewing angle. The plots in red below each pane represents the error between measured and retrieved.

98
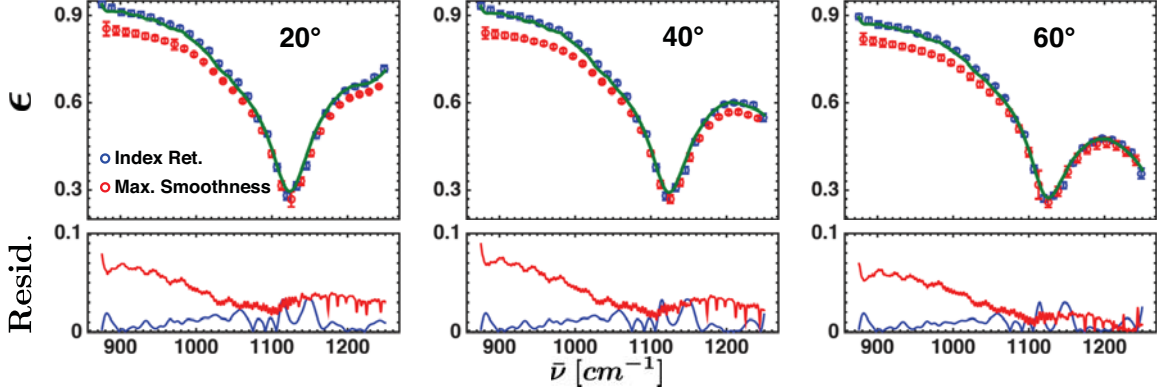
Figure 30. Comparison of the emissivity retrieved via maximum smoothness TES (red) and the method developed in this work (blue) at all three viewing angles. The true emissivity generated by forward modeling the ellipsometry measured index of refraction is in green.

variability is also reduced albeit less so. The rms standard deviation, i.e. the size of the error bars, for the three angles are $4.89 \cdot 10^{-3}$, $4.71 \cdot 10^{-3}$, and $4.50 \cdot 10^{-3}$ compared to $5.88 \cdot 10^{-3}$, $4.74 \cdot 10^{-3}$, and $7.82 \cdot 10^{-3}$ when using TES.

The main source of error in the TES algorithm is converging to the wrong temperature. One of the basic tenets of the maximum smoothness TES algorithm is that the downwelling is not spectrally smooth relative to the emissive spectrum. Under clear sky, this is almost always true, but in this case, the downwelling was a blackbody and therefore does not have a lot of spectral variability. With that said, the spectral angle between the retrieved and library emissivity spectra is often what is used in classification. This is a metric of how similar the spectra are disregarding their overall absolute value. The spectral angle between the TES retrieved emissivity spectra and truth at 20°, 40°, and 60° are 0.77°, 0.88°, and 1.14°, respectively. In this aspect, the TES algorithm outperforms the index retrieval at low angles. The spectral angles between the emissivities solved for via the index of refraction retrieval at all three angles are 1.00°, 0.98°, and 0.92°. The biggest issue with TES is that the emissivity is viewing angle dependent. The spectral angle between the retrieved emissivity at 20°, 40°, and 60° and the true emissivity at normal viewing is 0.7°, 2.6°, and 6.7°,

respectively. By comparison, the spectral angle between the retrieved and the true index is 1.5° and 3.0° in the real and imaginary components and remains constant regardless of viewing angle.

Surface Normal Estimation.

The results presented to this point have all assumed the viewing geometry was known, but this fitting algorithm can also be adapted to simultaneously solve for index of refraction and surface normal angle relative to the sensor. To this point, it has been assumed that the viewing geometry was known *a priori* but this is not, in principle, a necessary assumption. Adding a third dimension of spatial information, namely the angle of a target's surface normal relative to the image plane, has the potential to aid in target classification.

First, the Pyrex beaker data was again analyzed this time treating the viewing angle as an additional fit parameter. This provides an interesting test case because there is range of different angles going horizontally across the image, which vary in a way that is easy to model using simple geometry. There are also multiple rows which should have roughly identical solutions so the self-consistency of the angle retrievals can be compared. For each pixel in the image, surface temperature, downwelling temperature, viewing angle, and index of refraction were solved for. The constraints of the fit are described in Chapter IV, the only additional constraint was forcing the viewing angle parameter to be between 0° and 90°. The initial guess of viewing angle is always 45°. The fitted angle results are shown in Figure 31 and compared with the true values.

The top two images, (a) and (b), show the true and retrieved angle maps, respectively. The plot below these images shows the median retrieved angle across all rows (blue line) plus/minus two standard deviations (shaded blue region) compared with
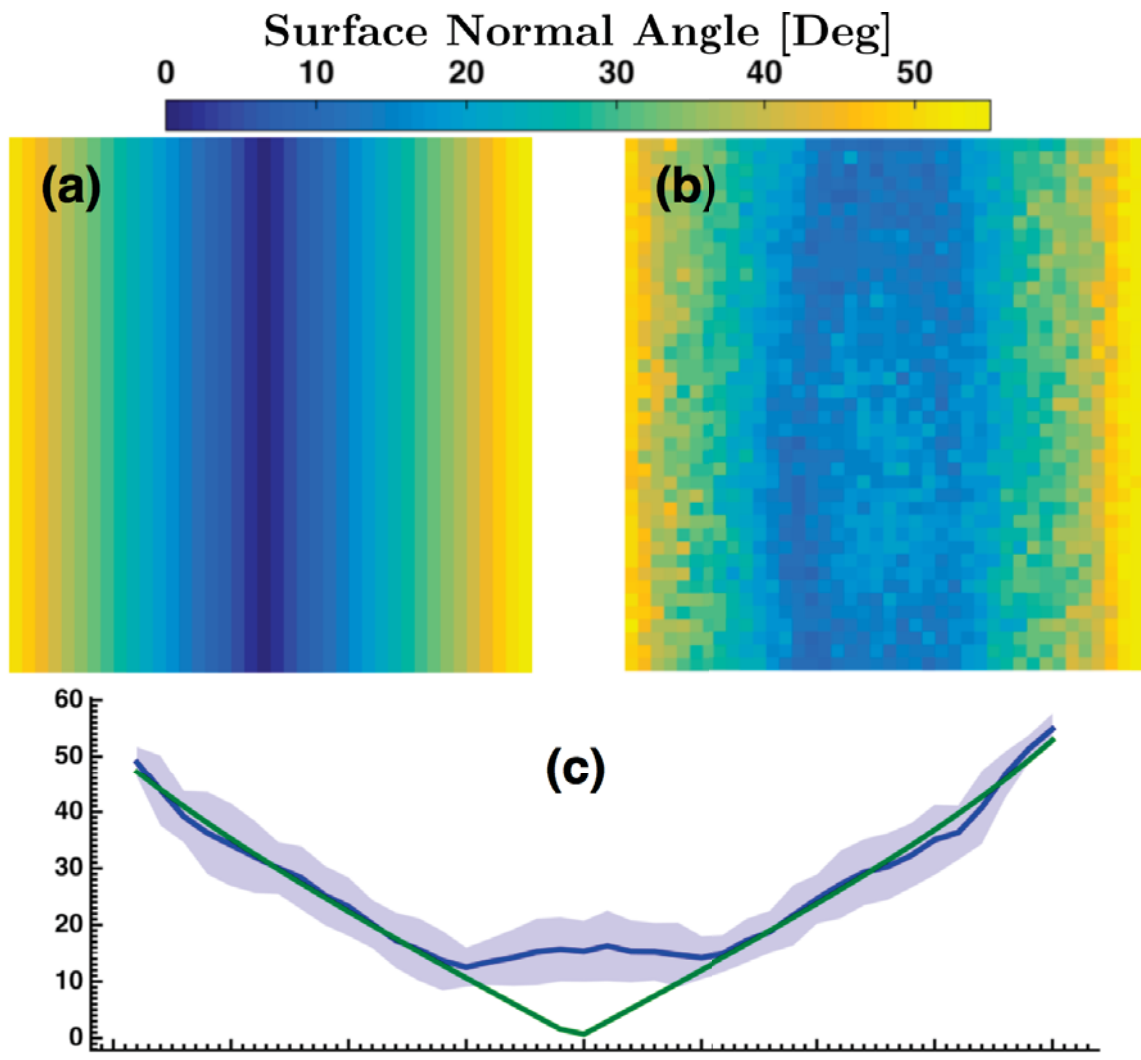
Figure 31. Retrieved and true surface normal values for all pixels imaging a Pyrex beaker. (a) shows the true angle map and (b) shows the retrieved angle map. (c) shows the median across all rows of the image. The blue line is the retrieved angle and the shaded blue region represents plus/minus two standard deviations across all rows. The green line is the true angle.

the true angle values (green). The rms error between the median retrieved angle and the truth across all columns in the image is 5.3°. It is obvious that much of this error is due to the behavior of the retrieval as angle goes to zero. The angle retrieval never goes below about 15°, even when the true angle is near zero. One cause of this is the effect discussed in Section 4.3. Because S_1 and S_2 are added in quadrature, when polarization is near zero, noise will produce an additive bias to the total polarization measurement. At 15°, the band-average P is between 0.03 and 0.07 $\frac{\mu W}{cm^2 \cdot sr \cdot cm^{-1}}$, which is consistent with P values where it was shown in Section 4.3 that this biasing starts to affect the data. Because polarization increases with angle, this bias is interpreted in the angle fit as a larger surface normal angle than what is actually there. Another potential culprit for this error is scene drift, shown in Section 5.2, generating an artificial polarization signature.

One might think to ignore the polarization if it is near or below this threshold, as discussed in Section 4.3, but unfortunately S_0 changes very slowly with angle at near-normal viewing geometries. This means that S_0 is not effective in estimating small angles either. Using a sensor with better noise characteristics will drive this minimum retrievable angle down, but there will always be some point where the angle is too close to normal to be accurately retrieved. Still, this technique is useful in giving shape information at larger angles and potentially with additional processing or better instrumentation could give information about small angles as well.

When pixels with a true surface normal angle of less than 15° (the center 12 columns) are ignored, the rms error of the median retrieved angle is 1.4°. The rms standard deviation across all rows of the image is 2.6°.

It is also important to consider what effect fitting the angle might have on the retrieved index of refraction. This provides a measure of how variations in retrieved viewing angle from truth affect the index retrieval. If this effect is too large then it is

not practical to simultaneously estimate index and surface normal, even if the surface normal estimates are somewhat accurate. Figure 32 shows the retrieved index when fitting angle (a) compared to assuming angle is known (b). Due to the errors as P goes to zero near the center of beaker, the 12 center columns are excluded. The rms errors in n and κ increase from 0.115 and 0.466 to 0.150 and 0.476, respectively when surface normal angle is included as a fit parameter. The rms standard deviation, i.e. half the size of the error bars, increases from 0.163 and 0.162 in n and κ when assuming angle is known to 0.251 and 0.354 when fitting surface normal angle. Because the scene geometry is known very well in advance, it is unsurprising that allowing variations from the expected angle increases error. It is promising, however, that the index retrieval does not get significantly worse when simultaneously fitting the angle.

Another way to compensate for the error at near-normal viewing angles is to allow the sign of P to vary at every spectral point. As discussed earlier this has some drawbacks which will be seen and discussed later in this section. Figure 33(a) shows the retrieved angles when the sign of P is allowed to vary. While this is able to match angles less than 15°, it still is unable to retrieve angles less than about 10°. The major contributor to this limitation seems to be scene drift. Figure 33(b) shows the
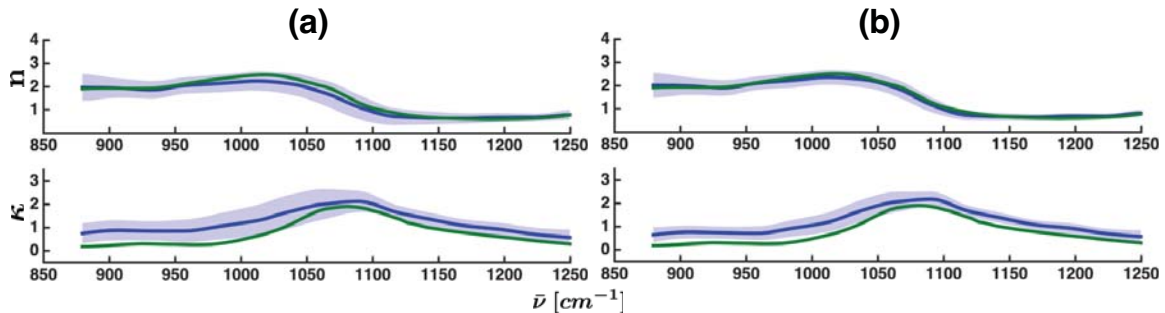
Figure 32. Retrieved index incorporating surface normal angle as a fit parameter (a) compared to index retrieval assuming the angle is known *a priori* (b). The blue line represents the median retrieval across pixels and the shaded blue region represents plus/minus two standard deviations across pixels. Because of the errors as total polarization, P, goes to zero near the center of beaker, the 12 center columns are excluded from this plot.

results of the pixel-by-pixel angle retrieval using only the top 7 rows of the image, where scene drift was previously shown to be lowest. There still appears to be some error for angles less than about 5° which may be due to some small scene drift. In total, the rms error in angle is reduced to 2.8° when only using the top 7 rows as compared to 4.0° using all rows. Both of these are better than the rms error of 5.3° when the sign of P is not allowed to vary spectrally. There is still the issue of the contrast reversal between reflected and emitted radiance when scene drift causes the P to have the wrong sign, however.

This fitting can also be done using all surface normal angles in conjunction with one another which imposes the additional constraint that each pixel along a row of the image must be the same material. Just as in Section 5.2, the fit was then done independently on each row of the image, but this time the viewing angles of each pixel in the row (40 in total) are treated as fit parameters. Figure 34 shows the results of this fit. Again the effect of S_1 drifting positive are evident. The majority of the pixels in a given row have negative P dictating that the object temperature is greater than the downwelling temperature for that row. When P for a given pixel is positive, the closest the fit can get to replicating this is to set the surface normal angle, and thus the modeled P, to zero. Figure 34 (b) shows the surface normal retrievals for only the top 7 rows of the image where scene drift is lowest. While the effect of P going positive is still evident, it is less pronounced, only occuring at angles less than about 5°.

The rms error in surface normal is 3.85°, which is clearly driven the error at small surface normal angles and scene drift. For the 7 rows at the top of the image, where temperature drift is the smallest, the rms error is 2.28°. The rms error for only the outer 10 pixels where the surface normal is the greatest is only 1.08°. The rms error in the retrieved index performing the fit this way is 0.228 in the real component and
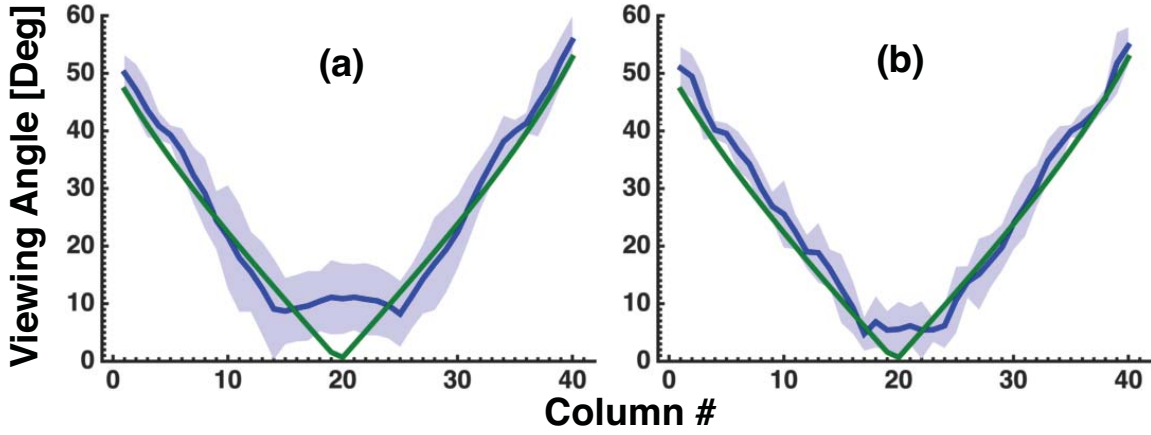
Figure 33. Retrieved (blue) and expected (green) surface normal angles ascribing a sign to P at each spectral point. The shaded blue region represents plus/minus two standard deviations across rows. (a) shows the results of using all rows of the image while (b) shows the results of only using the top **7** rows of the beaker. This shows that the error in (a) at small angles is most likely driven by scene drift which is worse at the bottom of the beaker than at the top.
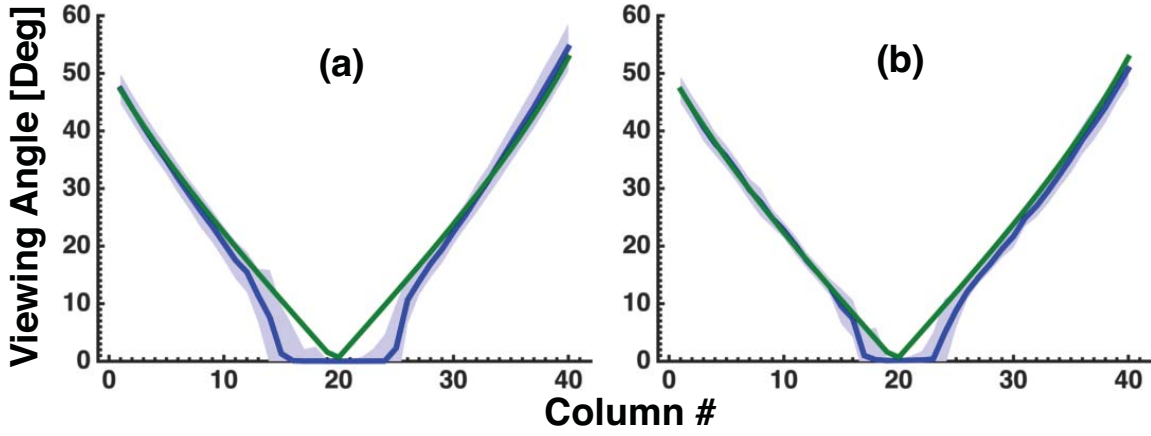
Figure 34. Retrieved (blue) and expected (green) surface normal angles when fitting the index for every row, concatenating all viewing angles into one fit. The shaded blue region represents plus/minus two standard deviations across rows. (a) shows the results of using all rows of the image while (b) shows the results of only using the top **7** rows of the beaker. The error in the retrieved angle as the true angle approaches zero is again an effect of scene drift.

0.223 in κ. The rms standard deviation across all rows is 0.183 and 0.144. When only the top 7 rows are used, the error is reduced to 0.106 and 0.150, and the standard deviation is reduced to 0.095 and 0.083. As expected, this is better than the pixel-by-pixel fits demonstrating the utility of using multiple viewing angles to constrain the fit.

As was shown in Section 5.2 and previously in this section, scene drift and other factors made this dataset somewhat difficult to work with. To further test simultaneously estimating surface normal angle and index of refraction, the quartz block data was also examined. The quartz block presents a different test case for the angle retrieval code. Here each pixel is seeing roughly the same angle, with only a slight change going left to right across the image due to the pixel FOV. This provides a better test of the self-consistency of the retrieval. For this, the multiple viewing angles of nominally 20°, 40°, and 60° are again used in conjunction with one another to constrain the fit. Unlike with the beaker dataset, however, the true surface normal angles cannot be estimated from the image itself and are therefore more uncertain. The alignment of the block was done with a protractor so estimated uncertainty in the "true" angle is approximately 3°. Each of the three angles is an independent parameter in the fit. Again, the fit is performed independently for each pixel that viewed the object at all three angles.

The retrieved angles are 20.58 ± 1.92°, 41.34 ± 3.24°, and 58.00 ± 3.84°. Each of these angles are consistent with the expected values. Additionally the uncertainties, reported as two standard deviations, are highly skewed by outliers. For normally distributed values, 95% of pixels should lie with two standard deviations of the median. For this dataset the actual 95% confidence bounds are 20.58 ± 0.80°, 41.34 ± 1.17°, and 58.00 ± 1.30°.

On top of all of this, there is some inherent variability in these measurements

because each pixel has a slightly different viewing angle relative to the surface normal. There is approximately a 0.5° difference between the expected surface normal at the left edge of the window compared to the right edge. 53.7%, 53.3%, and 51.1% of pixels lie within $\pm$ 0.25° of the median for the three angles, respectively.

The retrieved index of refraction, shown in Figure 35 is also very accurate even when simultaneously solving for viewing angle. The rms error is the real and imaginary components is 0.081 and 0.071. Recall the error when holding the angle fixed was 0.072 and 0.062 so again this is slightly worse, but not significantly so. The main difference between fitting the angle and holding it fixed is the pixel-to-pixel variability. The rms standard deviation across all pixels is 0.135 in both n and κ when fitting angle compared to 0.060 and 0.057 when holding angle fixed. Again, however, outliers heavily skew this standard deviation when fitting angle. When pixels where the retrieved angles were outside of the 95% confidence bounds are ignored, the pixel-to-pixel variability is reduced to 0.036 and 0.035 in the real and imaginary components. The retrieved downwelling and object temperatures when these outlier pixels are ignored is 385.2 $\pm$ 1.2 K and 298.8 $\pm$ 0.5 K.

Similar results are seen when analyzing the SiC dataset as well. The median retrieved angles across are pixels are 23.1 $\pm$ 1.6°, 37.1 $\pm$ 1.0°, and 55.3 $\pm$ 1.4°. The reported uncertainty represents two standard deviations across all pixels. This is another case where the true angles are not well known, but the retrievals are at least close to the expected. The index of refraction retrieval also remains accurate, the rms error in n and κ is 0.084 and 0.069, respectively which is very close to the error of 0.073 and 0.067 when angle is held fixed.
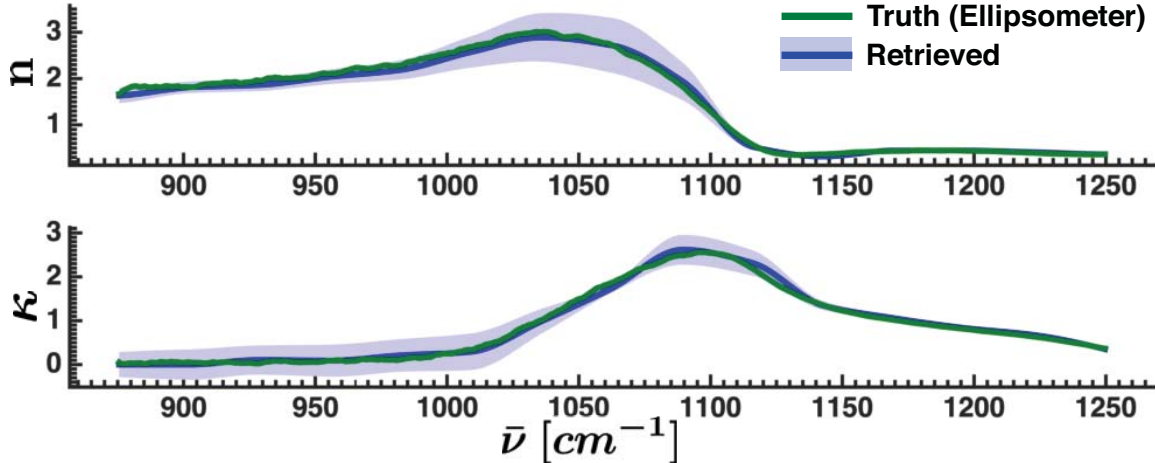
Figure 35. Retrieved (blue) and true (green) index of refraction for a quartz glass window when simultaneously fitting viewing angle. The solid blue line represents the median retrieval across all pixels and the shaded blue region represents plus/minus two standard deviations. The green line is taken from ellipsometry measurements.

Other Considerations.

Single Angle vs Multiple Angles.

With the exception of some of the simulated datasets and some of the beaker data analysis, all the work presented thus far has used multiple angles to constrain the fit. It is also of value to see how the fit performs without multiple viewing angles providing constraints, specifically on the quartz and SiC datasets. For the sake of a more accurate comparison, three pixels are averaged for each single angle fit to ensure than any improvement in the multiple angle fits are not just due to the boost in SNR from having three measurements. Instead of 20°, 40°, and 60°, the angles used are the median retrieved angles from the previous section. Figure 36 shows the results of individually fitting each of the viewing angles for the quartz window data.

The error in the 40° fit illustrates one of the fundamental issues with utilizing index of refraction measurements. There are many local minima where drastically different indices of refraction can produce very similar reflectivity and emissivity spectra and thus produce very similar radiance signatures. With noise, or potentially systematic
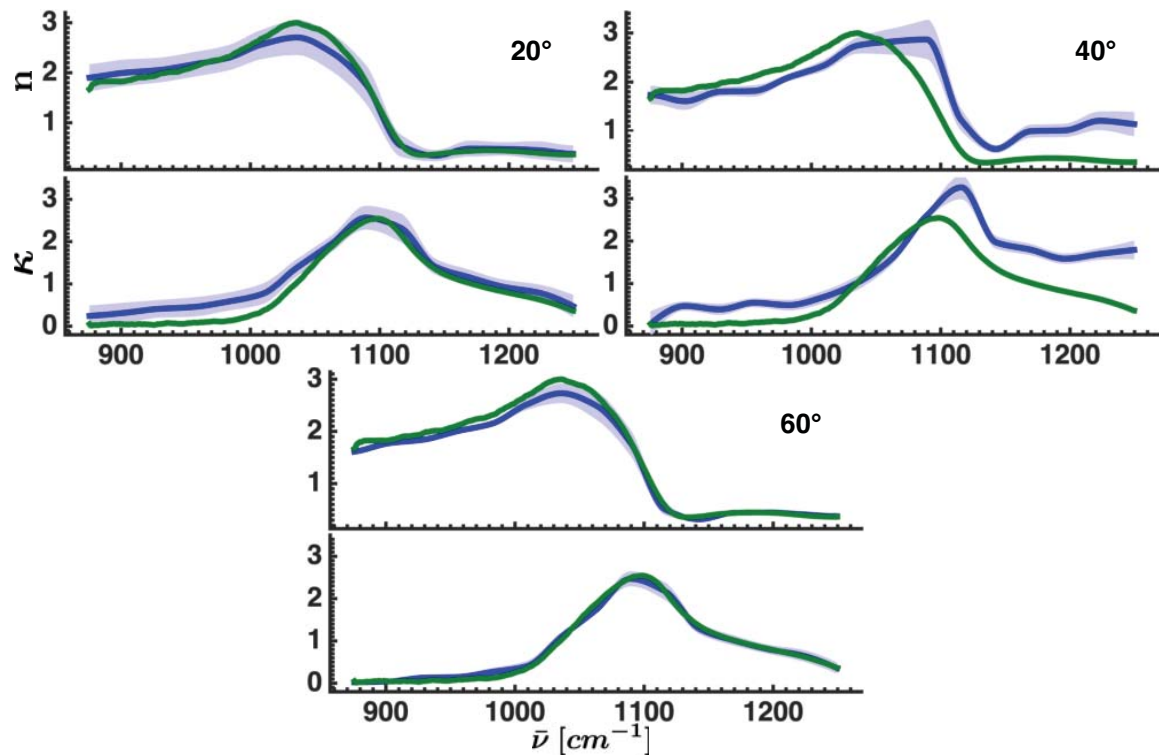
Figure 36. Retrieved (blue) and true (green) index of refraction for a quartz glass window using only a single viewing angle. The solid blue line represents the median retrieval across all pixels and the shaded blue region represents plus/minus two standard deviations. The green line is taken from ellipsometry measurements.

biasing, these local minima can become the global minimum. In this case, radiance spectra is better modeled by these retrieved values than the truth with an rms error in S_0 and P of 2.45 and 1.71 $\frac{\mu W}{cm^2 \cdot sr \cdot cm^{-1}}$ compared to 4.42 and 2.15 $\frac{\mu W}{cm^2 \cdot sr \cdot cm^{-1}}$ when using the expected values based on the ellipsometer measured index of refraction. The median retrieved temperatures for the 40° fit were $T_d = 389.1$ K and $T_e = 297.9$ K which are very close to the temperatures of 386.4 K and 298.1 K retrieved using all three angles. This indicates that the reflectively and emissivity spectra obtained by forward modeling this index is close that that of forward modeling the true index, which is born out in the data. The rms difference between the retrieved reflectance and the truth is only 1.7%, whereas the rms difference between the real and imaginary components of retrieved index and truth are 0.5 and 0.6. These errors values in index represent 36.6% and 72.2% of the mean n and κ, respectively. This further illustrates that drastically different indices of refraction can produce similar spectra potentially allowing systematic errors in the measured radiance to dramatically skew the retrieved index of refraction.

The fits at 20° and 60°, however, show much better results. The rms error in n and κ is 0.133 and 0.265 for the 20° case and 0.130 and 0.075 for the 60° case. This mimics what was seen in the simulated data where large viewing angles, because they tend to have more polarization, are better suited for fitting index of refraction. It should be noted that both of these fits still perform worse than using all three angles in conjunction with one another where the rms error was 0.072 and 0.062 in the real and imaginary components, respectively. Recall that the single angle fitting is utilizing a three pixel average, so this indicates that using multiple viewing angles is actually adding independent information to the fit as opposed to simply reducing the SNR. There is more pixel-to-pixel variability when only using a single angle in the 20° fit, but the 60° fit seems to perform on-par with the three angle fit in this

measure. The rms standard deviation across all pixels was 0.129 in n and 0.114 in κ for the 20° fit. For the 60° fit, the rms standard deviation was 0.061 and 0.060. For the fit using three angles, the rms standard deviation was 0.060 and 0.057 in the real and imaginary components , respectively. Again, this illustrates that the fit performs better from farther off-nadir viewing geometries.

Again, these fits can be compared with the maximum smoothness TES algorithm. While a single viewing angle makes the fit more susceptible to converging to the wrong solution in index of refraction, it also means that the S_0 and P spectra for a given angle can be better replicated since the fit is only trying to optimize that one angle. Again, twice as many pixels are averaged for the TES algorithm input to mimic the effects of a non-polarimetic sensor. In this case, since three pixels were averaged for the index fit, six pixels are averaged for the TES algorithm. The results for each of the three angles are shown in Figure 37.

The rms difference between the TES-estimated emissivity and truth is 0.0427, 0.0437, and 0.0352 for the three angles. The index retrieval again significantly reduces this error to 0.0213, 0.0174, and 0.0153. Again, it is seen that despite the large error in index of refraction at 40°, the emissivity is still retrieved quite accurately. As before, the rms error in the TES-estimated emissivity is primarily due to the algorithm fitting to the wrong temperature. The spectral angle between the retrieved and true emissivities for all three angles when fitting index is 1.23°, 0.98°, and 0.88° compared to 0.95°, 0.95°, and 1.00° when using maximum smoothness TES. As in the multi-angle case, the index retrieval seems to perform better relative to TES the further off-nadir the sensor is.

Unlike the multiple angle fit, the pixel-to-pixel variability seems to be less when using TES compared to using the index retrieval from a single angle. The rms standard deviation across all pixels (i.e. half the size of the errorbars in Figure 37) is
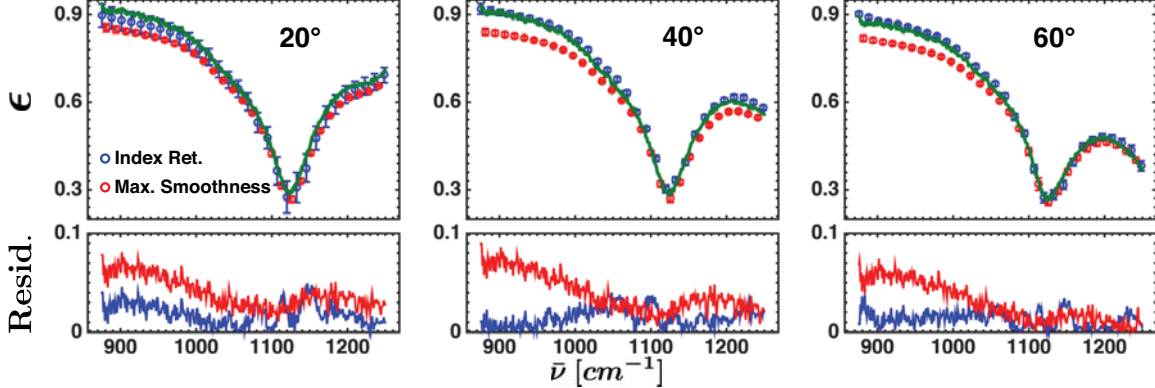
Figure 37. Comparison of the emissivity retrieved via maximum smoothness TES (red) and from forward modeling the retrieved index of refraction using only a single viewing angle (blue). The true emissivity generated by forward modeling the ellipsometry measured index of refraction is in green.

$4.8 \cdot 10^{-3}$, $3.4 \cdot 10^{-3}$, and $4.3 \cdot 10^{-3}$ when using maximum smoothness. These increase to $17.8 \cdot 10^{-3}$, $4.7 \cdot 10^{-3}$, and $5.4 \cdot 10^{-3}$ when using the index retrievals from a single angle. This further indicates that multiple viewing angles provide more constraining information than simply improving SNR by using multiple measurements.

Fitting Using Only S0.

While the primary focus of this work is on utilizing polarimetric hyperspectral information, it is also of interest to see how this technique might perform with a purely hyperspectral dataset. The full P-HSI datacube can be reduced to an HSI datacube by only using S_0. To reproduce the effect of not having a polarizer in the instrument, again a two-pixel average is used when fitting the index of refraction.

The results of fitting the quartz window data using only S_0 are shown in Figure 38. The rms error between the median retrieved index and truth is 0.147 in n and 0.205 in κ — which is approximately a factor of two worse than when using both S_0 and P in conjunction with one another. The pixel-to-pixel variability on the other hand is actually slightly reduced when only using S_0. The standard deviation across all pixels is 0.048 and 0.056 in n and κ, respectively, compared with 0.060 and 0.057

112
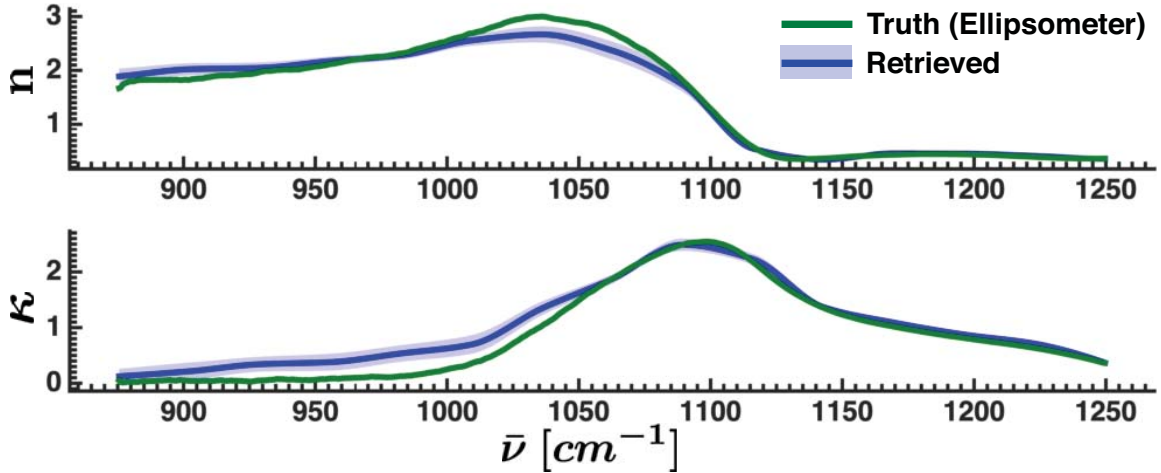
Figure 38. Retrieved (blue) and true (green) index of refraction for a quartz glass window using only a S_0 in the fit. The solid blue line represents the median retrieval across all pixels and the shaded blue region represents plus/minus two standard deviations. The green line is taken from ellipsometry measurements.

when using both S_0 and P. The retrieved downwelling and object temperatures are also slightly more accurate 387.9±1.7 and 293.9±2.2 K compared to the expected 388.2 and 294.7 K. Recall the retrieved temperatures when using both S_0 and P were 386.4±1.4 and 298.1±1.2 K.

Figure 39 shows the retrieved S_0 values (black) compared with the measured (blue). For dramatically undersampling the spectrum — 583 spectral points are modeled by 15 knots — the retrieval does fairly well. Still, there are some errors
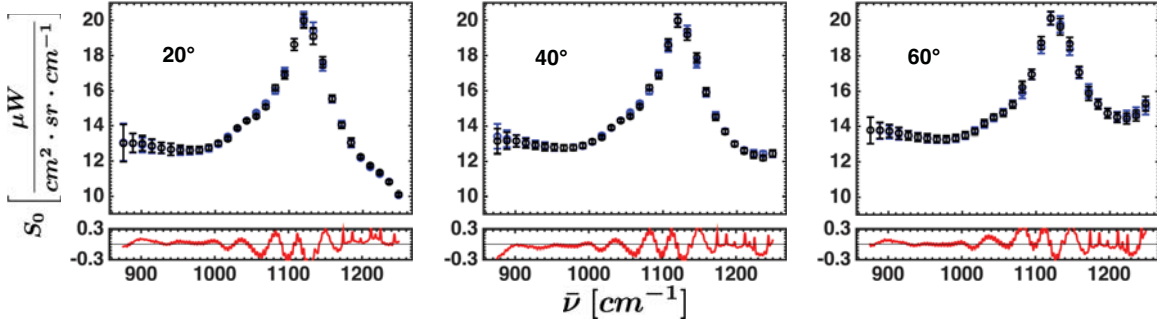
Figure 39. Measured S_0 (blue) compared with retrieved (black) for when fitting only S_0 for the quartz block data. The error bars represent plus/minus two standard deviation across all pixels. The plots in red below each pane represents the error between measured and retrieved.

113

generated by this undersampling which are evident in the residuals, specifically the oscillations near 1100 cm^{-1}. The rms difference between the median retrieved and measured S_0 is 0.129 $\frac{\mu W}{cm^2 \cdot sr \cdot cm^{-1}}$, which interestingly is not much of an improvement over the 0.133 $\frac{\mu W}{cm^2 \cdot sr \cdot cm^{-1}}$ error in S_0 when fitting both S_0 and P.

Similar results are also seen when examinining the beaker dataset. Figure 40 shows the retrieved index using only S_0, but fitting each row of the image as opposed to each pixel. Again, the error is significantly worse than when using both S_0 and P. The rms error in n and κ is 0.235 and 0.239, respectively, compared to 0.135 and 0.180 when using both S_0 and P. This error is very likely due to the fit falling into a local minimum, however. The rms error in S_0 across all pixels and spectral points is 0.153 $\frac{\mu W}{cm^2 \cdot sr \cdot cm^{-1}}$ compared to a 0.146 $\frac{\mu W}{cm^2 \cdot sr \cdot cm^{-1}}$ rms error in S_0 when forward modeling the fitted values using both S_0 and P. This makes the results difficult to analyze but again emphasizes the point that adding polarimetric information can greatly aid the fit in avoiding these local minima.

5.3   Outdoor Measurements

To test the refractive index retrieval on real data under atmospheric downwelling, an experiment was conducted on the AFIT roof. The test was done on the rooftop to avoid adjacency effects from nearby buildings from affecting the data. A number of different materials were arrayed on a board which could be adjusting to different angles. This allowed for multiple viewing angles to be collected with minimal time difference between each angle. This is analogous to a sensor flying past or around a target of interest and observing it from multiple angles. Figure 41 shows the layout of the target array. The instrument was set up approximately 10 m from the target board corresponding to a sampling distance of approximately 3.5 mm per pixel providing many pixels on all targets. The instrument was tilted to look down at a declination
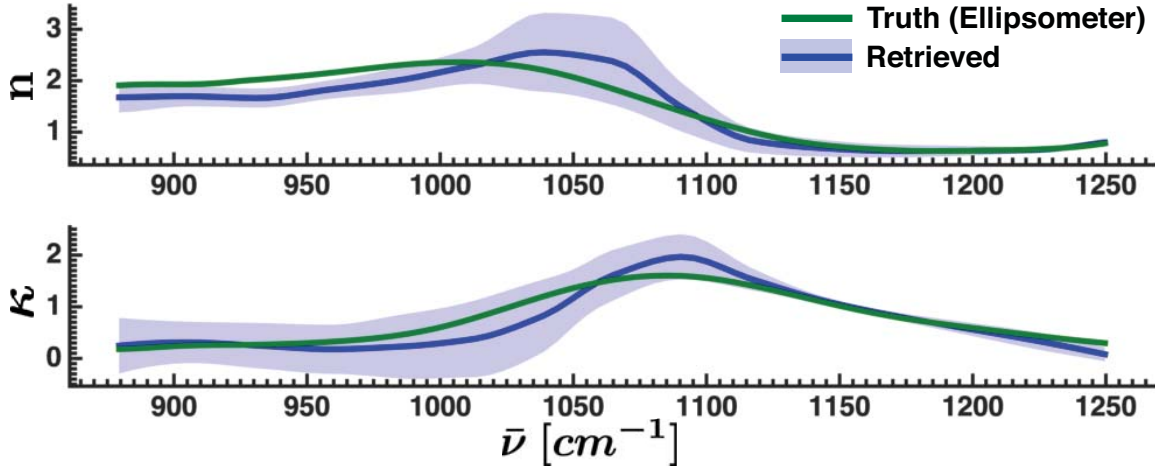
Figure 40. Retrieved (blue) and true (green) index of refraction for a heated Pyrex beaker using only a S_0 in the fit. The solid blue line represents the median retrieval across all pixels and the shaded blue region represents plus/minus two standard deviations. The green line is taken from ellipsometry measurements.

angle of $10°$. The primary targets of interest for this research are the Silicon Carbide blocks, the fused silica wafers, and the sapphire glass. The gold mirrors are in the scene to provide an estimate of directional atmospheric downwelling and the infragold gives an estimate of diffuse downwelling.

Thermocouples were attached to samples of the SiC and fused silica placed outside the scene to get rough estimates of the temperatures of those materials at the time of the data collect. When the instrument was calibrating, temperature measurements of each object on the board were taken using an Exergen D501 infrared thermometer. Additionally, air temperature, relative humidity, and pressure measurements were taken intermittantly throughout the data collect using a Kestrel 4000 series handheld weather station.

In total, eight tests were done over the course of two days with a variety of instrument settings, each observing the targets at a number of different viewing angles. The settings for each test are summarized in Table 2. The instrument stopped recording datacubes during test 14-5 and had to be rebooted so that test did not provide
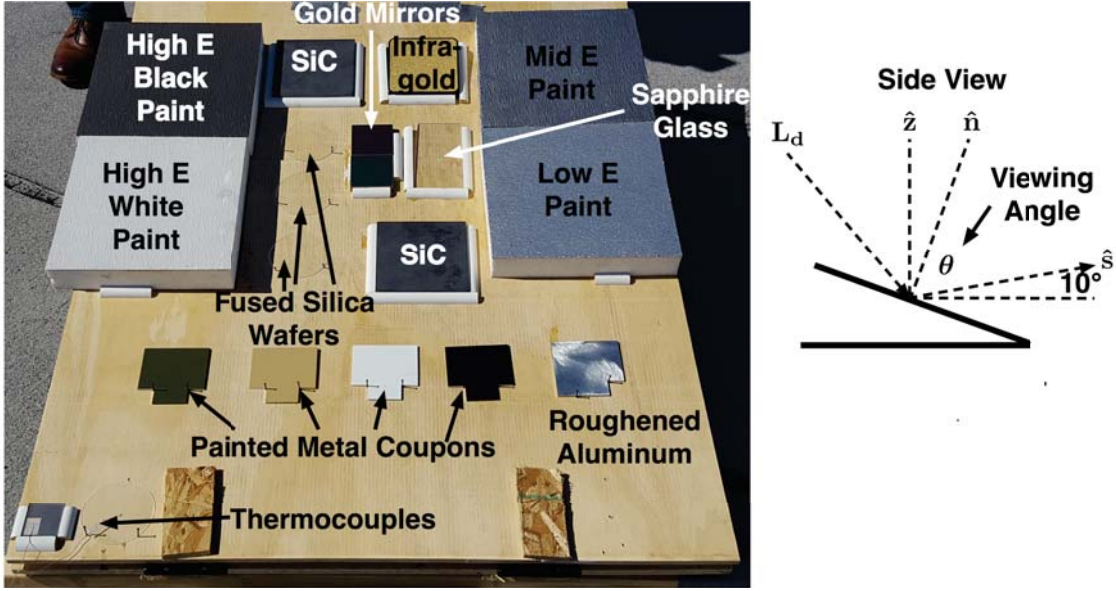
Figure 41. Layout of the target array measured from the AFIT rooftop. The targets of interest for this work are the SiC block, fused silica wafers, and sapphire glass. The gold mirrors and infragold provide estimates of directional and diffuse downwelling, respectively.

any data. For each test except for 13-1, calibration cubes were collected at all four polarizer angles at the beginning and end of each test as opposed to the beginning and end of each individual viewing angle measurement. This was done in an attempt to minimize scene drift. Because of complications with the control software, test 13-1 was conducted using the more traditional method of calibrating before and after each viewing angle. For test 14-7 an additional calibration was performed in the middle of the test. Most of the analysis presented in this section, unless stated otherwise, are done on test 14-4 although all datasets have been at least partially analyzed.

Silicon Carbide.

One of the targets of interest in the scene was SiC. Unlike the highly pure wafer used in the laboratory measurements, this was a ceramic block of SiC. Because this is a ceramic material, the lattice structure is expected to be randomly distributed meaning the birefringence model was not necessary to describe the index of refraction

Table 2. Summary of settings for each test collected from the AFIT roof on 13 and 14 April 2016. The instrument stopped recording datacubes during test 14-5 so no useable data was obtained from that test.

ID	Start Time (GMT)	End Time (GMT)	Viewing Angles	Res. $[cm^{-1}]$	# Acq.	Window Size
13-1	1852	1925	70, 75, 80	8	8	320x150
14-1	1406	1500	20, 40, 60	8	8	320x256
14-2	1501	1525	20, 40, 60	16	4	320x256
14-3	1532	1557	20, 40, 60	8	2	320x256
14-4	1902	1944	30, 50, 70	1	2	320x80
14-5	2015	2025	30, 50, 70	1	2	320x256
14-6	2042	2140	30, 50, 70	4	4	320x256
14-7	2141	2241	20, 30, 40, 50, 60, 70	8	4	320x256

for this sample. This adds a complication, however, in that there is less control over contaminants which could potentially be an issue based on what is seen in the data.

Figure 42 shows the measured S_0 and P compared to what is expected based on the expected index of refraction and the measured object temperature and downwelling radiance. Because the SiC sample was black in the visible, it was difficult to properly align in the ellipsometer. This caused significant errors in the ellipsometry measurement, so instead, the expected values for the index of SiC were taken from the database in the Woollam software package. Clearly, there is significant error, especially at frequencies below 1000 cm^{-1}. There is also significantly more pixel-to-pixel variability in this spectral band. Figure 43 shows the spatial distribution of the radiance averaged over the spectral band from 875-975 cm^{-1}.

It is clear that there is a non-random spatial distribution to this spectral feature. This is possibly an indication of contaminants which are spread in varying concentrations across the SiC block. SiC becomes very reflective below 1000 cm^{-1} and this
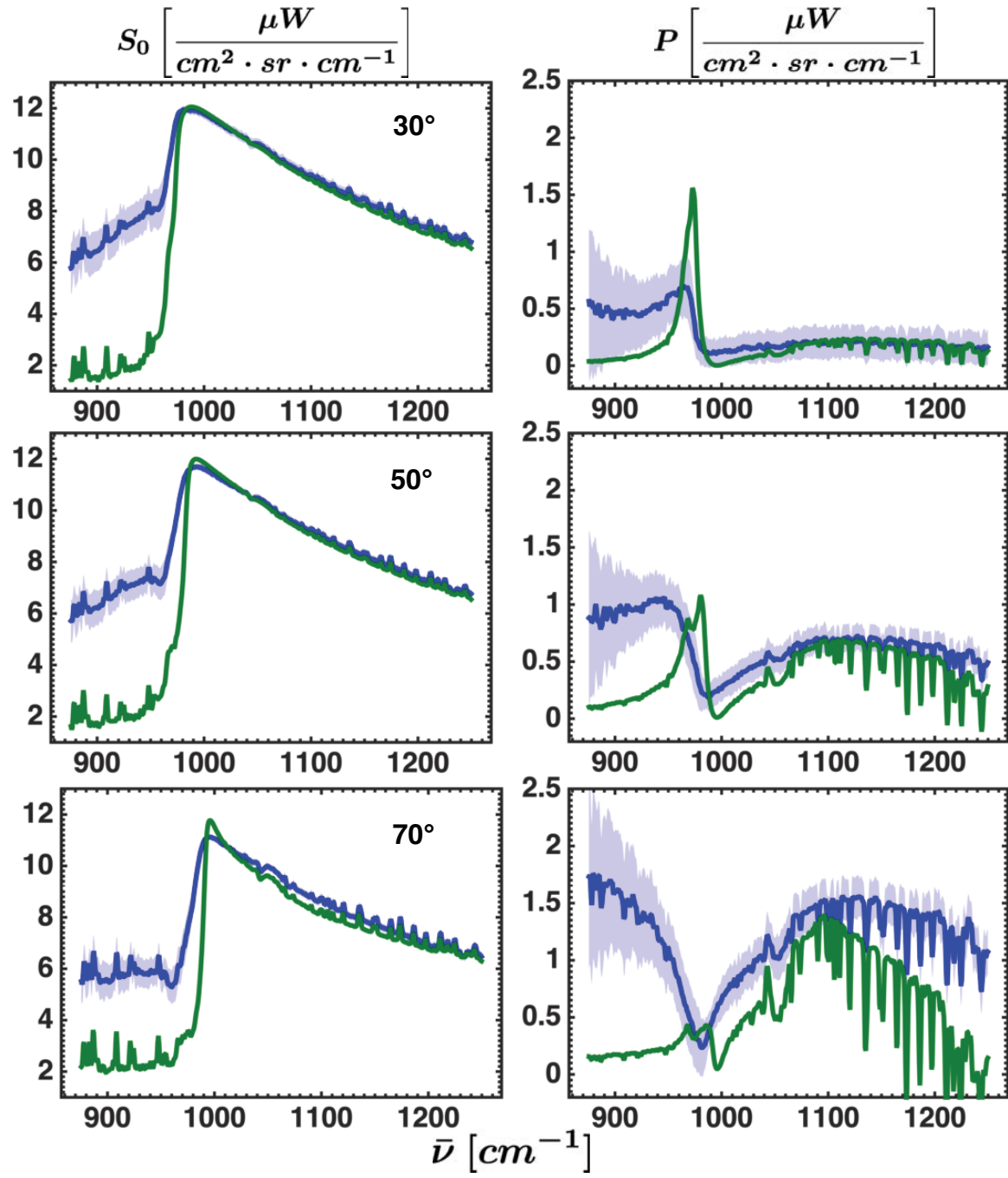
Figure 42. Measured (blue) compared with expected (green) S_0 and P for the SiC block data. The shaded blue region represent plus/minus two standard deviation across all pixels.

118
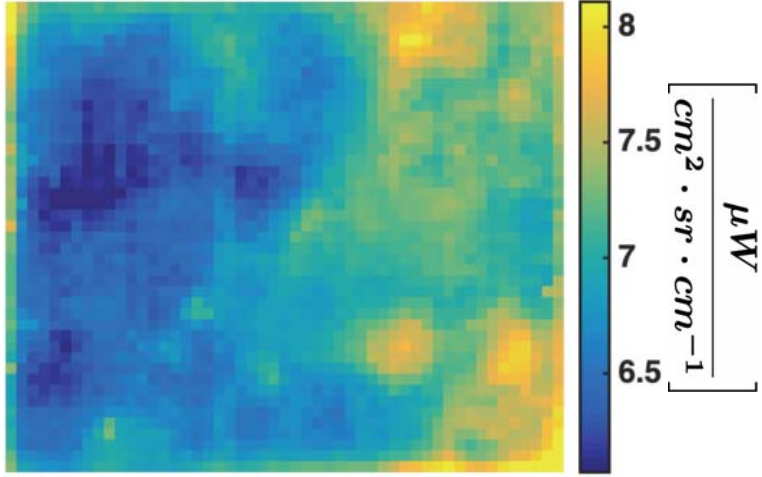
Figure 43. Band-averaged radiance map of the SiC used in outdoor testing. The average is taken over all spectral points from 875-975 cm^{-1}. This shows a clear spatial patterning of the spectral anomoly seen in Figure 42.

contaminant seems to be blackbody-like, raising the effective emissivity of the sample. To properly account for this effect, some sort of mixing model would have to be incorporated, but that is outside the scope of this work. In spite of all of this, the fit is still applied to the data. Figure 44 shows the retrieved index of refraction. In order to partially account for the potential contaminants, two oscillators are used in the fitting. This is probably not the best way to compensate for the effect, but it can at least partially account for it.

The "true" index of refraction presented is merely the index of refraction for SiC, taken from a database as described earlier. Without knowing what the contaminant might be and without being able to get accurate ellipsometry data off of the sample, it is impossible to get a good estimate of what the true index of refraction should look like. This means that comparing the index of refraction fit is not really useful. Instead, it is more illuminating to see how well the fitted values replicate the measured S_0 and P spectra. This is shown in Figure 45.

Clearly the fitted parameters do a much better job of replicating the S_0 and P spectra than the expected parameters do. Still, however, there are significant

119
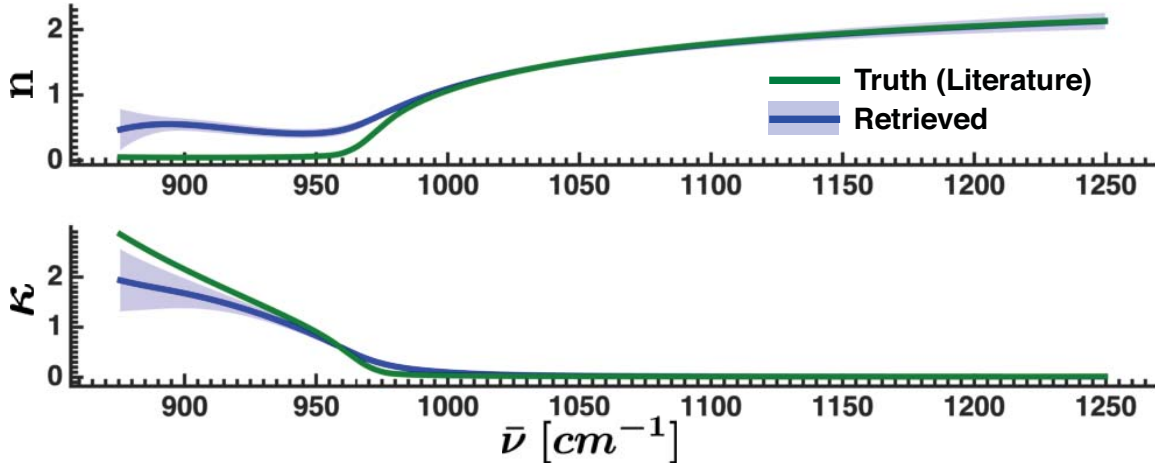
Figure 44. Retrieved (blue) and "true" (green) index of refraction for a ceramic SiC block. The solid blue line represents the median retrieval across all pixels and the shaded blue region represents plus/minus two standard deviations. The green line is taken from the SiC values from the JA Woollam ellipsometry WVASE software database. [31] As discussed, due to complications, likely contamination, this is not a good model for the index of refraction of the block. Without knowing the contaminant, however, it is impossible to get a good estimate of the "true" index of refraction.

differences between the retrieved S_0 and P and what is measured. This indicates the need to develop and incorporate into the fit some kind of mixing model, but that is outside the scope of this work. Another thought on what could be causing the variations from expectation below 1000 cm^{-1}, where SiC becomes highly reflective, is if something warm near the SiC block is being diffusely reflected into the sensor. This would also mean the SiC block violates the smooth surface assumption used in the rest of this work. To test this hypothesis, an option to include adjacency effects was added to the fit. Essentially, this accounts for the downwelling as some mix of sky downwelling and blackbody-like adjacency effects from nearby objects. Both an adjacency percentage, accounting for how much of the downwelling is coming from the nearby object and the temperature of the object are added as fit parameters. Figure 46 shows the results of this retrieval.

Again, however it is of more interest to see how well the fit replicated the measured spectra. The retrieved and measured S_0 and P at all three viewing angles are shown in

120
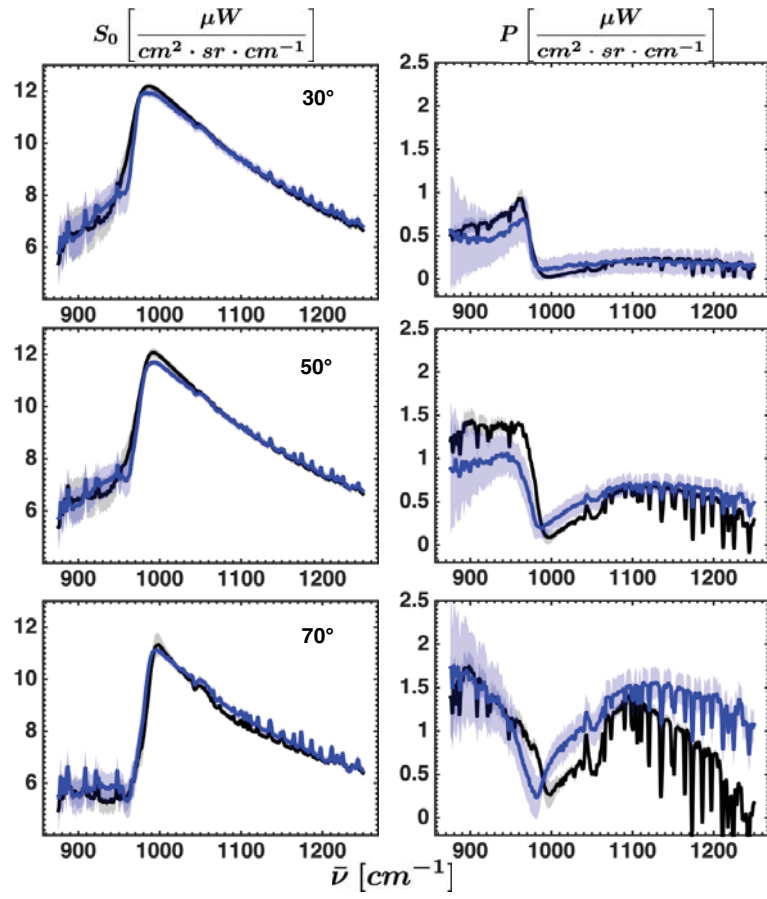
Figure 45. Measured (blue) compared with retrieved (black) S_0 and P for the SiC block data using the atmospheric downwelling fit. The shaded regions represent plus/minus two standard deviation across all pixels.

121
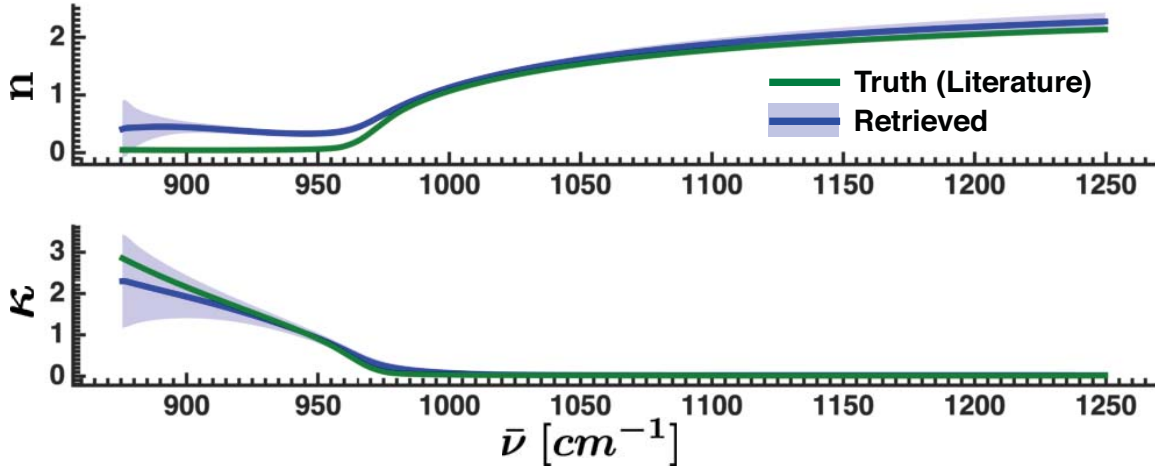
Figure 46. Retrieved (blue) and "true" (green) index of refraction for a ceramic SiC block after adding adjacency effects to the fit. The solid blue line represents the median retrieval across all pixels and the shaded blue region represents plus/minus two standard deviations. The green line is taken from the SiC values from the JA Woollam ellipsometry software database. [31] As discussed, due to complications, likely contamination, this is not a good model for the index of refraction of the block. Without knowing the contaminant, however, it is impossible to get a good estimate of the "true" index of refraction.

Figure 47. The rms difference between the retrieved and measured across all viewing angles, spectral points, and pixels is $0.260 \frac{\mu W}{cm^2 \cdot sr \cdot cm^{-1}}$ in S_0 and $0.193 \frac{\mu W}{cm^2 \cdot sr \cdot cm^{-1}}$ in P. This is significantly better than the rms error of $0.300 \frac{\mu W}{cm^2 \cdot sr \cdot cm^{-1}}$ and $0.357 \frac{\mu W}{cm^2 \cdot sr \cdot cm^{-1}}$ when adjacency effects are not accounted for. It is unclear, however, how much of this effect is simply due to having more fit parameters rather than those fit parameters truly describing the actual physics in play.

Fused Silica Wafer.

Another material examined in the outdoor test was a set of fused silica (quartz) glass wafers. These have a virtually identical index of refraction to the quartz glass block window examined earlier. Unlike the SiC data, the expected and measured S_0 and P are quite similar as shown in Figure 48, though there are some discrepancies especially the 70° viewing angle.

122
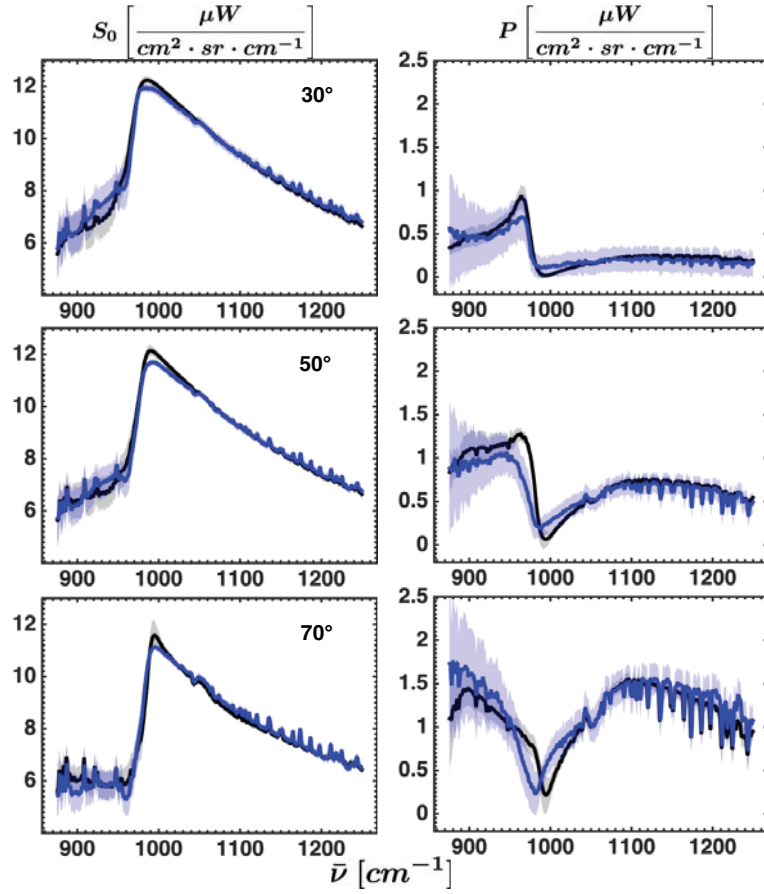
Figure 47. Measured (blue) compared with retrieved (black) S_0 and P for the SiC block data when including adjacency effects in the fit. The shaded regions represent plus/minus two standard deviation across all pixels.
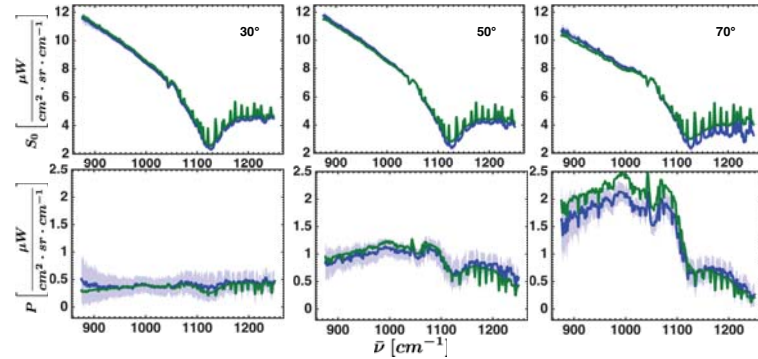
Figure 48. Measured (blue) compared with expected (green) S_0 and P for the fused silica wafer data. The shaded blue region represent plus/minus two standard deviation across all pixels.
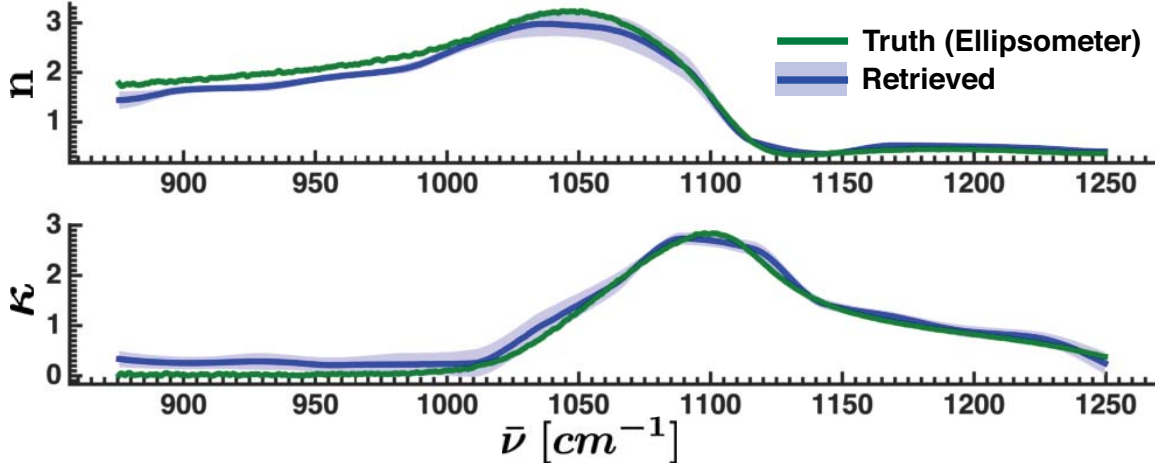
Figure 49. Retrieved (blue) and true (green) index of refraction for a fused silica wafer. The solid blue line represents the median retrieval across all pixels and the shaded blue region represents plus/minus two standard deviations. The green line is taken from the ellipsometry measurements.

The retrieval done on this data is also quite accurate. Figure 49 shows the retrieved index. The rms error between the median retrieved index and the true index is 0.164 and 0.158 in n and κ, respectively. The fit is also very consistent pixel to pixel, the rms standard deviation is 0.068 for n and 0.085 for κ. The largest source of error seems to be in the atmospheric retrieval where the water lines specifically show the greatest discrepency between measured and retrieved. The effect of this is seen when comparing the retrieved S_0 and P with the measured in Figure 50.

Because of this error in the atmospheric compensation, it is interesting to see how the fit performs when the atmosphere is held fixed. Specifically, the gold mirror is used to get an in-scene estimate of the downwelling radiance. To correct for the small — but possibly significant — emissivity of the gold mirror, greybody radiance with an emissivity of 0.03 and a temperature of 305 K is subtracted from the gold mirror pixels radiance to give a more accurate estimate of the true downwelling. This is used as the downwelling radiance in the fit instead of fitting to the best modeled atmosphere. The results of this fit are shown in Figure 51.
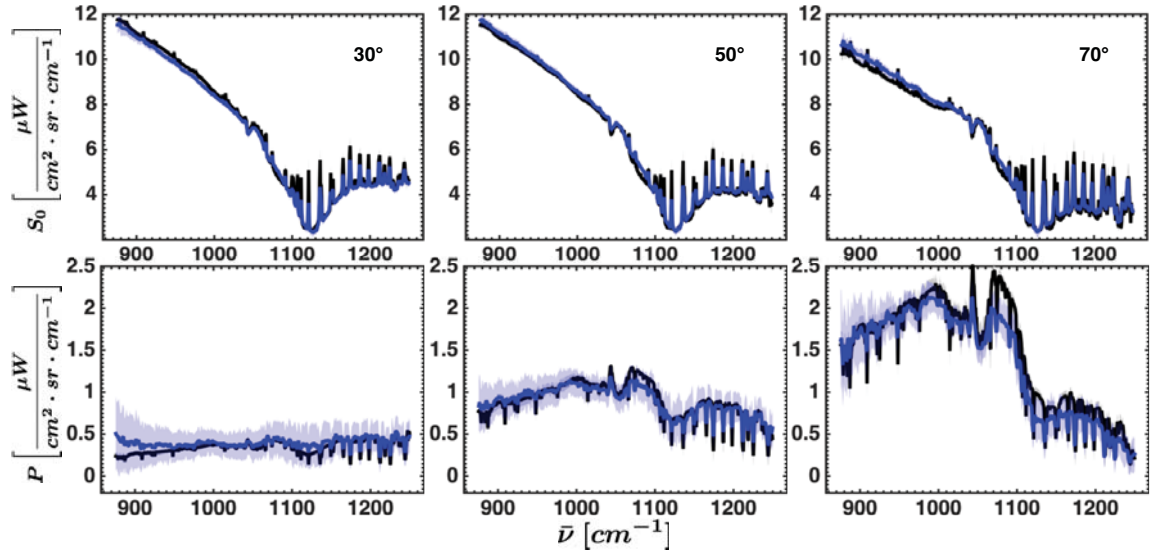
Figure 50. Measured (blue) compared with retrieved (black) S_0 and P for a fused silica wafer. The shaded regions represent plus/minus two standard deviation across all pixels.
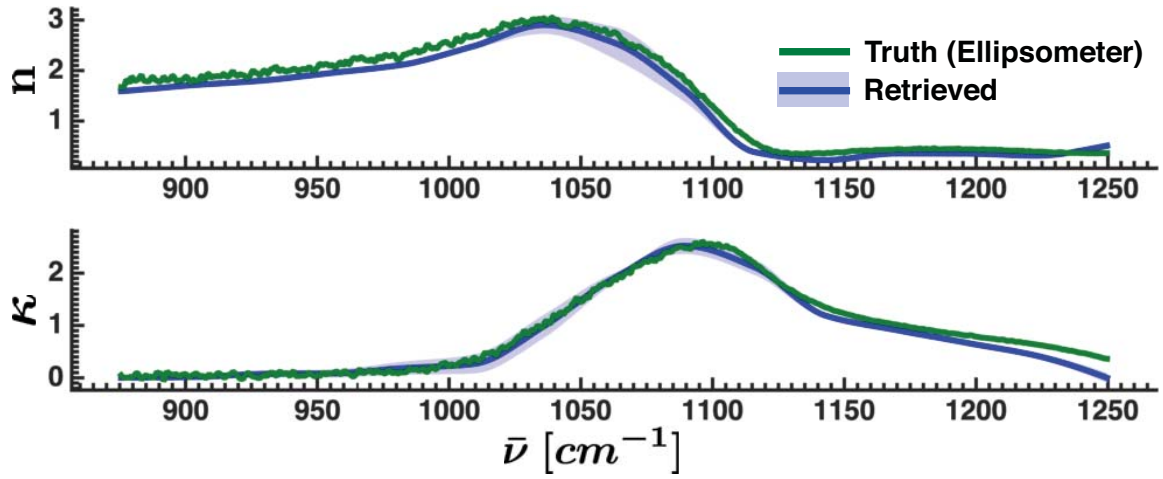
Figure 51. Retrieved (blue) and true (green) index of refraction for a fused silica wafer when not fitting the atmospheric parameters. Atmospheric downwelling radiance is instead estimated from the gold mirror placed in the scene. The solid blue line represents the median retrieval across all pixels and the shaded blue region represents plus/minus two standard deviations. The green line is taken from the ellipsometry measurements.

125

In this case, the fit is more accurate and self-consistent than when fitting the atmospheric parameters. The rms error in the median retrieved index is 0.155 in the real component and 0.117 in the imaginary. The rms standard deviation in n is 0.059, and in κ, it is 0.056. There is still a significant difference in the retrieved P, however, especially at larger viewing angles and in the ozone band. The amount of polarization is underestimated in this region which may indicate that the assumption of the downwelling radiance being unpolarized is not valid. A more detailed study would need to be conducted to properly answer this question, however.

Once more, these results are compared with the maximum smoothness TES algorithm. Again, a two-pixel average is used when performing the TES fit to mimic the effect of a sensor without a polarizer. Because TES requires atmospheric compensation as an input, the fixed atmosphere index retrieval is used as the basis of comparison. The results of the comparsion are shown in Figure 52. The error between 1200 and 1250 cm^{-1} in the 70° retrievals are most likely due to noise causing the measured radiance to be less than the measured downwelling radiance at these pixels. While some compensation was done to account for the small emissivity of the gold mirror, without the true emissivity spectra of the mirror, the simple 0.03 emissivity greybody correction may not be sufficient.

Still, for most wavelengths, the retireval is very accurate. The rms error in the retrieved emissivity was 0.025, 0.036, and 0.033 for 30°, 50°, and 70°, respectively. The TES algorithm performs better at 30° with an rms error of 0.010, but worse at 50° and 70° — rms error of 0.049 and 0.079. When spectral points above 1200 cm^{-1} are ignored, the rms error at 70° is reduced to 0.024 for the index retrieval and 0.032 for the TES algorithm. The spectral angle between the retrieved and expected emissivities are 1.5°, 3.0°, and 3.3° for the index retrieval, and 0.8°, 2.4°, and 7.9° for the TES algorithm. Again, when ignoring points over 1200 cm^{-1}, the spectral angle
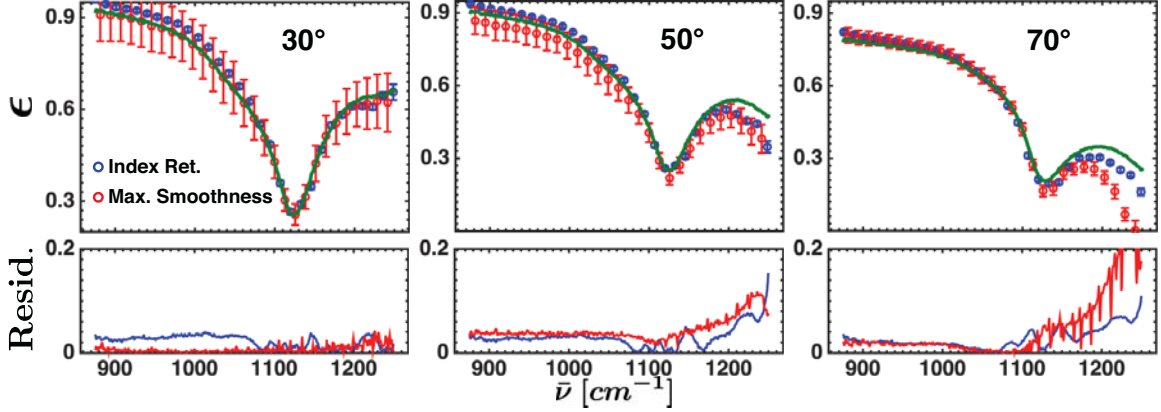
Figure 52. Comparison of the emissivity retrieved via maximum smoothness TES (red) and the method developed in this work (blue) at all three viewing angles for a fused silica wafer. The true emissivity generated by forward modeling the ellipsometry measured index of refraction is in green.

difference in the 70° retrievals is significantly reduced to 2.1 for the index retrieval and 3.0° for the TES. The most noticable difference between the two methods is the pixel-to-pixel variability. The rms standard deviation across all pixels — i.e. half the size of the errorbars in Figure 52 — is 0.004 for all angles using the index retrieval. When using the TES algorithm, this is increased to 0.040, 0.026 and 0.014 for the three angles. Finally, the retrieved temperatures are also important to consider. For the index retrieval, the estimated object temperature is 301.2±0.4 K compared to the expected based on in-situ measurements with the contact probe of 304.3±1.0 K. The TES retrieved temperatures were 302.2±3.1 K, 306.9±1.9 K, and 304.2±1.0 K at the three angles.

It is significant to see what effect, if any, spectral resolution has on the retrieval. Figure 53 shows the retrieval from data at 8 cm^{-1}. The fit is almost identical to the fit conducted on the 1 cm^{-1} data. The rms difference between the median retrieved and expected index is 0.162 in the real component and 0.171 in the imaginary. The pixel-to-pixel consistency is also almost identical to the 1 cm^{-1} fit. The rms standard deviation across all pixels is 0.062 in n and 0.080 in κ.
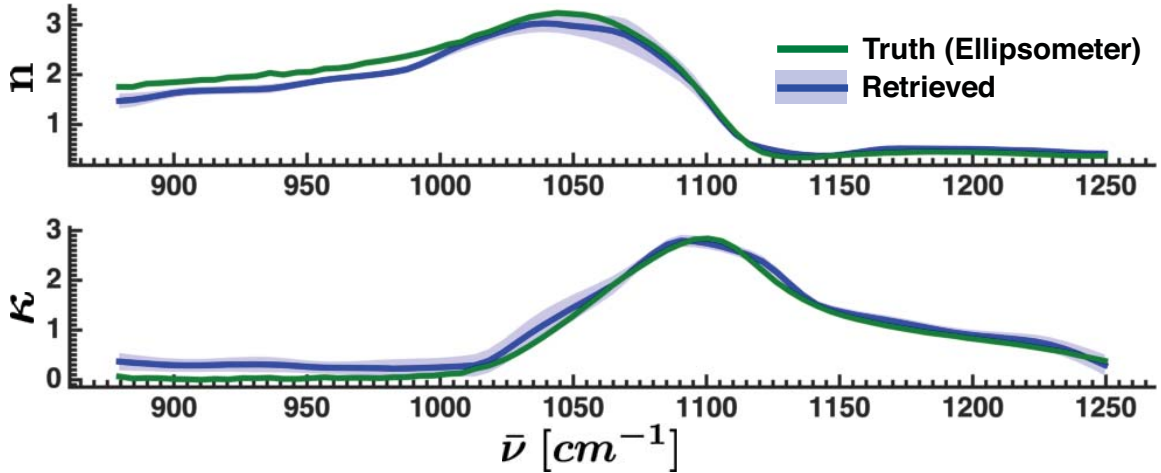
Figure 53. Retrieved (blue) and true (green) index of refraction for a fused silica wafer based on data taken at 8 cm^{-1}. The solid blue line represents the median retrieval across all pixels and the shaded blue region represents plus/minus two standard deviations. The green line is taken from ellipsometry measurements.

It is also interesting to see how this fit will perform using only a single viewing angle. Figure 54 shows the results of performing the retrieval on all three viewing angles independently. As with the laboratory data, there is generally good agreement between the retrieved and expected, but the fit is susceptible to converging to wildly different solutions based on small measurement errors. The 70° data where this effect is worse seems to converge to two sets of solutions, one very near the true solution and the other, slightly more prevalent solution is what is shown in the median retrieval. Again, this illustrates one of the difficulties with estimating index of refraction as well as the added utility of incorporating multiple viewing geometries into the fit.

Finally, as in the last section, the fit is also examined using only S_0. Figure 55 shows the retrieval fitting only to the S_0 data. Again, as with the laboratory data, this fit is not nearly as accurate as when using both S_0 and P, but it is still reasonably accurate. The rms error is 0.264 in n and 0.546 in κ. The pixel-to-pixel variablility is also larger. The rms standard deviation across all pixels is 0.115 for n and 0.132
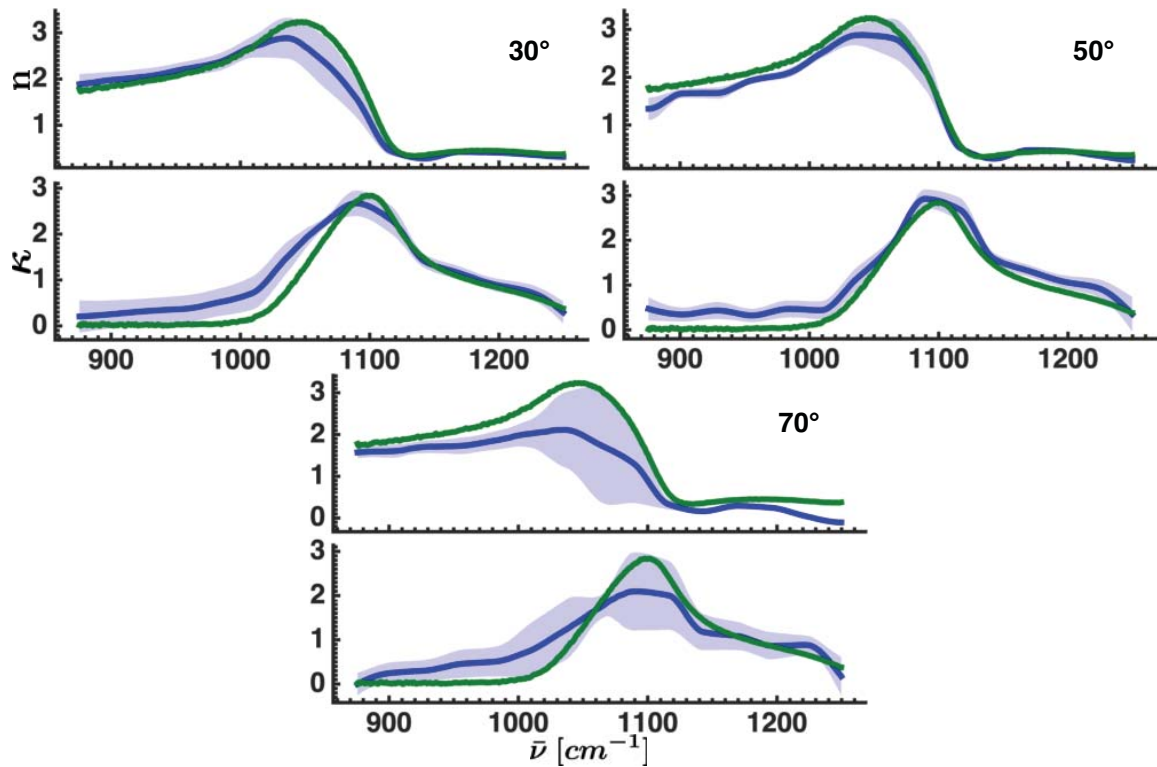
Figure 54. Retrieved (blue) and true (green) index of refraction for a fused silica wafer using only a single viewing angle. The solid blue line represents the median retrieval across all pixels and the shaded blue region represents plus/minus two standard deviations. The green line is taken from ellipsometry measurements.

129

for κ. This is a further demonstration of the utility of combining polarimetric and hyperspectral information in this fit.

Sapphire Glass.

The final material examined for this work was a sample of sapphire glass. Despite being a glass, this material well modeled by the Lorentz oscillator model. Because sapphire is so emissive across much of the LWIR, ellipsometry measurements were difficult to make. Because of this, again the index of refraction values were taken from the Woollam software database.[31] Unlike the SiC, however, reasonable measurements were obtained for a small part of the band of interest. In this region, there is reasonable agreement between the measured and modeled values.

Figure 56 shows the retrieved index for sapphire using the Lorentz oscillator model to fit the index. For the most part, there is very good agreement except from about 875-900 cm^{-1}. The rms error in n and κ are 0.060 and 0.017, respectively. Additionally the fit is very consistent as the rms standard deviation across all pixels is only 0.010 and 0.011 in the real and imaginary component. While this fit does a good job of retrieving the index of refraction, the retrieved values do not model the measured S_0 and specifically P well. Figure 57 shows the retrieved S_0 and P compared to the measured.

Sapphire is highly birefringent, but because this was a glass sample it was expected that the lattice structure would be mixed, essentially negating the effect of the birefringence and giving the material an effective index of refraction roughly equal to the average of the ordinary and extrodinary ray indices. This was not the case, however, as is clearly evident in Figure 57. The measured P being significantly greater than the retrieved was an indicator of birefringence before in the SiC laboratory data and again birefringence is the most likely cause of the discrepency between measured and
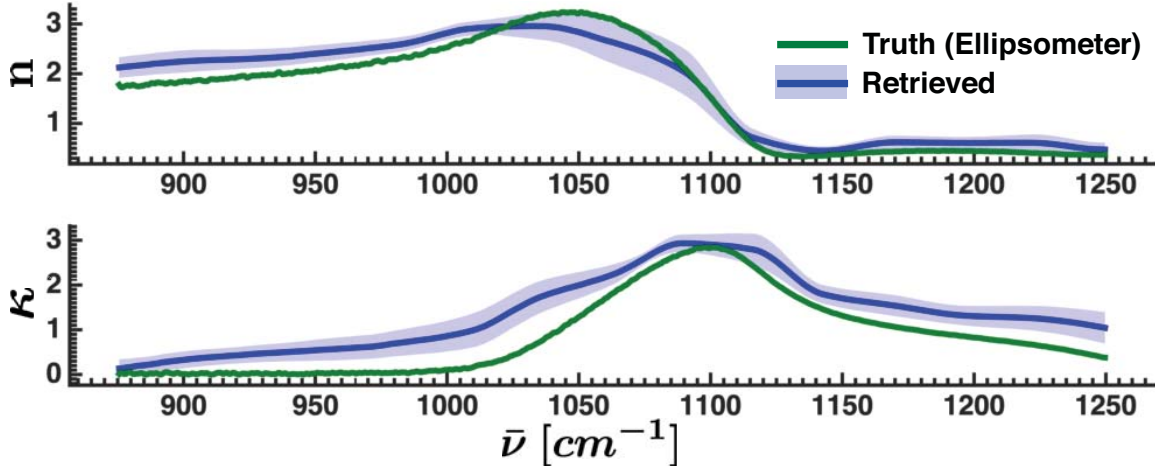
Figure 55. Retrieved (blue) and true (green) index of refraction for a fused silica wafer using only S_0 information in the fit. The solid blue line represents the median retrieval across all pixels and the shaded blue region represents plus/minus two standard deviations. The green line is taken from the ellipsometry measurements.
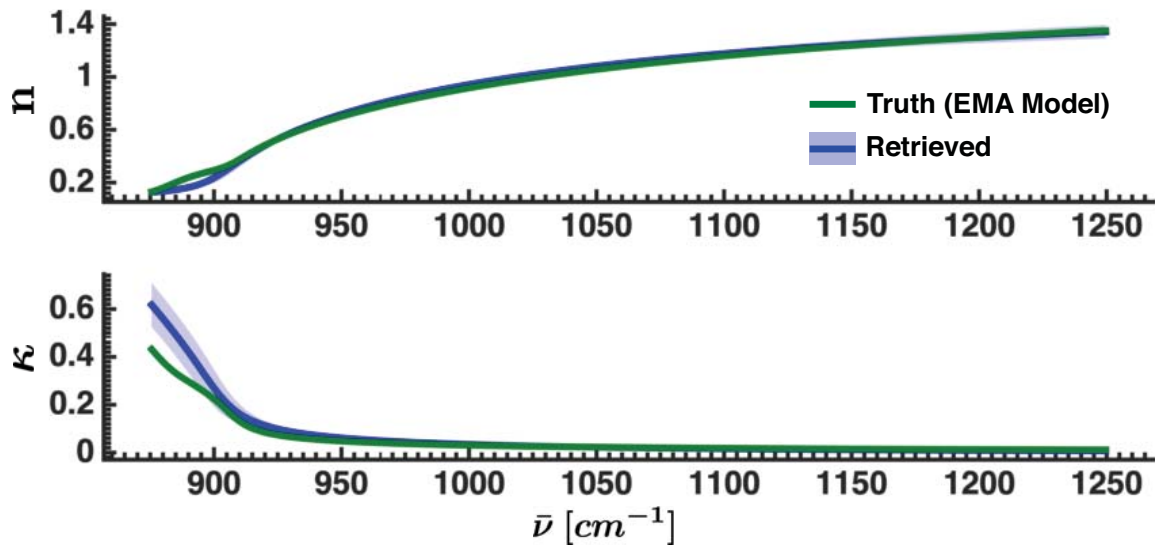
Figure 56. Retrieved (blue) and "true" (green) index of refraction for a sapphire glass window. The solid blue line represents the median retrieval across all pixels and the shaded blue region represents plus/minus two standard deviations. The green line is taken are the values for the index of refraction of sapphire from the JA Woollam ellipsometry software database. [31]

131
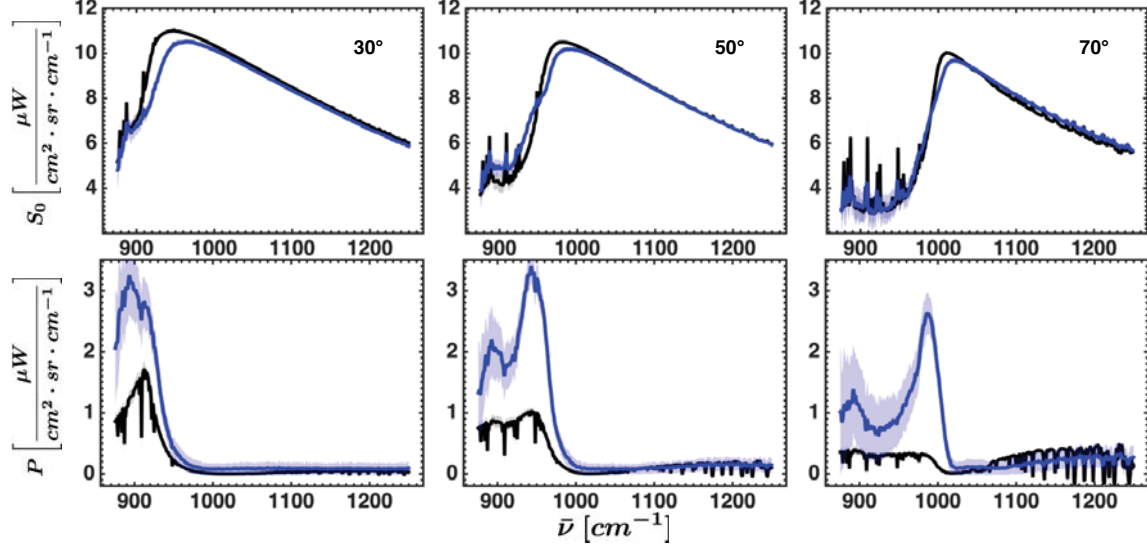
Figure 57. Measured (blue) compared with retrieved (black) S_0 and P for a sapphire window. The shaded regions represent plus/minus two standard deviation across all pixels.

expected here. Because of this, the birefringence model used for the SiC laboratory data was added to the retrieval code. Figure 58 shows the retrieved e- and o- ray indicies of refraction.

Again, this fit is very accurate indicating that the index of refraction can be retrieved under atmospheric downwelling, even for birefringent materials. The rms error in the ordinary ray index is 0.032 and 0.015 in n and κ and the rms error in the extraordinary index is 0.040 and 0.005. The fit is also self consistent with an rms standard deviation across all pixels of 0.009 and 0.010 in n and κ for the o-ray and 0.012 and 0.004 for the e-ray. Accounting for birefringence also does a much better job of replicating the measured S_0 and P, although there are still some unexplained artifacts. Figure 59 shows the retrieved S_0 and P compared with the measured values.

5.4 Summary

In this section, results were presented retrieving index of refraction from synthetic, laboratory, and outdoor polarimetric hyperspectral radiance measurements. The syn-

132
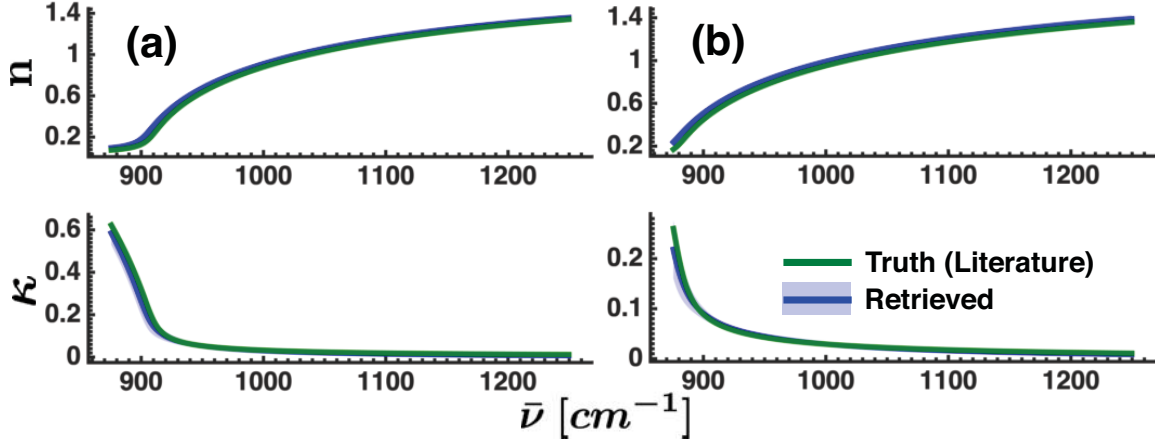
Figure 58. Retrieved (blue) and true (green) index of refraction for both the o- (plot a) and e-ray (plot b) of a sapphire glass window. The solid blue line represents the median retrieval across all pixels and the shaded blue region represents plus/minus two standard deviations. The truth values were taken from existing models used in the JA Woollam IR-VASE ellipsometry software package for both the o- and e- ray indices of refraction for Sapphire. [31]
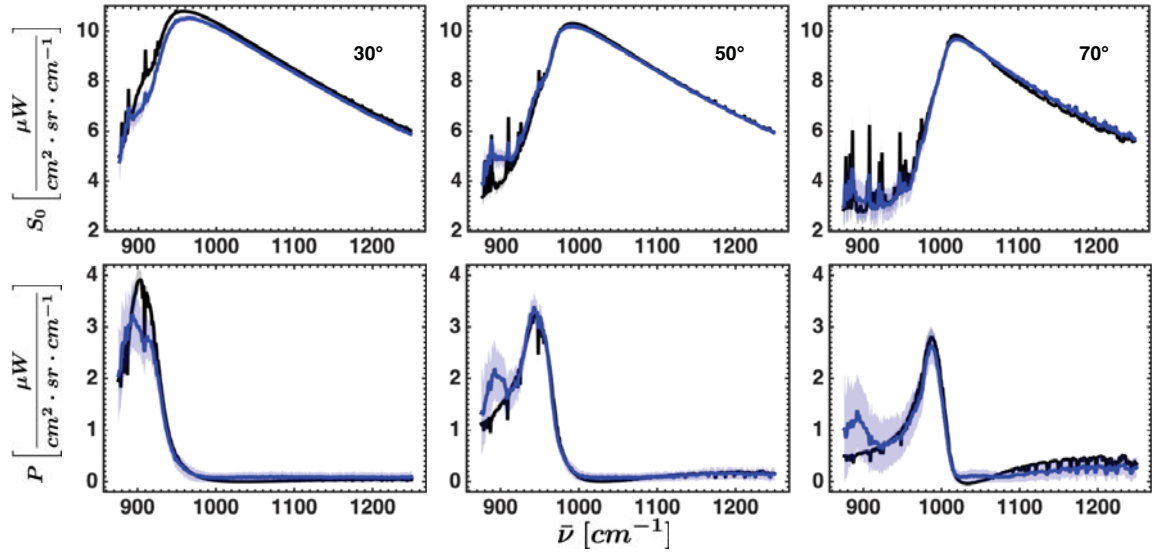
Figure 59. Measured (blue) compared with retrieved (black) S_0 and P for a sapphire window when birefringence is accounted for in the fit. The shaded regions represent plus/minus two standard deviation across all pixels.

133

thetic data helped generate a qualitative understanding of how certain variables affect the retrieval. As expected, the fit improves with decreasing NESR, increasing thermal contrast, and increasing the number of viewing angles used. Interestingly, spectral resolution does not seem to have a large effect on the retrieval accuracy. Laboratory data showed that index of refraction can be retrieved to within 0.08 rms error for both a SiC wafer and fused silica window while simultaneously estimating object temperature and a downwelling temperature representing the brightness temperature of the downwelling radiance. Additionally, the viewing angle can be added as an additional fit parameter and accurately retrieved to within $5°$ while maintaining the accuracy of the index retrieval. Outdoor measurements show that index of refraction can still be accurately retrived even with spectrally structured atmospheric downwelling radiance.

VI. Conclusions

This work presents novel instrumentation, a unique set of data, and a methodology for accurately estimating the spectrally-varying complex index of refraction from passive measurements without *a priori* knowledge of downwelling radiance and object temperature. Specifically, polarimetric hyperspectral imaging data made at one or more non-nadir viewing angles were fit to a physics-based model where n, κ, surface temperature, downwelling radiation (and in some cases surface normal angle) were parameters estimated by nonlinear regression. By utilizing physics-based models, the number of parameters needed to describe the index of refraction can be dramatically reduced. For smooth, specularly-reflecting surfaces, the Fresnel equations can be used to relate index of refraction to reflectivity, which in turn can be used to model the measured polarimetric hyperspectral radiance. Because the spectral variation of index of refraction is modeled, reducing the number of parameters, the problem of determining index of refraction from polarimetric hyperspectral radiance measurements can be made overdetermined while simultanously solving for downwelling radiance and object temperature.

Various aspects of the performance of this methodology were assessed using both synthetic and measured data. Simulated data qualitatively demonstrated how the index estimation depends on thermal contrast, sensor NESR, spectral resolution, and the number and range of viewing angles. From these datasets, fit accuracy scales approximately exponentially with temperature contrast and linearly with sensor NESR at least over reasonable ranges for each quantity. Spectral resolution had little effect on the accuracy of index estimates, and this was largely driven by the trade-off of increased NESR with improved resolution. However, both synthetic data and measurements were performed for short distances where highly structured atmospheric absorption features could be ignored, so this observation may not hold for longer path

data collections. Viewing farther off nadir generally improved the index estimates, a result expected given the increased polarization with angle. Finally, measurements at multiple angles significantly increased the accuracy of index estimates when compared to those made using a single viewing angle.

The complex index of refraction retrieval method was tested on a series of measurements taken indoors with controlled laboratory conditions. The first dataset made observations a heated Pyrex beaker which produced a vertical temperature gradient and a range of surface normals laterally traversing the beaker. The index of refraction was retrieved to with 0.090 rms error in the real component and 0.222 in the imaginary component. Significant variability in the index estimates were observed and resulted from radiometric scene drift caused by the hot plate's intermittent heating cycles. When only pixels with the least scene drift were used in the retrieval, the rms error was reduced to 0.085 and 0.179 in n and κ, respectively. Additionally, the retrieval results were found to be uncorrelated with beaker temperature. These results demonstrated the ability to retrieve n and κ in P-HSI measurements of a target dominated by thermal emission.

Next, a SiC wafer target was examined in reflection mode by using a heated, wide-area blackbody reflecting off the wafer to induce a necessary thermal contrast. The birefringent nature of this crystalline SiC wafer required adaptation of the model to accommodate a different index of refraction based on the polarization state of the incident light. The ordinary ray refractive index was retrieved to within 0.043 and 0.067 rms error in n and κ, respectively, and the extraordinary ray index was retrieved to within 0.066 and 0.114 rms error, respectively. Additionally, the retrieved index was relatively consistent with the standard deviation across all pixels and never exceeded 0.064. Both the object and downwelling temperatures were also accurately retrieved without any *a priori* inputs, which is a novel contribution. Additionally,

the ability to solve for the indices of refraction of birefringent media from passive measurements has been demonstrated for the first time.

A third set of laboratory measurements were made of a quartz glass block, again in reflection-mode by using a heated, wide-area blackbody to create thermal contrast. Here, the index was retrieved to within 0.072 for the real component and 0.062 for the imaginary component. The fit was again self-consistent as judged by the standard deviation across all pixel-wise index estimates of 0.060 and 0.057 for the real and imaginary components, respectively. Furthermore, results from the quartz glass block were shown to outperform the maximum smoothness temperature-emissivity separation (TES) technique. When using TES with S_0 — i.e., the standard hyperspectral image — the rms error increased to 0.147 and 0.205 in n and κ respectively. Finally, when only a single angle was used in fitting, the retrievals were also less accurate and much more susceptible to fitting challenges due to local minima. These local minima represent one of the potential drawbacks of this methodology for estimating index of refraction. Utilizing both polarimetric and hyperspectral information, as well as multiple viewing angles — which is unique to this work — significantly improves regression performance by adding information which reduces the impact of local minima.

Another avenue investigated in this research effort is the ability to simultaneously estimate index of refraction and the angle of the surface normal with respect to the sensor. Results from the heated Pyrex beaker show that the surface normal can be obtained to within about 1 degree error when factors like temperature drift are properly accounted for. Furthermore, including surface normal angle in the fit did not significantly degrade the accuracy of the retrieved index. Similar analysis using the quartz block data was consistent with these findings: surface normal angle was retrieved to within about 1 degree error while maintaining accuracy in the index of

refraction retrieval. Furthermore, the quartz dataset showed that the retrieval is very consistent pixel-to-pixel with greater than 50% of the retrieved angles lying within 0.25 degrees of the median retrieval for all viewing angles.

To test this index of refraction retrieval method under operationally relevant atmospheric downwelling radiation, a number of measurements of a target board containing several materials were made outdoors under daytime clear sky conditions. Complications, potentially due to contamination made SiC data collected outdoors difficult to analyze. Adding adjacency effects and multiple oscillators to the model, however, allowed the S_0 and P spectra to be reasonably described by the fit. The index of refraction of a fused silica was was retrieved to with 0.155 rms error in n and 0.117 error in κ. Spectral resolution did not seem to have any significant effect on the retieval as expected based on the synthetic dataset discussed earlier. Again, these results were shown to compare favorably to the maximum smoothness TES algorithm. Finally, a sapphire window was examined and the index was again retrieved quite accurately with rms error of less than 0.04 for both n and κ of both the o- and e-ray indices. Furthermore, this fit was very consistent with the rms standard deviation across all pixels never exceeding 0.012.

While the data and analysis presented here is promising, it is important to realize that this work is an initial step in developing a methodology to robustly estimate the refractive index of materials using passive, polarimetrically-resolved hyperspectral data. The present effort benefitted by analyzing optically smooth dielectric materials which filled hundreds of pixels and exhibiting strong spectral variations in n and κ across the instrument's measurement band. There are still several challenges and complications, some of which are discussed in the next section, that need to be addressed before this type of instrumentation and technique can be fielded against realistic targets in an operational setting.

6.1 Future Work

At various points in this document, the limitations of division-of-time polarimeters were discussed — chief among them being the potential effects of scene drift. There are two other types of commonly used polarimeters: division of aperture and division of focal plane. Division-of-aperture polarimeters split the incoming light into multiple beams and measure a different polarization state for each of the beams. This has the advantage of simultaneously collecting all polarization states while maintaining spatial resolution but at the cost of SNR. Division-of-focal-plane polarimeters limit the spatial resolution but simultaneously collect the polarization states and don't require dividing the incoming light, so SNR is maintained. While a division-of-time polarimeter was used to collect data for this work, nothing in the index of refraction fit is explicitly dependent on the Stokes vector being measured by a specific type of polarimeter. For fielded sensors, division of aperture or division of focal plane would probably outperform division of time polarimeters. It would be interesting to test this fitting routine of data collected by other types of polarimeters to test any effects this has on the fit as well as to collect some datasets which are more realistic to actual applications.

One of the chief drawbacks of this method as it is currently implemented is the amount of time it takes to fit index of refraction for a single pixel — usually on the order of 10s of seconds. This makes it impractical to apply to an entire image. One way to improve this is to incorporate GPU processing because the fitting routine is highly parallelizable. For much of this work, MATLAB's parallel processing toolbox was used to run the fit independently on each of the computers four cores. This offered almost exactly a 4x improvement in the number of pixels fit in a given t'ime period. GPUs have hundreds of cores, the only limitiation being limited RAM, but since this fit is not RAM intensive, the processing speed could be significantly

improved using GPUs. Additionally, implementing the code in C to avoid the MAT-LAB overhead could significantly improve fit speed. Even with these improvements however — because of the non-linear relationship between index of refraction and radiance — the fit will likely never be as fast as classification techniques that can be implemented with linear algebra. It would also be important to consider better ways to search the parameter space; a number of techniques were tested as part of this research — only a handful of which are discussed — but perhaps someone with a better mathematics background could find ways to improve the search algorithms and tailor them for this application. Another interesting development in recent years has been the proliferation of neural network applications in remote sensing. It may be interesting to try using neural networks to match index of refraction spectra to radiance measurements. Finally, further work could be done to improve the models used to describe index of refraction. One specific idea I had but did not implement was treating both the magnitude and the spectral location of the "knot" points used in the PCHIP model as fit parameters. Another addition would be to add out-of-band knot points a fit parameters instead of the simple linear extrapolation used for this work. It would also be good — though likely very difficult — to have a single model capable of describing the index of refraction of all materials.

Another limitation of this work is that it only dealt with smooth surfaces. Many of the targets of interest for remote sensing applications won't have smooth surfaces that are well described by a simple Fresnel reflectance model. It would also be interesting to consider the effects that surface roughness would have and how to best account for them. Implementing a pBRDF to describe the material reflectance from rough surfaces could allow the index of refraction to be fit. There are a number of complications with this that would need to be studied. The biggest difficulty with studying this is the lack of reliable truth measurements. Index of refraction is generally treated

140

as a fit parameter in BRDF models but it is not always clear whether this is actually representative of the material being examined or just a value that produces the best fit. Additionally, because strong sources are usually needed to measure off-specular reflection, lasers are used to measure BRDFs limiting most measurements to a single wavelength. Finally, to the author's knowledge, there is no single BRDF model that can describe a wide range of materials, so any study of BRDF effects may have to be limited to a specific category of materials — painted targets for example.

Along these same lines, it would be beneficial to apply this fitting to more realistic scenarios. Currently, searching for targets in a scene would be very time consuming, but perhaps with some of the improvements discussed above it would be feasible. This would allow a more "apples-to-apples" comparison with existing material identification techniques. It would also be interesting to see how potentially having estimates of scene geometry could improve classfication accuracy. Ways of accounting for sub-pixel targets would also have to be developed which may not be trivial due to the non-linear relationship between radiance and index of refraction. Finally, the fit needs to be applied to and potentially adapted for data from a wider range of more realistic materials. The materials used in this work were chosen primary because they have strong features in the LWIR and were easy to get truth measurements of index of refraction for, but it would also be interesting to consider materials with more subtle spectral features.

VII. Acknowledgments

First, I'd like to thank my advisor for his guidance and mentorship. I'd also like to thank the rest of my research committee for their input and ideas. Finally, I want to thank my family for their years of support. I wouldn't have accomplished this without all of you.

Appendix A. Index of Refraction Fit - Indoor

```matlab
function [n,kappa,Tr,Te,Parameters,fval,exitflag,output] =
    nkFit4(theta,tot_pol,S0,X,varargin)
% [n,kappa,Tr,Te] = nkFit4(theta,tot_pol,X,varargin)
%
% Fit real and imaginary components of index of refraction
%    based on the Lorentz oscillator model and assuming
%   blackbody radiance incident on the surface.
%
% --- Parameters --- {} denotes default value
% Model - oscillator model
%               'LOM' - Lorentz oscillator model
%               'PCI' - pchip interpolation
%               'BIR' - birefringence model
% nOsc  - number of oscillators to include in fit {1 if
%   LOM, 15 if PCI}
% Algorithm - type of algorithm to use for fitting
%               'fmsb'   - fminsearchbnd
%               'q-n'    - quasi-newton
%               'hybrid' - 200 iterations of fmsb then q-n
% Tr       - temperature of downwelling blackbody {300}
% Te       - surface temperature {300}
% dT       - +/- range of temperatures to allow in fitting
%    {50}
% emis     - emissivity of downwelling blackbody {1}
% S0_only  - only use S0 values in fitting {false}
% pol_only - only use tot_pol values in fitting {false}
%
% ------------------------------
% Jacob A. Martin
% Air Force Institute of Technology
% Wright-Patterson AFB, Ohio
% (517) 507-1013
% jacob.martin@afit.edu
% Version 0.16  --  07-Jul-2016
% ------------------------------

% V 0.01 11-Jun-2014 Initial version.
% V 0.02 18-Jun-2014 Updated to vectorize oscillator
%   parameters.
% V 0.03 28-Jun-2014 Updated to account for arbitrary
%   number of oscillators
```

```
% V 0.04 30-Jun-2014 Updated to account for multiple
    angles
% V 0.05 14-Jul-2014 Added option for hybrid Lorentz-
    Gaussian oscillator model
% V 0.06 18-Jul-2014 Include S0 in error function
% V 0.07 21-Jul-2014 Added e_inf term to Lorentz
    oscillator model
% V 0.08 12-Nov-2014 Added option to include S2 in error
    function
% V 0.09 17-Nov-2014 Added option to only use S0 or
    tot_pol
% V 0.10 31-Mar-2015 Added Tauc-Lorentz fitting function
% V 0.11 05-Apr-2015 Added "New Amorphous Dispersion
    Formula" function
% V 0.12 17-Apr-2015 Added option to weight error function
     by noise in S0 and tot_pol
% V 0.13 26-Jun-2015 Automate oscillator locations and
    number of oscillators based on turning points in the
    data. Number of oscillators can still be input manually
     if desired.
% V 0.14 21-Sep-2015 Automatically choose between Lorentz
    oscillator model and PCHIP interpolation based on
    sharpness of tot_pol features. Improved temperature
    bound estimates
% V 0.15 06-Jun-2016 Add birefringence fitting option
% V 0.16 07-Jul-2016 Clean up code and comment

nAng = numel(theta);
nSpc = numel(X);

% Load in optional inputs
opts = struct('nOsc',[],'Algorithm',[],'Model',[],'Tr',[],
    'Te',[], 'dT',[],'emis',1,'S0_only',0,'pol_only',0);
opts = parse_pv_pairs(opts,varargin);

nOsc     = opts.nOsc;
emis     = opts.emis;
dT       = opts.dT;
S0_only  = opts.S0_only;
pol_only = opts.pol_only;

% Ensure X is a row vector
[nRow,nCol] = size(X);
```

```matlab
if nRow > nCol;
    X = X';
end

% Ensure tot_pol is shaped [nAng,nSpc]
[nRow,~] = size(tot_pol);
if nRow ~= numel(theta);
    tot_pol = tot_pol';
end
tot_pol = double(tot_pol);

% Ensure S0 is shaped [nAng,nSpc]
[nRow,~] = size(S0);
if nRow ~= numel(theta);
    S0 = S0';
end
S0 = double(S0);

% Ensure theta and phi are column vectors
[nRow,nCol] = size(theta);
if nRow < nCol;
    theta = theta';
end

% If the model is unspecified, test how sharp the tot_pol
    features are. If
% they are above a threshold, use the Lorentz oscillator
    model, if not use
% PCHIP interpolation model
if isempty(opts.Model);
    if prctile(abs(diff(tot_pol,[],2) / (X(2) - X(1))),95)
        > 0.1;
        opts.Model = 'LOM';
    else opts.Model = 'PCI';
    end
end

% Default search methods for each model
if isempty(opts.Algorithm) && strcmp(opts.Model,'PCI');
    opts.Algorithm = 'q-n'; end
if isempty(opts.Algorithm) && strcmp(opts.Model,'LOM');
    opts.Algorithm = 'fmsb'; end
```

```matlab
if isempty(opts.Algorithm) && strcmp(opts.Model,'BIR');
    opts.Algorithm = 'fmsb'; end

% Calculate temperature limits based on S0 and S1
if isempty(opts.Tr) && isempty(opts.Te) && isempty(opts.dT
    );
    if mean(mean(mean(tot_pol))) > 0;
        Te_upper = prctile(min(brightnessTemperature(X,S0
            /1e6),[],1),5);
        Te_lower = Te_upper - 25;
        opts.Te  = mean([Te_upper Te_lower]);
        Tr_lower = prctile(max(brightnessTemperature(X,S0
            /1e6),[],1),95);
%       opts.Tr  = mean(mean(brightnessTemperature(X,1e
    -6*(2*S0) - ...
%               repmat(planckian(X,opts.Te),nAng,1))));
        opts.Tr  = Tr_lower + 25;
%       dT       = opts.Tr - Tr_lower;
%       Tr_upper = opts.Tr + 5 * dT;
        Tr_upper = Tr_lower + 50;
    elseif mean(mean(mean(tot_pol))) < 0;
        Te_lower = prctile(max(brightnessTemperature(X,S0
            /1e6),[],1),95);
        Te_upper = Te_lower + 25;
        opts.Te  = mean([Te_upper Te_lower]);
        Tr_upper = prctile(min(brightnessTemperature(X,S0
            /1e6),[],1),5);
        opts.Tr  = mean(mean(brightnessTemperature(X,1e
            -6*(2*S0) - ...
            repmat(planckian(X,opts.Te),nAng,1))));
        dT       = Tr_upper - opts.Tr;
        Tr_lower = opts.Tr - 5 * dT;
    end
elseif isempty(opts.Tr) && isempty(opts.Te)
    if mean(mean(mean(tot_pol))) > 0;
        Te_upper = prctile(min(brightnessTemperature(X,S0
            /1e6),[],1),20);
        Te_lower = Te_upper - opts.dT;
        opts.Te = mean([Te_upper Te_lower]);
        Tr_lower = prctile(max(brightnessTemperature(X,S0
            /1e6),[],1),80);
        Tr_upper = Tr_lower + opts.dT;
        opts.Tr = mean([Tr_upper Tr_lower]);
```

146

```matlab
    elseif mean(mean(mean(tot_pol))) < 0;
        Te_lower = prctile(max(brightnessTemperature(X,S0
            /1e6),[],1),80);
        Te_upper = Te_lower + opts.dT;
        opts.Te = mean([Te_upper Te_lower]);
        Tr_upper = prctile(min(brightnessTemperature(X,S0
            /1e6),[],1),20);
        Tr_lower = Tr_upper - opts.dT;
        opts.Tr = mean([Tr_upper Tr_lower]);
    end
else Te_upper = opts.Te + opts.dT; Te_lower = opts.Te -
  opts.dT;
    Tr_upper = opts.Tr + opts.dT; Tr_lower = opts.Tr -
        opts.dT;
end

% If the number of oscillators is not specified, the
  number of peaks in tot_pol
% (with a minimum prominence of 0.1 - well above the noise
  ) is used as
% the number of oscillators. If the number of oscillators
  is specified, the
% oscillator locations are set to be equally spaced
  between 700 and 1350
% wavenumbers. Otherwise, If using PCI model nOsc is
% always 15.

if isempty(nOsc) && strcmp(opts.Model,'PCI'); nOsc = 15;
  end

if isempty(nOsc)
    [pks,loc] = findpeaks(abs(mean(tot_pol,1)),X,'
        MinPeakProminence',0.1);
    nOsc = numel(pks);
    Osc_loc = loc-[200 190];
    elseif nOsc == 1; [~,tmp] = max(abs(mean(tot_pol,1)));
        Osc_loc = X(tmp) - 200;
    else Osc_loc = linspace(700,800,nOsc);
end

% Define a function for S0, total polarization in terms of
    different models. The
```

```matlab
% error function is defined as the Frobinius norm of the
   difference
% between the S0 , tot_pol data and the function values for
    these terms
% at a given point in the parameter space . By default , S0
   and total
% polarization are used in the error metric , but options
   also exist to use
% only S0 or only polarization .
switch opts.Model
    case 'LOM'
        % Lorentz oscillator model for dielectric constant
        e1 = @ (vp ,v0 ,Xi ,f ,einf ,v) einf + sum ( repmat (f ,1 ,
           nSpc ) .* ...
            ( repmat (vp ,nOsc ,nSpc ).^2 .* ( repmat (v0 ,1 ,nSpc )
               .^2 - ...
            repmat (v ,nOsc ,1 ).^2)) ./ (( repmat (v0 ,1 ,nSpc )
               .^2 - ...
            repmat (v ,nOsc ,1 ).^2).^2 + repmat (Xi ,1 ,nSpc ).^2
                .* repmat (v ,nOsc ,1 ).^2),1);

        e2 = @ (vp ,v0 ,Xi ,f ,v) sum ( repmat (f ,1 ,nSpc ) .* (
           repmat (vp ,nOsc ,nSpc ).^2 .* ...
            repmat (Xi ,1 ,nSpc ) .* repmat (v ,nOsc ,1 )) ./ ((
               repmat (v0 ,1 ,nSpc ).^2 - ...
            repmat (v ,nOsc ,1 ).^2).^2 + repmat (Xi ,1 ,nSpc ).^2
                .* repmat (v ,nOsc ,1 ).^2),1);

        % Index of refraction
        N = @ (vp ,v0 ,Xi ,f ,einf ,v) repmat ((1/ sqrt (2)) .*
           sqrt (e1 (vp ,v0 ,Xi ,f ,einf ,v) + ...
            sqrt (e1 (vp ,v0 ,Xi ,f ,einf ,v ).^2 + e2 (vp ,v0 ,Xi ,f ,
               v ).^2)),nAng ,1) + ...
            1i * repmat ((1/ sqrt (2)) .* sqrt (-e1 (vp ,v0 ,Xi ,f
               ,einf ,v) + ...
            sqrt (e1 (vp ,v0 ,Xi ,f ,einf ,v ).^2 + e2 (vp ,v0 ,Xi ,f ,
               v ).^2)),nAng ,1);

        % Fresnel
        cos_t = @ (vp ,v0 ,Xi ,f ,einf ,v ,Theta ) sqrt (1 -
           bsxfun (@times ,sin ( Theta ), ...
            1 ./ N(vp ,v0 ,Xi ,f ,einf ,v )).^2);
```

```matlab
R_s = @ (vp,v0,Xi,f,einf,v,Theta) abs(bsxfun(@
   minus,cos(Theta), ...
     bsxfun(@times,N(vp,v0,Xi,f,einf,v),cos_t(vp,v0
        ,Xi,f,einf,v,Theta))) ./ bsxfun(@plus,cos(
        Theta), ...
     bsxfun(@times,N(vp,v0,Xi,f,einf,v),cos_t(vp,v0
        ,Xi,f,einf,v,Theta)))).^2;

R_p = @ (vp,v0,Xi,f,einf,v,Theta) abs((cos_t(vp,v0
   ,Xi,f,einf,v,Theta) - ...
     bsxfun(@times,N(vp,v0,Xi,f,einf,v),cos(Theta))
        ) ./ ...
     (cos_t(vp,v0,Xi,f,einf,v,Theta) + bsxfun(@
        times,N(vp,v0,Xi,f,einf,v), ...
     cos(Theta)))).^2;

R = @ (vp,v0,Xi,f,einf,v,Theta) (R_s(vp,v0,Xi,f,
   einf,v,Theta) + R_p(vp,v0,Xi,f,einf,v,Theta)) /
    2;

% Theoretical S0
S0_calc = @(vp,v0,Xi,f,einf,Tr,Te,v) R(vp,v0,Xi,f,
   einf,v,theta) .* ...
     repmat(emis*planckian(v,Tr),nAng,1) * 1e6 + (1
         - R(vp,v0,Xi,f,einf,v,theta)) .* ...
     repmat(planckian(v,Te),nAng,1) * 1e6;

% Theoretical total polarization
tot_pol_calc = @(vp,v0,Xi,f,einf,Tr,Te,v) (R_s(vp,
   v0,Xi,f,einf,v,theta) - R_p(vp,v0,Xi,f,einf,v,
   theta)) ...
     .* repmat((emis*planckian(v,Tr) - planckian(v,
        Te)),nAng,1) * 0.5e6;

% Define error function
if S0_only
     error = @(x) norm(S0-S0_calc(x(3*nOsc+1),x(1:
        nOsc),x(nOsc+1:2*nOsc),x(2*nOsc+1:3*nOsc),
        ...
        x(3*nOsc+2),x(3*nOsc+3),x(3*nOsc+4),X),'
           fro');
elseif pol_only
```

```matlab
            error = @(x) norm(tot_pol-tot_pol_calc(x(3*
                nOsc+1),x(1:nOsc),x(nOsc+1:2*nOsc),x(2*nOsc
                +1:3*nOsc),...
                  x(3*nOsc+2),x(3*nOsc+3),x(3*nOsc+4),X),'
                      fro');
        else
            error = @(x) norm(tot_pol-tot_pol_calc(x(3*
                nOsc+1),x(1:nOsc),x(nOsc+1:2*nOsc),x(2*nOsc
                +1:3*nOsc),...
                  x(3*nOsc+2),x(3*nOsc+3),x(3*nOsc+4),X),'
                      fro') + ...
                  norm(S0-S0_calc(x(3*nOsc+1),x(1:nOsc),x(
                      nOsc+1:2*nOsc),x(2*nOsc+1:3*nOsc),...
                  x(3*nOsc+2),x(3*nOsc+3),x(3*nOsc+4),X),'
                      fro');
        end

        % Initial guess for algorithm and bounds
        % x = [v0 ; Xi ; f ; vp ; einf ; Tr ; Te]
        % If nOsc = 1, f can be forced to one
        if nOsc == 1;
            x_init  = [Osc_loc'               ; 10*ones(nOsc,1)
                    ; ones(nOsc,1) ; 1250 ; 5 ; opts.Tr  ;
                opts.Te];
            x_lower = [600*ones(nOsc,1)  ; zeros(nOsc,1)
                    ; ones(nOsc,1)    ; 0    ; 0 ;
                Tr_lower ; Te_lower];
            x_upper = [1250*ones(nOsc,1) ; 30*ones(nOsc,1)
                    ; ones(nOsc,1)      ; 20000; 10; Tr_upper
                ; Te_upper];
        else
            x_init  = [1000*ones(nOsc,1) ; ones(nOsc,1)  ;
                0.5*ones(nOsc,1)  ; 1400 ; 6.7 ; opts.Tr
                ; opts.Te];
            x_lower = [600*ones(nOsc,1) ; zeros(nOsc,1) ;
                zeros(nOsc,1)    ; 1000    ; 0 ; Tr_lower ;
                 Te_lower];
            x_upper = [1500*ones(nOsc,1) ; 30 * ones(nOsc
                ,1)   ; ones(nOsc,1) ; 2000; 10; Tr_upper ;
                Te_upper];
        end
    case 'PCI'
        % Knot point spacing
```

```matlab
tmp = linspace(X(1),X(end),nOsc);
del_xx = tmp(2)-tmp(1);

% Number of out-of-band extrapolation points
nOut = 5;

% Knot point locations
xx = [linspace(X(1)-nOut*del_xx,X(1)-del_xx,nOut)
    ...
    linspace(X(1),X(end),nOsc) linspace(X(end)+
        del_xx,X(end)+nOut*del_xx,nOut)];

% Kappa at each knot point and extrapolate out of
    band
K_tmp = @(yy) max(interp1(tmp,yy,xx,'linear','
    extrap'),0);

% Apply the hilbert transform to kappa to solve
    for n
N_tmp = @(yy,a) -imag(hilbert(K_tmp(yy))) + a;

% Interpolate n and kappa back onto instrument
    spectral axis
K = @(yy) interp1(tmp,max(yy,0),X,'pchip');
N_tmp = @(yy,a) interp1(xx,N_tmp(yy,a),X,'pchip');

% Index of refraction
N = @(yy,a) N_tmp(yy,a) + 1i * K(yy);

% Fresnel
cos_t = @ (yy,a,Theta) sqrt(1 - bsxfun(@times,sin(
    Theta), ...
    1 ./ N(yy,a)).^2);

R_s = @ (yy,a,Theta) abs(bsxfun(@minus,cos(Theta),
    ...
    bsxfun(@times,N(yy,a),cos_t(yy,a,Theta))) ./
        bsxfun(@plus,cos(Theta), ...
    bsxfun(@times,N(yy,a),cos_t(yy,a,Theta)))).^2;

R_p = @ (yy,a,Theta) abs((cos_t(yy,a,Theta) - ...
    repmat(N(yy,a),nAng,1) .* repmat(cos(Theta),1,
        nSpc)) ./ ...
```

```matlab
        (cos_t(yy,a,Theta) + repmat(N(yy,a),nAng,1) .*
            ...
        repmat(cos(Theta),1,nSpc))).^2;

R = @ (yy,a,Theta) (R_s(yy,a,Theta) + R_p(yy,a,
    Theta)) / 2;

% Theoretical S0
S0_calc = @ (yy,a,Tr,Te,v) R(yy,a,theta) .* ...
    repmat(emis*planckian(v,Tr),nAng,1) * 1e6 + (1
        - R(yy,a,theta)) .* ...
    repmat(planckian(v,Te),nAng,1) * 1e6;

% Theoretical tot_pol
tot_pol_calc = @ (yy,a,Tr,Te,v) (R_s(yy,a,theta) -
    ...
    R_p(yy,a,theta)) .* repmat((emis*planckian(v,
        Tr) - ...
    planckian(v,Te)),nAng,1) * 0.5e6;

if dT == 0;
    % Define error function
    if S0_only
        error = @(x) norm(S0-S0_calc(x(1:nOsc),x(
            nOsc+1),opts.Tr,opts.Te,X),'fro');
    elseif pol_only
        error = @(x) norm(tot_pol-tot_pol_calc(x
            (1:nOsc),x(nOsc+1),opts.Tr,opts.Te,X),'
            fro');
    else
        error = @(x) norm(tot_pol-tot_pol_calc(x
            (1:nOsc),x(nOsc+1),opts.Tr,opts.Te,X),'
            fro') + ...
            norm(S0-S0_calc(x(1:nOsc),x(nOsc+1),
                opts.Tr,opts.Te,X),'fro');
    end

    % Initial guess for algorithm and bounds
    % x = [yy ; a ; Tr ; Te]
    x_init  = [ones(nOsc,1)    ; 1.4639];
    x_lower = [zeros(nOsc,1)   ; 1];
    x_upper = [10*ones(nOsc,1) ; 1.5];
else
```

```matlab
            % Define error function
            if S0_only
                error = @(x) norm(S0-S0_calc(x(1:nOsc),x(
                    nOsc+1),x(nOsc+2),x(nOsc+3),X),'fro');
            elseif pol_only
                error = @(x) norm(tot_pol-tot_pol_calc(x
                    (1:nOsc),x(nOsc+1),x(nOsc+2),x(nOsc+3),
                    X),'fro');
            else
                error = @(x) norm(tot_pol-tot_pol_calc(x
                    (1:nOsc),x(nOsc+1),x(nOsc+2),x(nOsc+3),
                    X),'fro') + ...
                      norm(S0-S0_calc(x(1:nOsc),x(nOsc+1),x(
                          nOsc+2),x(nOsc+3),X),'fro');
            end

            % Initial guess for algorithm and bounds
            % x = [yy ; a ; Tr ; Te]
            x_init  = [ones(nOsc,1)     ; 1.4639 ; opts.Tr
                ; opts.Te];
            x_lower = [zeros(nOsc,1)    ; 1 ; Tr_lower ;
                Te_lower];
            x_upper = [10*ones(nOsc,1) ; 1.5 ; Tr_upper ;
                Te_upper ];
    end
case 'BIR'
    % Lorentz oscillator model for dielectric constant
    e1 = @ (vp,v0,Xi,f,einf,v) einf + sum(repmat(f,1,
        nSpc) .* ...
        (repmat(vp,nOsc,nSpc).^2 .* (repmat(v0,1,nSpc)
            .^2 - ...
        repmat(v,nOsc,1).^2)) ./ ((repmat(v0,1,nSpc)
            .^2 - ...
        repmat(v,nOsc,1).^2).^2 + repmat(Xi,1,nSpc).^2
            .* repmat(v,nOsc,1).^2),1);

    e2 = @ (vp,v0,Xi,f,v) sum(repmat(f,1,nSpc) .* (
        repmat(vp,nOsc,nSpc).^2 .* ...
        repmat(Xi,1,nSpc) .* repmat(v,nOsc,1)) ./ ((
            repmat(v0,1,nSpc).^2 - ...
        repmat(v,nOsc,1).^2).^2 + repmat(Xi,1,nSpc).^2
            .* repmat(v,nOsc,1).^2),1);
```

```matlab
% Index of refraction
N = @ (vp,v0,Xi,f,einf,v) repmat((1/sqrt(2)) .*
    sqrt(e1(vp,v0,Xi,f,einf,v) + ...
      sqrt(e1(vp,v0,Xi,f,einf,v).^2 + e2(vp,v0,Xi,f,
        v).^2)),nAng,1) + ...
      1i * repmat((1/sqrt(2)) .* sqrt(-e1(vp,v0,Xi,f
        ,einf,v) + ...
      sqrt(e1(vp,v0,Xi,f,einf,v).^2 + e2(vp,v0,Xi,f,
        v).^2)),nAng,1);

% Fresnel
cos_t = @ (vp,v0,Xi,f,einf,v,Theta) sqrt(1 -
    bsxfun(@times,sin(Theta), ...
      1 ./ N(vp,v0,Xi,f,einf,v)).^2);

R_s = @ (vp_s,v0_s,Xi_s,f_s,einf_s,v,Theta) abs(
    bsxfun(@minus,cos(Theta), ...
      bsxfun(@times,N(vp_s,v0_s,Xi_s,f_s,einf_s,v),
        cos_t(vp_s,v0_s,Xi_s,f_s,einf_s,v,Theta)))
        ./ bsxfun(@plus,cos(Theta), ...
      bsxfun(@times,N(vp_s,v0_s,Xi_s,f_s,einf_s,v),
        cos_t(vp_s,v0_s,Xi_s,f_s,einf_s,v,Theta))))
        .^2;

R_p = @ (vp_p,v0_p,Xi_p,f_p,einf_p,v,Theta) abs((
    cos_t(vp_p,v0_p,Xi_p,f_p,einf_p,v,Theta) - ...
      bsxfun(@times,N(vp_p,v0_p,Xi_p,f_p,einf_p,v),
        cos(Theta))) ./ ...
      (cos_t(vp_p,v0_p,Xi_p,f_p,einf_p,v,Theta) +
        bsxfun(@times,N(vp_p,v0_p,Xi_p,f_p,einf_p,v
        ), ...
      cos(Theta)))).^2;

R = @ (vp_s,v0_s,Xi_s,f_s,einf_s,vp_p,v0_p,Xi_p,
    f_p,einf_p,v,Theta) (R_s(vp_s,v0_s,Xi_s,f_s,
    einf_s,v,Theta) + ...
      R_p(vp_p,v0_p,Xi_p,f_p,einf_p,v,Theta)) / 2;

% Theoretical S0
S0_calc = @(vp_s,v0_s,Xi_s,f_s,einf_s,vp_p,v0_p,
    Xi_p,f_p,einf_p,Tr,Te,v) ...
      R(vp_s,v0_s,Xi_s,f_s,einf_s,vp_p,v0_p,Xi_p,f_p
        ,einf_p,v,theta) .* ...
```

```matlab
        repmat(emis*planckian(v,Tr),nAng,1) * 1e6 + ...
        (1 - R(vp_s,v0_s,Xi_s,f_s,einf_s,vp_p,v0_p,
            Xi_p,f_p,einf_p,v,theta)) .* repmat(
            planckian(v,Te),nAng,1) * 1e6;

% Theoretical total polarization
tot_pol_calc = @(vp_s,v0_s,Xi_s,f_s,einf_s,vp_p,
    v0_p,Xi_p,f_p,einf_p,Tr,Te,v) ...
        (R_s(vp_s,v0_s,Xi_s,f_s,einf_s,v,theta) - R_p(
            vp_p,v0_p,Xi_p,f_p,einf_p,v,theta)) ...
        .* (repmat(emis*planckian(v,Tr),nAng,1) * 0.5
            e6 - ...
        repmat(planckian(v,Te),nAng,1) * 0.5e6);

% Define error function
if S0_only
    error = @(x) norm(S0-S0_calc(x(3*nOsc+1),x(1:
        nOsc),x(nOsc+1:2*nOsc),x(2*nOsc+1:3*nOsc),x
        (3*nOsc+2),x(6*nOsc+3),x(3*nOsc+3:4*nOsc+2)
        ,x(4*nOsc+3:5*nOsc+2),...
         x(5*nOsc+3:6*nOsc+2),x(6*nOsc+4),x(6*nOsc
            +5),x(6*nOsc+6),X),'fro');
elseif pol_only
    error = @(x) norm(tot_pol-tot_pol_calc(x(4),x
        (1),x(2),x(3),x(5),x(9),x(6),x(7),...
         x(8),x(10),x(11),x(12),X),'fro');
else
    error = @(x) norm(tot_pol-tot_pol_calc(x(3*
        nOsc+1),x(1:nOsc),x(nOsc+1:2*nOsc),x(2*nOsc
        +1:3*nOsc),x(3*nOsc+2),x(6*nOsc+3),x(3*nOsc
        +3:4*nOsc+2),x(4*nOsc+3:5*nOsc+2),...
         x(5*nOsc+3:6*nOsc+2),x(6*nOsc+4),x(6*nOsc
            +5),x(6*nOsc+6),X),'fro') + ...
         norm(S0-S0_calc(x(3*nOsc+1),x(1:nOsc),x(
            nOsc+1:2*nOsc),x(2*nOsc+1:3*nOsc),x(3*
            nOsc+2),x(6*nOsc+3),x(3*nOsc+3:4*nOsc
            +2),x(4*nOsc+3:5*nOsc+2),...
         x(5*nOsc+3:6*nOsc+2),x(6*nOsc+4),x(6*nOsc
            +5),x(6*nOsc+6),X),'fro');
end

% Initial guess for algorithm and bounds
```

```matlab
        % x = [v0_s ; Xi_s ; f_s ; vp_s ; einf_s ; v0_p ;
           Xi_p ; f_p ;
        %       vp_p ; einf_p ; Tr ; Te]
        if nOsc == 1;
            x_init  = [500 ; 14 ; 1 ; 1250 ; 3 ; 500 ; 18
               ; 1 ; 1350 ; 3 ; opts.Tr  ; opts.Te];
            x_lower = [300 ; 10 ; 1 ; 1000 ; 0 ; 300 ; 10
               ; 1 ; 1000 ; 0 ; Tr_lower ; Te_lower];
            x_upper = [800 ; 20 ; 1 ; 4000 ; 5 ; 800 ; 20
               ; 1 ; 4000 ; 5 ; Tr_upper ; Te_upper];
        else
            x_init  = [linspace(500,700,nOsc)' ; 14*ones(
               nOsc,1) ; ones(nOsc,1)  ; ...
                 1250 ; 3 ; linspace(500,700,nOsc)' ; 18*
                    ones(nOsc,1) ; ones(nOsc,1) ; ...
                 1350 ; 3 ; opts.Tr  ; opts.Te];
            x_lower = [300*ones(nOsc,1)        ; 10*ones(
               nOsc,1) ; zeros(nOsc,1) ; ...
                 1000 ; 0 ; 300*ones(nOsc,1) ; 10*ones(nOsc
                    ,1) ; zeros(nOsc,1) ; ...
                 1000 ; 0 ; Tr_lower ; Te_lower];
            x_upper = [800*ones(nOsc,1)        ; 20*ones(
               nOsc,1) ; ones(nOsc,1)  ; ...
                 4000 ; 5 ; 800*ones(nOsc,1) ; 20*ones(nOsc
                    ,1) ; ones(nOsc,1) ; ...
                 4000 ; 5 ; Tr_upper ; Te_upper];
        end
end

% Implement algorithm of choice to search the parameter
   space. By default
% the bounded fminsearch is used.
switch opts.Algorithm
    case 'fmsb'
        [x_meas,fval,exitflag,output] = fminsearchbnd(
           error,x_init,x_lower,x_upper,...
            optimset('MaxFunEvals',1e15,'MaxIter',1.5e4,'
               PlotFcns',@optimplotfval));
    case 'q-n'
        fitopts = optimoptions('fminunc','Algorithm','
           quasi-newton',...
            'MaxFunEvals',1e15,'PlotFcns',@optimplotfval);
```

```matlab
        [x_meas,fval,~,~,~] = fminunc(error,x_init,fitopts
            );
    case 'hybrid'
        [x_meas,~,exitflag,output] = fminsearchbnd(error,
            x_init,x_lower,x_upper,...
            optimset('MaxFunEvals',1e15,'MaxIter',200,'
                PlotFcns',@optimplotfval));

        fitopts = optimoptions('fminunc','Algorithm','
            quasi-newton',...
            'MaxFunEvals',1e15,'PlotFcns',@optimplotfval);
        [x_meas,fval,~,~,~] = fminunc(error,x_meas,fitopts
            );
end

% Parse out oscillator parameters
switch opts.Model
    case 'LOM'
        Parameters.vp   = x_meas(3*nOsc+1);
        Parameters.v0   = x_meas(1:nOsc);
        Parameters.Xi   = x_meas(nOsc+1:2*nOsc);
        Parameters.f    = x_meas(2*nOsc+1:3*nOsc);
        Parameters.einf = x_meas(3*nOsc+2);
        Tr   = x_meas(3*nOsc+3);
        Te   = x_meas(3*nOsc+4);
        Parameters.TrLim   = [Tr_lower Tr_upper];
        Parameters.TeLim   = [Te_lower Te_upper];

        % Predicted n and kappa
        n      = real(mean(N(Parameters.vp,Parameters.v0,
            Parameters.Xi,Parameters.f,Parameters.einf,X)
            ,1));
        kappa = imag(mean(N(Parameters.vp,Parameters.v0,
            Parameters.Xi,Parameters.f,Parameters.einf,X)
            ,1));
    case 'PCI'
        if dT == 0;
            Parameters.yy    = x_meas(1:nOsc);
            Parameters.a     = x_meas(nOsc+1);
            Tr               = opts.Tr;
            Te               = opts.Te;
        else
            Parameters.yy    = x_meas(1:nOsc);
```

157

```matlab
            Parameters.a    = x_meas(nOsc+1);
            Tr              = x_meas(nOsc+2);
            Te              = x_meas(nOsc+3);
            Parameters.TrLim = [Tr_lower Tr_upper];
            Parameters.TeLim = [Te_lower Te_upper];
        end

        % Predicted n and kappa
        n    = mean(real(N(Parameters.yy,Parameters.a))
            ,1);
        kappa = mean(K(Parameters.yy),1);
    case 'BIR'
        Parameters.v0_s   = x_meas(1:nOsc);
        Parameters.Xi_s   = x_meas(nOsc+1:2*nOsc);
        Parameters.f_s    = x_meas(2*nOsc+1:3*nOsc);
        Parameters.vp_s   = x_meas(3*nOsc+1);
        Parameters.einf_s = x_meas(3*nOsc+2);
        Parameters.v0_p   = x_meas(3*nOsc+3:4*nOsc+2);
        Parameters.Xi_p   = x_meas(4*nOsc+3:5*nOsc+2);
        Parameters.f_p    = x_meas(5*nOsc+3:6*nOsc+2);
        Parameters.vp_p   = x_meas(6*nOsc+3);
        Parameters.einf_p = x_meas(6*nOsc+4);
        Tr                = x_meas(6*nOsc+5);
        Te                = x_meas(6*nOsc+6);

        % Predicted n and kappa for each polarization
            state
        Parameters.n_1 = real(mean(N(Parameters.vp_s,
            Parameters.v0_s,Parameters.Xi_s,Parameters.f_s,
            Parameters.einf_s,X),1));
        Parameters.n_2 = real(mean(N(Parameters.vp_p,
            Parameters.v0_p,Parameters.Xi_p,Parameters.f_p,
            Parameters.einf_p,X),1));

        Parameters.k_1 = imag(mean(N(Parameters.vp_s,
            Parameters.v0_s,Parameters.Xi_s,Parameters.f_s,
            Parameters.einf_s,X),1));
        Parameters.k_2 = imag(mean(N(Parameters.vp_p,
            Parameters.v0_p,Parameters.Xi_p,Parameters.f_p,
            Parameters.einf_p,X),1));

        % Predicted n and kappa
        n = (Parameters.n_1 + Parameters.n_2) / 2;
```

```matlab
        kappa = (Parameters.k_1 + Parameters.k_2) / 2;
end

disp(['Objective Function Value = ' num2str(fval)]);
```

Appendix B. Index of Refraction Fit - Outdoor

```matlab
function [n,kappa,Ld,Te,Parameters,fval,exitflag,output] =
    nkFit5(theta,tot_pol,S0,X,varargin)
% [n,kappa,Ld,Te] = nkFit5(theta,tot_pol,X,varargin)
%
% Fit real and imaginary components of index of refraction
%    as well as object temperature and atmospheric
%   downwelling radiance.
%
% --- Parameters --- {} denotes default value
% Model - oscillator model
%              'LOM'  - Lorentz oscillator model (default)
%              'PCI'  - pchip interpolation
%              'BIR' - birefringence model
% nOsc  - number of oscillators to include in fit {1 if
%   LOM, 15 if PCI}
% Algorithm - type of algorithm to use for fitting
%               'fmsb' - fminsearchbnd (default)
%               'q-n'  - quasi-newton
%               'hybrid' - 200 iterations of fmsb then q-n
% Te       - surface temperature {300}
% dT       - +/- range of temperatures to allow in fitting
%     {[]}
% S0_only  - only use S0 values in fitting {false}
% pol_only - only use tot_pol values in fitting {false}
% atm_path - file path of atmospheres to load ('/Users/
%   martinja/Desktop/Atmospheres')
% Ld       - fixed downwelling radiance {[]}
% adj      - adjacency effects {false}
%
% --------------------------------
% Jacob A. Martin
% Air Force Institute of Technology
% Wright-Patterson AFB, Ohio
% (517) 507-1013
% jacob.martin@afit.edu
% Version 0.04  --  07-Jul-2016
% --------------------------------

% V 0.01 22-Feb-2016 Initial version (modified from nkFit4
    .m)
```

```matlab
% V 0.02 01-Mar-2016 Added option to manually input
   downwelling
% V 0.03 20-Jun-2016 Added option for adjacency effect
% V 0.04 07-Jul-2016 Code cleanup and comment

nAng = numel(theta);
nSpc = numel(X);

% Load in optional inputs
opts = struct('nOsc',[],'Algorithm',[],'Model','LOM','Te'
   ,[],'dT',[],'Ld',[], 'S0_only',0,'pol_only',0,'atm_path
   ','/Users/martinja/Desktop/Atmospheres/','adj',0);
opts = parse_pv_pairs(opts,varargin);


nOsc     = opts.nOsc;
dT       = opts.dT;
S0_only  = opts.S0_only;
pol_only = opts.pol_only;
atm_path = opts.atm_path;

% Ensure X is a row vector
[nRow,nCol] = size(X);
if nRow > nCol;
    X = X';
end

% Ensure tot_pol is shaped [nAng,nSpc]
[nRow,~] = size(tot_pol);
if nRow ~= numel(theta);
    tot_pol = tot_pol';
end
tot_pol = double(tot_pol);

% Ensure S0 is shaped [nAng,nSpc]
[nRow,~] = size(S0);
if nRow ~= numel(theta);
    S0 = S0';
end
S0 = double(S0);

% Ensure input Ld is shaped [nAng,nSpc]
if ~isempty(opts.Ld);
[nRow,~] = size(opts.Ld);
```

```matlab
if nRow ~= numel(theta);
    opts.Ld = opts.Ld';
end
opts.Ld = double(opts.Ld);
end

% Ensure theta is a column vector
[nRow,nCol] = size(theta);
if nRow < nCol;
    theta = theta';
end

% Default search algorithms based on model
if isempty(opts.Algorithm) && strcmp(opts.Model,'PCI');
    opts.Algorithm = 'q-n'; end
if isempty(opts.Algorithm) && strcmp(opts.Model,'LOM');
    opts.Algorithm = 'fmsb'; end
if isempty(opts.Algorithm) && strcmp(opts.Model,'BIR');
    opts.Algorithm = 'fmsb'; end

% Set object temperature limits
if isempty(opts.Te)
    Te_lower = prctile(max(brightnessTemperature(X,S0/1e6)
        ,[],2),95);
    Te_upper = Te_lower + 25;
    opts.Te  = mean([Te_upper Te_lower]);
else
    Te_lower = opts.Te - dT;
    Te_upper = opts.Te + dT;
end

% If the number of oscillators is not specified, the
  number of peaks in tot_pol
% (that are at least 50 wavenumbers separated from another
   peak) is used as
% the number of oscillators. The location of these peaks
  are used as the
% initial estimate of the oscillator centers. Two
  additional oscillators
% are added approximately 100 wavenumbers outside the band
   response of the
% Telops sensor. If the number of oscillators is specified
   , the oscillator
```

```matlab
% locations are set to be equally spaced between 700 and
    1350 wavenumbers.

if isempty(nOsc) && strcmp(opts.Model,'PCI'); nOsc = 15;
    end

if isempty(nOsc)
    [pks,loc] = findpeaks(abs(mean(tot_pol,1)),X,'
        MinPeakProminence',0.1);
    nOsc = numel(pks);
    Osc_loc = loc-[200 190];
    elseif nOsc == 1; [~,tmp] = max(abs(mean(tot_pol,1)));
        Osc_loc = X(tmp) - 200;
    elseif nOsc == 2;
        Osc_loc = [700 800];
    else Osc_loc = linspace(700,1350,nOsc);
end

% Load in atmospheres. The angle here is the angle of the
    downwelling ray
% w.r.t zenith. At this point angles and spectral
    resolution have to be
% manually set.
if isempty(opts.Ld);
    wn = 1;
    ang = [20 20 60]*pi/180;
    down = zeros(numel(theta),20,5,20,20,numel(X));
    for ii = 1:numel(theta);
        tmp = load([atm_path num2str(wn) 'wn' num2str(ang(
            ii)*180/pi) 'Deg']);
        down(ii,:,:,:,:,:) = tmp.down;
    end
else down = opts.Ld;
end

% Define a function for S0, total polarization in terms of
    different models. The
% error function is also defined as the Frobinius norm of
    the difference
% between the S0, tot_pol data and the function values for
    these terms
% at a given position in the parameter space. By default,
    S0 and total
```

```matlab
% polarization are used in the error metric, but options
   also exist to use
% only S0 or only polarization.
switch opts.Model
    case 'LOM'
        % Lorentz oscillator model for dielectric constant
        e1 = @ (vp,v0,Xi,f,einf,v) einf + sum(repmat(f,1,
           nSpc) .* ...
             (repmat(vp,nOsc,nSpc).^2 .* (repmat(v0,1,nSpc)
                .^2 - ...
             repmat(v,nOsc,1).^2)) ./ ((repmat(v0,1,nSpc)
                .^2 - ...
             repmat(v,nOsc,1).^2).^2 + repmat(Xi,1,nSpc).^2
                .* repmat(v,nOsc,1).^2),1);

        e2 = @ (vp,v0,Xi,f,v) sum(repmat(f,1,nSpc) .* (
           repmat(vp,nOsc,nSpc).^2 .* ...
             repmat(Xi,1,nSpc) .* repmat(v,nOsc,1)) ./ ((
                repmat(v0,1,nSpc).^2 - ...
             repmat(v,nOsc,1).^2).^2 + repmat(Xi,1,nSpc).^2
                .* repmat(v,nOsc,1).^2),1);

        % Index of refraction
        N = @ (vp,v0,Xi,f,einf,v) repmat((1/sqrt(2)) .*
           sqrt(e1(vp,v0,Xi,f,einf,v) + ...
             sqrt(e1(vp,v0,Xi,f,einf,v).^2 + e2(vp,v0,Xi,f,
                v).^2)),nAng,1) + ...
             1i * repmat((1/sqrt(2)) .* sqrt(-e1(vp,v0,Xi,f
                ,einf,v) + ...
             sqrt(e1(vp,v0,Xi,f,einf,v).^2 + e2(vp,v0,Xi,f,
                v).^2)),nAng,1);

        % Fresnel
        cos_t = @ (vp,v0,Xi,f,einf,v,Theta) sqrt(1 -
           bsxfun(@times,sin(Theta), ...
             1 ./ N(vp,v0,Xi,f,einf,v)).^2);

        R_s = @ (vp,v0,Xi,f,einf,v,Theta) abs(bsxfun(@
           minus,cos(Theta), ...
             bsxfun(@times,N(vp,v0,Xi,f,einf,v),cos_t(vp,v0
                ,Xi,f,einf,v,Theta))) ./ bsxfun(@plus,cos(
                Theta), ...
```

```matlab
        bsxfun(@times,N(vp,v0,Xi,f,einf,v),cos_t(vp,v0
            ,Xi,f,einf,v,Theta)))).^2;

R_p = @ (vp,v0,Xi,f,einf,v,Theta) abs((cos_t(vp,v0
    ,Xi,f,einf,v,Theta) - ...
        bsxfun(@times,N(vp,v0,Xi,f,einf,v),cos(Theta))
            ) ./ ...
        (cos_t(vp,v0,Xi,f,einf,v,Theta) + bsxfun(@
            times,N(vp,v0,Xi,f,einf,v), ...
        cos(Theta)))).^2;

R = @ (vp,v0,Xi,f,einf,v,Theta) (R_s(vp,v0,Xi,f,
    einf,v,Theta) + R_p(vp,v0,Xi,f,einf,v,Theta)) /
    2;

if isempty(opts.Ld);
    % Theoretical S0
    S0_calc = @(v0,Xi,f,vp,einf,Tg,Tl,H2O,O3,Te,v)
        R(vp,v0,Xi,f,einf,v,theta) .* ...
            squeeze(down(:,round(Tg),round(Tl),round(
                H2O),round(O3),:)) + ...
            (1 - R(vp,v0,Xi,f,einf,v,theta)) .* repmat
                (planckian(v,Te),nAng,1) * 1e6;

    % Theoretical total polarization
    tot_pol_calc = @(v0,Xi,f,vp,einf,Tg,Tl,H2O,O3,
        Te,v) (R_s(vp,v0,Xi,f,einf,v,theta) - R_p(
        vp,v0,Xi,f,einf,v,theta)) ...
            .* (0.5 .* squeeze(down(:,round(Tg),round(
                Tl),round(H2O),round(O3),:)) - ...
            repmat(planckian(v,Te),nAng,1) * 0.5e6);
else
    % Theoretical S0
    S0_calc = @(v0,Xi,f,vp,einf,Tg,Tl,H2O,O3,Te,v)
        R(vp,v0,Xi,f,einf,v,theta) .* ...
            down + (1 - R(vp,v0,Xi,f,einf,v,theta)) .*
                repmat(planckian(v,Te),nAng,1) * 1e6;

    % Theoretical total polarization
    tot_pol_calc = @(v0,Xi,f,vp,einf,Tg,Tl,H2O,O3,
        Te,v) (R_s(vp,v0,Xi,f,einf,v,theta) - R_p(
        vp,v0,Xi,f,einf,v,theta)) ...
```

```matlab
                .* (0.5 .* down - repmat ( planckian (v ,Te),
                    nAng ,1) * 0.5 e6 );
    end

    % Define error function
    if S0_only
        error = @(x) norm (S0 - S0_calc (x (1: nOsc ),x( nOsc
            +1:2* nOsc ),x (2* nOsc +1:3* nOsc ) ,...
            x (3* nOsc +1) ,x (3* nOsc +2) ,x (3* nOsc +3) ,x (3*
                nOsc +4) ,x (3* nOsc +5) ,...
            x (3* nOsc +6) ,x (3* nOsc +7) ,X) ,'fro ');
    elseif pol_only
        error = @(x) norm ( tot_pol - tot_pol_calc (x (1:
            nOsc ),x( nOsc +1:2* nOsc ),x (2* nOsc +1:3* nOsc ),
            ...
            x (3* nOsc +1) ,x (3* nOsc +2) ,x (3* nOsc +3) ,x (3*
                nOsc +4) ,x (3* nOsc +5) ,...
            x (3* nOsc +6) ,x (3* nOsc +7) ,X) ,'fro ');
    else
        error = @(x) norm ( tot_pol - tot_pol_calc (x (1:
            nOsc ),x( nOsc +1:2* nOsc ),x (2* nOsc +1:3* nOsc ),
            ...
            x (3* nOsc +1) ,x (3* nOsc +2) ,x (3* nOsc +3) ,x (3*
                nOsc +4) ,x (3* nOsc +5) ,...
            x (3* nOsc +6) ,x (3* nOsc +7) ,X) ,'fro ') + ...
            norm (S0 - S0_calc (x (1: nOsc ),x( nOsc +1:2* nOsc )
                ,x (2* nOsc +1:3* nOsc ) ,...
            x (3* nOsc +1) ,x (3* nOsc +2) ,x (3* nOsc +3) ,x (3*
                nOsc +4) ,x (3* nOsc +5) ,...
            x (3* nOsc +6) ,x (3* nOsc +7) ,X) ,'fro ');
    end

    % Initial guess for algorithm and bounds
    % x = [v0 ; Xi ; f ; vp ; einf ; Tg ; Tl ; H2O ;
        O3 ; Te]
    % If nOsc = 1, f can be forced to one
    if nOsc == 1;
        x_init  = [Osc_loc '      ; 10* ones ( nOsc ,1) ;
            ones ( nOsc ,1) ; ...
                1250 ; 5   ; 10 ; 4 ; 10 ; 10 ; opts .Te];
        x_lower = [Osc_loc '-200 ; zeros ( nOsc ,1)    ;
            ones ( nOsc ,1) ; ...
                1000     ; 0  ; 1 ; 1 ; 1 ; 1 ; Te_lower ];
```

```matlab
        x_upper = [Osc_loc'+200 ; 20*ones(nOsc,1) ;
            ones(nOsc,1) ; ...
              20000; 10 ; 20 ; 5 ; 20 ; 20 ; Te_upper];
    else
        x_init  = [Osc_loc'      ; ones(nOsc,1)       ;
            0.5*ones(nOsc,1) ; ...
              1400 ; 6.7 ; 10 ; 4 ; 10 ; 10 ; opts.Te];
        x_lower = [Osc_loc'-200 ; zeros(nOsc,1)      ;
            zeros(nOsc,1)    ; ...
              1000 ; 5   ; 1  ; 1 ; 1  ; 1  ; Te_lower];
        x_upper = [Osc_loc'+200 ; 30 * ones(nOsc,1) ;
            ones(nOsc,1)     ; ...
              2000 ; 10  ; 20 ; 5 ; 20 ; 20 ; Te_upper];
    end

    % Adjacency effects
    if opts.adj == 1;
        S0_calc = @(v0,Xi,f,vp,einf,Te,adj,Tr,v) ...
            (1 - adj) .* R(vp,v0,Xi,f,einf,v,theta) .*
                down + ...
            adj .* R(vp,v0,Xi,f,einf,v,theta) .*
                repmat(planckian(v,Tr),nAng,1) * 1e6 +
                ...
            (1 - R(vp,v0,Xi,f,einf,v,theta)) .* repmat
                (planckian(v,Te),nAng,1) * 1e6;

        tot_pol_calc = @(v0,Xi,f,vp,einf,Te,adj,Tr,v)
            (R_s(vp,v0,Xi,f,einf,v,theta) - R_p(vp,v0,
            Xi,f,einf,v,theta)) ...
            .* (0.5 .* ((1-adj) .* down + adj .*
                repmat(planckian(v,Tr),nAng,1) * 1e6) -
                ...
            repmat(planckian(v,Te),nAng,1) * 0.5e6);

        error = @(x) norm(tot_pol-tot_pol_calc(x(1:
            nOsc),x(nOsc+1:2*nOsc),x(2*nOsc+1:3*nOsc),
            ...
            x(3*nOsc+1),x(3*nOsc+2),x(3*nOsc+3),x(3*
                nOsc+4),x(3*nOsc+5),X),'fro') + ...
            norm(S0-S0_calc(x(1:nOsc),x(nOsc+1:2*nOsc)
                ,x(2*nOsc+1:3*nOsc),...
            x(3*nOsc+1),x(3*nOsc+2),x(3*nOsc+3),x(3*
                nOsc+4),x(3*nOsc+5),X),'fro');
```

167

```matlab
            x_init  = [Osc_loc'      ; ones(nOsc,1)        ;
                0.5*ones(nOsc,1) ; ...
                  1400 ; 6.7 ; opts.Te ; 0.5 ; 300];
            x_lower = [Osc_loc'-200 ; zeros(nOsc,1)       ;
                zeros(nOsc,1)    ; ...
                  1000 ; 5   ; Te_lower; 0   ; 250];
            x_upper = [Osc_loc'+200 ; 30 * ones(nOsc,1) ;
                ones(nOsc,1)     ; ...
                  2000 ; 10  ; Te_upper; 1   ; 300];
    end
case 'PCI'
    % Knot point spacing
    tmp = linspace(X(1),X(end),nOsc);
    del_xx = tmp(2)-tmp(1);

    % Number of out-of-band extrapolation points
    nOut = 5;

    % Knot point locations
    xx = [linspace(X(1)-nOut*del_xx,X(1)-del_xx,nOut)
        ...
          linspace(X(1),X(end),nOsc) linspace(X(end)+
            del_xx,X(end)+nOut*del_xx,nOut)];

    % Kappa at each knot point and extrapolate out of
       band
    K_tmp = @(yy) max(interp1(tmp,yy,xx,'linear','
       extrap'),0);

    % Apply the hilbert transform to kappa to solve
       for n
    N_tmp = @(yy,a) -imag(hilbert(K_tmp(yy))) + a;

    % Interpolate n and kappa back onto instrument
       spectral axis
    K = @(yy) interp1(tmp,max(yy,0),X,'pchip');
    N_tmp = @(yy,a) interp1(xx,N_tmp(yy,a),X,'pchip');

    % Index of refraction
    N = @(yy,a) N_tmp(yy,a) + 1i * K(yy);

    % Fresnel
```

```
cos_t = @ (yy ,a ,Theta) sqrt (1 - bsxfun(@times ,sin(
   Theta), ...
   1 ./ N(yy ,a)).^2);


R_s = @ (yy ,a ,Theta) abs(bsxfun(@minus ,cos(Theta),
   ...
   bsxfun(@times ,N(yy ,a),cos_t(yy ,a ,Theta))) ./
      bsxfun(@plus ,cos(Theta), ...
   bsxfun(@times ,N(yy ,a),cos_t(yy ,a ,Theta)))).^2;


R_p = @ (yy ,a ,Theta) abs((cos_t(yy ,a ,Theta) - ...
   repmat(N(yy ,a),nAng ,1) .* repmat(cos(Theta),1,
      nSpc)) ./ ...
   (cos_t(yy ,a ,Theta) + repmat(N(yy ,a),nAng ,1) .*
      ...
   repmat(cos(Theta),1,nSpc))).^2;


R = @ (yy ,a ,Theta) (R_s(yy ,a ,Theta) + R_p(yy ,a,
   Theta)) / 2;


if isempty(opts.Ld);
   % Theoretical S0
   S0_calc = @ (yy ,a ,Tg ,Tl ,H2O ,O3 ,Te ,v) R(yy ,a,
      theta) .* ...
         squeeze(down(:,round(Tg),round(Tl),round(
            H2O),round(O3),:)) + ...
         (1 - R(yy ,a ,theta)) .* repmat(planckian(v,
            Te),nAng ,1) * 1e6;


   % Theoretical tot_pol
   tot_pol_calc = @ (yy ,a ,Tg ,Tl ,H2O ,O3 ,Te ,v) (R_s
      (yy ,a ,theta) - ...
         R_p(yy ,a ,theta)) .* (0.5 .* squeeze(down
            (:,round(Tg),round(Tl),round(H2O),round
            (O3),:)) - ...
         repmat(planckian(v,Te),nAng ,1) * 0.5e6);
else
   % Theoretical S0
   S0_calc = @ (yy ,a ,Tg ,Tl ,H2O ,O3 ,Te ,v) R(yy ,a,
      theta) .* ...
         down + (1 - R(yy ,a ,theta)) .* repmat(
            planckian(v,Te),nAng ,1) * 1e6;
```

```matlab
        % Theoretical tot_pol
        tot_pol_calc = @ (yy,a,Tg,Tl,H2O,O3,Te,v) (R_s
            (yy,a,theta) - ...
             R_p(yy,a,theta)) .* (0.5 .* down - repmat(
                planckian(v,Te),nAng,1) * 0.5e6);
    end

    if dT == 0;
        % Define error function
        if S0_only
            error = @(x) norm(S0-S0_calc(x(1:nOsc),x(
                nOsc+1),x(nOsc+2), ...
                 x(nOsc+3),x(nOsc+4),x(nOsc+5),opts.Te,
                    X),'fro');
        elseif pol_only
            error = @(x) norm(tot_pol-tot_pol_calc(x
                (1:nOsc),x(nOsc+1),x(nOsc+2), ...
                 x(nOsc+3),x(nOsc+4),x(nOsc+5),opts.Te,
                    X),'fro');
        else
            error = @(x) norm(tot_pol-tot_pol_calc(x
                (1:nOsc),x(nOsc+1),x(nOsc+2), ...
                 x(nOsc+3),x(nOsc+4),x(nOsc+5),opts.Te,
                    X),'fro') + ...
                 norm(S0-S0_calc(x(1:nOsc),x(nOsc+1),x(
                    nOsc+2), ...
                 x(nOsc+3),x(nOsc+4),x(nOsc+5),opts.Te,
                    X),'fro');
        end

        % Initial guess for algorithm and bounds
        % x = [yy ; a ; Tg ; Tl ; H2O ; O3]
        x_init  = [ones(nOsc,1)    ; 1.4639 ; 10 ; 4 ;
            10 ; 10];
        x_lower = [zeros(nOsc,1)   ; 1      ; 1 ; 1  ;
            1  ; 1];
        x_upper = [10*ones(nOsc,1) ; 1.5    ; 20 ; 5 ;
            20 ; 20 ];
    else
        % Define error function
        if S0_only
            error = @(x) norm(S0-S0_calc(x(1:nOsc),x(
                nOsc+1),x(nOsc+2), ...
```

```matlab
                        x(nOsc+3),x(nOsc+4),x(nOsc+5),x(nOsc
                            +6),X),'fro');
            elseif pol_only
                error = @(x) norm(tot_pol-tot_pol_calc(x
                    (1:nOsc),x(nOsc+1),x(nOsc+2), ...
                     x(nOsc+3),x(nOsc+4),x(nOsc+5),x(nOsc
                        +6),X),'fro');
            else
                error = @(x) norm(tot_pol-tot_pol_calc(x
                    (1:nOsc),x(nOsc+1),x(nOsc+2), ...
                     x(nOsc+3),x(nOsc+4),x(nOsc+5),x(nOsc
                        +6),X),'fro') + ...
                     norm(S0-S0_calc(x(1:nOsc),x(nOsc+1),x(
                        nOsc+2), ...
                     x(nOsc+3),x(nOsc+4),x(nOsc+5),x(nOsc
                        +6),X),'fro');
            end

            % Initial guess for algorithm and bounds
            % x = [yy ; a ; Tg ; Tl ; H2O ; Te]
            x_init  = [ones(nOsc,1)     ; 1.4639 ; 10 ; 4 ;
                10 ; 10 ; opts.Te];
            x_lower = [zeros(nOsc,1)    ; 1.46    ; 1  ; 1 ;
                1  ; 1   ; Te_lower];
            x_upper = [10*ones(nOsc,1) ; 1.5      ; 20 ; 5 ;
                20 ; 20 ; Te_upper ];
        end
    case 'BIR'
        % Birefringence model for this fit is hard-coded
           to one oscillator
        % at this point
        nOsc = 1;

        % Lorentz oscillator model for dielectric constant
        e1 = @ (vp,v0,Xi,f,einf,v) einf + sum(repmat(f,1,
           nSpc) .* ...
            (repmat(vp,nOsc,nSpc).^2 .* (repmat(v0,1,nSpc)
               .^2 - ...
            repmat(v,nOsc,1).^2)) ./ ((repmat(v0,1,nSpc)
               .^2 - ...
            repmat(v,nOsc,1).^2).^2 + repmat(Xi,1,nSpc).^2
               .* repmat(v,nOsc,1).^2),1);
```

171

```matlab
e2 = @ (vp,v0,Xi,f,v) sum(repmat(f,1,nSpc) .* (
   repmat(vp,nOsc,nSpc).^2 .* ...
     repmat(Xi,1,nSpc) .* repmat(v,nOsc,1)) ./ ((
        repmat(v0,1,nSpc).^2 - ...
     repmat(v,nOsc,1).^2).^2 + repmat(Xi,1,nSpc).^2
        .* repmat(v,nOsc,1).^2),1);

% Index of refraction
N = @ (vp,v0,Xi,f,einf,v) repmat((1/sqrt(2)) .*
   sqrt(e1(vp,v0,Xi,f,einf,v) + ...
     sqrt(e1(vp,v0,Xi,f,einf,v).^2 + e2(vp,v0,Xi,f,
        v).^2)),nAng,1) + ...
     1i * repmat((1/sqrt(2)) .* sqrt(-e1(vp,v0,Xi,f
        ,einf,v) + ...
     sqrt(e1(vp,v0,Xi,f,einf,v).^2 + e2(vp,v0,Xi,f,
        v).^2)),nAng,1);

% Fresnel
cos_t = @ (vp,v0,Xi,f,einf,v,Theta) sqrt(1 -
   bsxfun(@times,sin(Theta), ...
     1 ./ N(vp,v0,Xi,f,einf,v)).^2);

R_s = @ (vp_s,v0_s,Xi_s,f_s,einf_s,v,Theta) abs(
   bsxfun(@minus,cos(Theta), ...
     bsxfun(@times,N(vp_s,v0_s,Xi_s,f_s,einf_s,v),
        cos_t(vp_s,v0_s,Xi_s,f_s,einf_s,v,Theta)))
        ./ bsxfun(@plus,cos(Theta), ...
     bsxfun(@times,N(vp_s,v0_s,Xi_s,f_s,einf_s,v),
        cos_t(vp_s,v0_s,Xi_s,f_s,einf_s,v,Theta))))
        .^2;

R_p = @ (vp_p,v0_p,Xi_p,f_p,einf_p,v,Theta) abs((
   cos_t(vp_p,v0_p,Xi_p,f_p,einf_p,v,Theta) - ...
     bsxfun(@times,N(vp_p,v0_p,Xi_p,f_p,einf_p,v),
        cos(Theta))) ./ ...
     (cos_t(vp_p,v0_p,Xi_p,f_p,einf_p,v,Theta) +
        bsxfun(@times,N(vp_p,v0_p,Xi_p,f_p,einf_p,v
        ), ...
     cos(Theta)))).^2;

R = @ (vp_s,v0_s,Xi_s,f_s,einf_s,vp_p,v0_p,Xi_p,
   f_p,einf_p,v,Theta) (R_s(vp_s,v0_s,Xi_s,f_s,
   einf_s,v,Theta) + ...
```

```matlab
            R_p(vp_p,v0_p,Xi_p,f_p,einf_p,v,Theta)) / 2;

if isempty(opts.Ld);
    % Theoretical S0
    S0_calc = @(vp_s,v0_s,Xi_s,f_s,einf_s,vp_p,
        v0_p,Xi_p,f_p,einf_p,Tg,Tl,H2O,O3,Te,v) ...
          R(vp_s,v0_s,Xi_s,f_s,einf_s,vp_p,v0_p,Xi_p
              ,f_p,einf_p,v,theta) .* ...
          squeeze(down(:,round(Tg),round(Tl),round(
              H2O),round(O3),:)) + ...
          (1 - R(vp_s,v0_s,Xi_s,f_s,einf_s,vp_p,v0_p
              ,Xi_p,f_p,einf_p,v,theta)) .* repmat(
              planckian(v,Te),nAng,1) * 1e6;

    % Theoretical total polarization
    tot_pol_calc = @(vp_s,v0_s,Xi_s,f_s,einf_s,
        vp_p,v0_p,Xi_p,f_p,einf_p,Tg,Tl,H2O,O3,Te,v
        ) ...
          (R_s(vp_s,v0_s,Xi_s,f_s,einf_s,v,theta) -
              R_p(vp_p,v0_p,Xi_p,f_p,einf_p,v,theta))
              ...
          .* (0.5 .* squeeze(down(:,round(Tg),round(
              Tl),round(H2O),round(O3),:)) - ...
          repmat(planckian(v,Te),nAng,1) * 0.5e6);
else
    % Theoretical S0
    S0_calc = @(vp_s,v0_s,Xi_s,f_s,einf_s,vp_p,
        v0_p,Xi_p,f_p,einf_p,Tg,Tl,H2O,O3,Te,v) ...
          R(vp_s,v0_s,Xi_s,f_s,einf_s,vp_p,v0_p,Xi_p
              ,f_p,einf_p,v,theta) .* ...
          down + (1 - R(vp_s,v0_s,Xi_s,f_s,einf_s,
              vp_p,v0_p,Xi_p,f_p,einf_p,v,theta)) .*
              repmat(planckian(v,Te),nAng,1) * 1e6;

    % Theoretical total polarization
    tot_pol_calc = @(vp_s,v0_s,Xi_s,f_s,einf_s,
        vp_p,v0_p,Xi_p,f_p,einf_p,Tg,Tl,H2O,O3,Te,v
        ) ...
          (R_s(vp_s,v0_s,Xi_s,f_s,einf_s,v,theta) -
              R_p(vp_p,v0_p,Xi_p,f_p,einf_p,v,theta))
              ...
          .* (0.5 .* down - repmat(planckian(v,Te),
              nAng,1) * 0.5e6);
```

```matlab
        end

        % Define error function
        if S0_only
            error = @(x) norm(S0-S0_calc(x(4),x(1),x(2),x
                (3),x(5),x(9),x(6),x(7),...
                 x(8),x(10),x(11),x(12),x(13),x(14),x(15),X
                    ),'fro');
        elseif pol_only
            error = @(x) norm(tot_pol-tot_pol_calc(x(4),x
                (1),x(2),x(3),x(5),x(9),x(6),x(7),...
                 x(8),x(10),x(11),x(12),x(13),x(14),x(15),X
                    ),'fro');
        else
            error = @(x) norm(tot_pol-tot_pol_calc(x(4),x
                (1),x(2),x(3),x(5),x(9),x(6),x(7),...
                 x(8),x(10),x(11),x(12),x(13),x(14),x(15),X
                    ),'fro') + ...
                 norm(S0-S0_calc(x(4),x(1),x(2),x(3),x(5),x
                    (9),x(6),x(7),...
                 x(8),x(10),x(11),x(12),x(13),x(14),x(15),X
                    ),'fro');
        end

        % Initial guess for algorithm and bounds
        % x = [v0 ; Xi ; f ; vp ; einf ; Tg ; Tl ; H2O ;
            O3 ; Te]
        x_init  = [548 ; 14 ; 1 ; 1250 ; 3 ; 450 ; 18 ; 1
            ; 1350 ; 3 ; 10 ; 4 ; 10 ; 10 ; opts.Te];
        x_lower = [300 ; 10 ; 1 ; 1000 ; 0 ; 290 ; 10 ; 1
            ; 1000 ; 0 ; 1  ; 1 ; 1  ; 1  ; Te_lower];
        x_upper = [800 ; 20 ; 1 ; 4000 ; 5 ; 790 ; 20 ; 1
            ; 4000 ; 5 ; 20 ; 5 ; 20 ; 20 ; Te_upper];
end

% Implement algorithm of choice to search the parameter
   space. By default
% the bounded fminsearch is used.
switch opts.Algorithm
    case 'fmsb'
        [x_meas,fval,exitflag,output] = fminsearchbnd(
            error,x_init,x_lower,x_upper,...
```

```matlab
                    optimset('MaxFunEvals',1e15,'MaxIter',1.5e4,'
                        PlotFcns',@optimplotfval));
        case 'q-n'
            fitopts = optimoptions('fminunc','Algorithm','
                quasi-newton',...
                'MaxFunEvals',1e15,'PlotFcns',@optimplotfval);
            [x_meas,fval,~,~,~] = fminunc(error,x_init,fitopts
                );
        case 'hybrid'
            [x_meas,~,exitflag,output] = fminsearchbnd(error,
                x_init,x_lower,x_upper,...
                    optimset('MaxFunEvals',1e15,'MaxIter',200,'
                        PlotFcns',@optimplotfval));

            fitopts = optimoptions('fminunc','Algorithm','
                quasi-newton',...
                'MaxFunEvals',1e15,'PlotFcns',@optimplotfval);
            [x_meas,fval,~,~,~] = fminunc(error,x_meas,fitopts
                );
end

% Parse out oscillator parameters
switch opts.Model
    case 'LOM'
        if opts.adj == 1;
            Parameters.v0   = x_meas(1:nOsc);
            Parameters.Xi   = x_meas(nOsc+1:2*nOsc);
            Parameters.f    = x_meas(2*nOsc+1:3*nOsc);
            Parameters.vp   = x_meas(3*nOsc+1);
            Parameters.einf = x_meas(3*nOsc+2);
            Te              = x_meas(3*nOsc+3);
            Parameters.adj  = x_meas(3*nOsc+4);
            Parameters.Tr   = x_meas(3*nOsc+5);
        else
        Parameters.v0   = x_meas(1:nOsc);
        Parameters.Xi   = x_meas(nOsc+1:2*nOsc);
        Parameters.f    = x_meas(2*nOsc+1:3*nOsc);
        Parameters.vp   = x_meas(3*nOsc+1);
        Parameters.einf = x_meas(3*nOsc+2);
        Parameters.Tg   = x_meas(3*nOsc+3);
        Parameters.Tl   = x_meas(3*nOsc+4);
        Parameters.H2O  = x_meas(3*nOsc+5);
        Parameters.O3   = x_meas(3*nOsc+6);
```

```matlab
            Te                  = x_meas(3*nOsc+7);
%           Parameters.TrLim = [Tr_lower Tr_upper];
%           Parameters.TeLim = [Te_lower Te_upper];
        end

        % Predicted Downwelling Radiance
        if isempty(opts.Ld);
            Ld = squeeze(down(:,round(Parameters.Tg),round
                (Parameters.Tl),...
                 round(Parameters.H2O),round(Parameters.O3)
                     ,:));
        else Ld = opts.Ld;
        end

        % Predicted n and kappa
        n       = real(mean(N(Parameters.vp,Parameters.v0,
            Parameters.Xi, ...
            Parameters.f,Parameters.einf,X),1));
        kappa = imag(mean(N(Parameters.vp,Parameters.v0,
            Parameters.Xi, ...
            Parameters.f,Parameters.einf,X),1));
    case 'PCI'
        if dT == 0;
            Parameters.yy = x_meas(1:nOsc);
            Parameters.a  = x_meas(nOsc+1);
            Parameters.Tg            = x_meas(nOsc+2);
            Parameters.Tl            = x_meas(nOsc+3);
            Parameters.H2O           = x_meas(nOsc+4);
            Parameters.O3            = x_meas(nOsc+5);
            Te              = opts.Te;
        else
            Parameters.yy = x_meas(1:nOsc);
            Parameters.a  = x_meas(nOsc+1);
            Parameters.Tg = x_meas(nOsc+2);
            Parameters.Tl = x_meas(nOsc+3);
            Parameters.H2O = x_meas(nOsc+4);
            Parameters.O3 = x_meas(nOsc+5);
            Te = x_meas(nOsc+6);
%           Parameters.TrLim = [Tr_lower Tr_upper];
%           Parameters.TeLim = [Te_lower Te_upper];
        end

        % Predicted downwelling radiance
```

```matlab
        if isempty(opts.Ld);
            Ld = squeeze(down(:,round(Parameters.Tg),round
                (Parameters.Tl),...
                  round(Parameters.H2O),round(Parameters.O3)
                    ,:)));
        else Ld = opts.Ld;
        end

        % Predicted n and kappa
        n     = mean(real(N(Parameters.yy,Parameters.a))
            ,1);
        kappa = mean(K(Parameters.yy),1);
    case 'BIR'
        Parameters.v0_s   = x_meas(1);
        Parameters.Xi_s   = x_meas(2);
        Parameters.f_s    = x_meas(3);
        Parameters.vp_s   = x_meas(4);
        Parameters.einf_s = x_meas(5);
        Parameters.v0_p   = x_meas(6);
        Parameters.Xi_p   = x_meas(7);
        Parameters.f_p    = x_meas(8);
        Parameters.vp_p   = x_meas(9);
        Parameters.einf_p = x_meas(10);
        Parameters.Tg     = x_meas(11);
        Parameters.Tl     = x_meas(12);
        Parameters.H2O    = x_meas(13);
        Parameters.O3     = x_meas(14);
        Te                = x_meas(15);

        Parameters.n_1 = real(mean(N(Parameters.vp_s,
            Parameters.v0_s,Parameters.Xi_s,Parameters.f_s,
            Parameters.einf_s,X),1));
        Parameters.n_2 = real(mean(N(Parameters.vp_p,
            Parameters.v0_p,Parameters.Xi_p,Parameters.f_p,
            Parameters.einf_p,X),1));

        Parameters.k_1 = imag(mean(N(Parameters.vp_s,
            Parameters.v0_s,Parameters.Xi_s,Parameters.f_s,
            Parameters.einf_s,X),1));
        Parameters.k_2 = imag(mean(N(Parameters.vp_p,
            Parameters.v0_p,Parameters.Xi_p,Parameters.f_p,
            Parameters.einf_p,X),1));
```

177

```matlab
        % Predicted n and kappa
        n = (Parameters.n_1 + Parameters.n_2) / 2;
        kappa = (Parameters.k_1 + Parameters.k_2) / 2;

        % Predicted downwelling radiance
        if isempty(opts.Ld);
            Ld = squeeze(down(:,round(Parameters.Tg),round
                (Parameters.Tl),...
                round(Parameters.H2O),round(Parameters.O3)
                    ,:));
        else Ld = opts.Ld;
        end
end

disp(['Objective Function Value = ' num2str(fval)]);
```

Bibliography

1. J.H. Hough and D.K. Aitken. Polarimetry in the infrared: what can be learned? *Journal of Quantitative Spectroscopy And Radiative Transfer*, pages 733–740, 2003.

2. Dinos P. Gonatas, X.D. Wu, Giles Novak, and R.H. Hildebrand. Systematic effects in the measurement of far-infrared linear polarization. *Applied Optics*, 28(5):1000–1006, 1989.

3. William J. Checovich, Randall E. Bolger, and Thomas Burke. Fluorescence polarization–a new tool for cell and molecular biology. *Nature*, 375(6528):254–256, 1995.

4. Marie Dacke, Peter Nordstrom, and Clarke H. Scholtz. Twilight orientation to polarised light in the crepuscular dung beetle scarabaeus zambesianus. *Journal of experimental biology*, 2006(9):1535–1543, 2003.

5. K.M. Twietmeyer, R.A. Chipman, A.E. Elsner, Y. Zhao, and D. VanNasdale. Mueller matrix retinal imager with optimized polarization conditions. *Optics Express*, 16(26):21339–21354, December 2008.

6. Steven L. Jacques, Jessica R. Roman, and Ken Lee. Imagining superficial tissues with polarized light. *Lasers in surgery and medicine*, 26(2):119–129, 2000.

7. M.J. Duggin, S.A. Israel, V.S. Whitehead, J.S. Myers, and D.R. Robertson. Use of polarization methods in earth resources investigations. In Russell A. Chipman, editor, *Polarization Considerations for Optical Systems II*, volume 1166, 1990.

8. V.S. Whitehead and Kinsell Coulson. The space shuttle as a polarization observation platform. In Russell A. Chipman, editor, *Polarization Considerations for Optical Systems II*, volume 1166, 1990.

9. Prasad Srinivasa Thenkabail, John G. Lyon, and Alfredo Huete. *Hyperspectral remote sensing of vegetation*. Boca Raton, FL: CRC Press, 2012.

10. Niels Henrik Broge and E. Leblanc. Comparing prediction power and stability of broadband and hyperspectral vegetation indices for estimation of green leaf area index and canopy chlorophyll density. *Remote Sensing of Environment*, 76(2):156–172, 2001.

11. E.A. Cloutis. Review article hyperspectral geological remote sensing: evaluation of analytical techniques. *International Journal of Remote Sensing*, 17(12):2215–2242, 1996.

12. Freek D. Van der Meer, Harald van der Werff, Frank JA van Ruitenbeek, Chris A. Hecker, Wim H. Bakker, Marleen F. Noomen, Mark van der Meijde, E. John M. Carranza, J. Smeth, and Tsehaie Woldai. Multi-and hyperspectral geologic remote sensing: A review. *International Journal of Applied Earth Observation and Geoinformation*, 14(1):112–128, 2012.

13. Kenneth C. Bradley, Kevin C. Gross, and Glen P. Perram. Imaging fourier transform spectrometry of chemical plumes. In Augustus W. Fountain III and Patrick J. Garner, editors, *Chemical, Biological, Radiological, Nuclear, and Explosives (CBRNE) Sensing X*, volume 7304, 2009.

14. Michele Hinnrichs. Remote sensing for gas plume monitoring using state-of-the-art infrared hyperspectral imaging.

15. Hamed Akbari, Kuniaki Uta, Yukio Kosugi, Kazuyuki Kojima, and Naofumi Tanaka. Cancer detection using infrared hyperspectral imaging. *Cancer Science*, 102(4):852–857, April 2011.

16. Donald B. Malkoff and William R. Oliver. Hyperspectral imaging applied to forensic medicine. In Gregory H. Bearman, Dario Cabib, and Richard M. Levenson, editors, *Spectral Imaging: Instrumentation, Applications, and Analysis*, volume 3920, 2000.

17. Jeff Dozier and Stephen G. Warren. Effect of viewing angle on the infrared brightness temperature of snow. *Water Resources Research*, 18(5):1424–1434, October 1982.

18. J. Labed and M.P. Stoll. Angular variation of land surface spectral emissivity in the thermal infrared: laboratory investigations of bare soils. *International Journal of Remote Sensing*, 12(11):2299–2310, 1991.

19. J.P. Lagouarde, Y.H. Kerr, and Y. Brunet. An experimental study of angular effects on surface temperature for various plant canopies and bare soils. *Agricultural and Forest Meteorology*, 77:167–190, December 1995.

20. Jose A. Sobrino and Juan Cuenca. Angular variation of thermal infrared emissivity for some natural surfaces from experimental measurements. *Applied Optics*, 38(18):3931–3936, 1999.

21. Christopher J. Deloye, Michael S. West, and John M. Grossmann. Changes in apparent emissivity as a function of viewing geometry. In *Active and Passive Signatures II*, volume 8040, 2011.

22. Mark Fox. *Optical Properties of Solids*. Oxford University Press, second edition, 2010.

23. Michael T. Eismann. *Hyperspectral Remote Sensing*. SPIE Press, 2012.

24. Bruce Hapke. *Theory of Reflectance and Emittance Spectroscopy.* Cambridge University Press, second edition, 2012.

25. John David Jackson. *Classical Electrodynamics.* John Wiley And Sons, third edition, 1999.

26. Andrew Resnick, Chris Persons, and George Lindquist. Polarized emissivity and kirchoff's law. *Applied Optics*, 38(8):1384–1387, March 1999.

27. Daniel A. LeMaster and Michael T. Eismann. *Passive Polarimetric Imaging, in Multi-Dimensional Imaging.* John Wiley And Sons, 2014.

28. Timothy J. Rogne, Frederick G. Smith, and James E. Rice. Passive target detection using polarized components of infrared signatures. In *Polarimetry: Radar, Infrared, Visible, Ultraviolet, and X-Ray*, volume 1317, 1990.

29. D.E. Aspnes. *Handbook of Optical Constants of Solids.* Academic Press, 1985.

30. R.M.A. Azzam. Ellipsometric configurations and techniques. In David E. Aspnes, Roy F. Potter, and Samuel S. So, editors, *Optical Characterization Techniques for Semiconductor Technology*, volume 0276, 1981.

31. J.A. Woollam Co., Lincoln, Nebraska, United States. *WVASE.*

32. H.E. Revercomb, H. Bujis, H.B. Howell, D.D. LaPorte, W.L. Smith, and L.A. Sromovsky. Radiometric calibration of ir fourier transform spectrometers: solution to a problem with the high-resolution interferometer sounder. *Applied Optics*, 27:3210–3218, 1988.

33. Joel G. Holder, Jacob A. Martin, Jeremey Pitz, Joseph L. Pezzaniti, and Kevin C. Gross. Calibration methodology and performance characterization of a polarimetric hyperspectral imager. In David B. Chenault and Dennis H. Goldstein, editors, *Polarization: Measurement, Analysis, and Remote Sensing XI*, volume 9099, May 2014.

34. Joel G. Holder. Polarimetric calibration and characterization of the telops field portable polarimetric-hyperspectral imager. Master's thesis, Air Force Institute of Technology, March 2014.

35. Christopher M. Persons, Michael W. Jones, Craig A. Farlow, L. Denise Morell, Michael G. Gulley, and Kevin D Spradley. A proposed standard method for polarimetric calibration and calibration verification. In Joseph A. Shaw and J. Scott Tyo, editors, *Polarization Science and Remote Sensing III*, volume 6682, 2007.

36. Charles A. Hibbitts. Optical signatures of buried mines. In *NATO Advanced Study Institute on Imaging for Detection and Identification*, pages 49–63, 2007.

37. Aed El-Saba and Tadele Bezuayehu. Higher probability of detection of subsurface land mines with a single sensor using multiple polarized and unpolarized image fusion. In David B. Chenault and Dennis H. Goldstein, editors, *Polarization: Measurement, Analysis, and Remote Sensing VIII*, volume 6972, 2008.

38. Herman E. Scott, Stephen H. Jones, Frank Iannarilli, and Kurt Annen. Hyperspectral ir polarimetry with applications in demining and unexploded ordnance detection. In *Conference of Environmental Monitoring and Remediation Technologies*, volume 3534, November 1998.

39. Gary A. Atkinson and Edwin R. Hancock. Recovery of surface orientation from diffuse polarization. *IEEE Transactions on Image Processing*, 15(6):1653–1664, June 2006.

40. Gary A. Atkinson and Edwin R. Hancock. Shape estimation using polarization and shading from two views. *IEEE Transactions on Pattern Analysis and Machine Intelligence*, 29(11):2001–2017, November 2007.

41. Daisuke Miyazaki, Megumi Saito, Yoichi Sato, and Katsushi Ikeuchi. Determining surface orientations of transparent objects based on polarization degrees in visible and infrared wavelengths. *Journal of Optical Society of America A*, 19(4):687–694, 2002.

42. Daisuke Miyazaki, Robby T. Tan, Kenji Hara, and Katsushi Ikeuchi. Polarization-based inverse rendering from a single view. *Proceedings of the Ninth IEEE International Conference on Computer Vision*, 2003.

43. Daisuke Miyazaki, Masataka Kagesawa, and Katsushi Ikeuchi. Transparent surface modeling from a pair of polarization images. *IEEE Transactions on Pattern Analysis and Machine Intelligence*, 26(1):73–82, January 2004.

44. Daisuke Miyazaki and Katsushi Ikeuchi. Inverse polarization raytracing: Estimating surface shapes of transparent objects. *IEEE Computer Society Conference on Computer Vision and Pattern Recognition*, 2:910–917, June 2005.

45. Michael Gartley, Peter Erbach, and Larry Pezzaniti. Pose estimation of unresolved targets using polarimetric imaging. In David B. Chenault and Dennis H. Goldstein, editors, *Polarization: Measurement, Analysis, and Remote Sensing IX*, volume 7672, 2010.

46. Robert B. Reid, Mark E. Oxley, Michael T. Eismann, and Matthew E. Goda. Quantifying surface normal estimation. In Dennis H. Goldstein and David B. Chenault, editors, *Polarization: Measurement, Analysis, and Remote Sensing VII*, volume 6240, 2006.

47. Lawrence B. Wolff, Andrew Lundberg, and Renjie Tang. Image understanding from thermal emission polarization. *IEEE Computer Society Conference on Computer Vision and Pattern Recognition*, pages 625–631, June 1998.

48. M. Vedel, N. Lechocinski, and S. Breugnot. 3d shape reconstruction of optical element using polarization. In David B. Chenault and Dennis H. Goldstein, editors, *Polarization: Measurement, Analysis, and Remote Sensing IX*, volume 7672. SPIE, 2010.

49. Qingsong Wang, Charles D. Creusere, Vimal Thilak, and David G. Voelz. Active polarimetric imaging for estimation of scene geometry. *Digital Signal Processing Workshop and 5th IEEE Signal Processing Education Workshop*, pages 659–663, January 2009.

50. Anand Pamba, Vimal Thilak, David G. Voelz, and Charles D. Creusere. Estimation of incidence and reflection angles from passive polarimetric imagery: extention to out-of-plane scattering. In Joseph A. Shaw and J. Scott Tyo, editors, *Polarization Science and Remote Sensing III*, volume 6682, August 2007.

51. Lawrence B. Wolff. Surface orientation from polarization images. In *Optics, Illumination, and Image Sensing for Machine Vision II*, volume 850, 1987.

52. Lawrence B. Wolff. Surface orientation from two camera stereo with polarizers. In *Optics, Illumination, and Image Sensing for Machine Vision IV*, volume 1194, 1989.

53. Irving S. Reed and Xiaoli Yu. Adaptive multiple-band cfar detection of an optical pattern with unknown spectral distribution. *IEEE Transactions on Acoustics, Speech, and Signal Processing*, 38(10):1760–1770, October 1990.

54. Heesung Kwon and Nasser M. Nasrabadi. Kernel rx-algorithm: A nonlinear anomaly detector for hyperspectral imagery. *IEEE Transactions on Geoscience and Remote Sensing*, 43(2):388–397, February 2005.

55. L.L. Scharf. Matched subspace detectors. *IEEE Transactions on Signal Processing*, 42(8):2146–2157, August 1994.

56. Glenn Healey and David Slater. Models and methods for automated material identification in hyperspectral imagery acquired under unknown illumination and atmospheric conditions. *IEEE Transactions on Geoscience and Remote Sensing*, 37(6):2706–2717, November 1999.

57. Joseph Meola and Michael T. Eismann. Methods for multi-temporal change detection. In Sylvia S. Shen and Paul E. Lewis, editors, *SPIE Algorithm and Technologies for Multispectral, Hyperspectral, and Ultraspectral Imagery XV*, number 7334, 2009.

58. Joseph Meola, Michael T. Eismann, Randolph L. Moses, and Joshua N. Ash. Detecting changes in hyperspectral imagery using a model-based approach. *IEEE Transactions on Geoscience and Remote Sensing*, 49(7):2647–2661, July 2011.

59. F.A. Kruse, A.B. Lefkoff, J.W. Boardman, K.B. Heiedbrecht, A.T. Shapiro, P.J. Barloon, and A.F.H. Goetz. The spectral image processing system (sips) - interactive visualization and analysis of imaging spectrometer data. *Remote Sensing of Environment*, 44(2):145–163, 1993.

60. Osmar Abilio de Carvalho Jr and Paulo Roberto Meneses. Spectral correlation mapper (scm): An improvement on the spectral angle mapper (sam). In *Summaries of the 9th JPL Airborne Earth Science Workshop*, volume 9, 2000.

61. Shawn Kraut, Louis L. Scharf, and L. Todd McWhorter. Adaptive subspace detectors. *IEEE Transactions on Signal Processing*, 49(1), January 2001.

62. Richard D. Tooley. Man-made target detection using infrared polarization. In *Polarization Considerations for Optical Systems II*, volume 1166, 1989.

63. Florence Nadal and Francois-Marie Breon. Parameterization of surface polarized reflectance derived from polder spaceborne measurements. *IEEE Transactions on Geoscience and Remote Sensing*, 37(3):1709–1718, May 1999.

64. Firooz A. Sadjadi and Cornell S. L. Chun. Automatic detection of small objects from their infrared state-of-polarization vectors. *Optics Letters*, 28(7):532–533, April 2003.

65. Shadi Sumrain and George C. Giakos. Efficient polarimetric detection of manmade targets. *IEEE International Workshop on Imaging Systems and Techniques*, pages 20–25, May 2005.

66. Michael J. Duggin, William R. Glass, Elizabeth R. Cabot, David Bowers, David Wellems, and Paul Alsing. Information enhancement, metrics and data fusion in spectral and polarimetric images of natural scenes. In Joseph A. Shaw and J. Scott Tyo, editors, *Polarization Science and Remote Sensing III*, volume 6682, 2007.

67. Daniel A. Lavigne, Melanie Breton, Mario Pichette, Vincent Larochelle, and Jean-Robert Simard. Evaluation fo active and passive polarimetric electro-optic imagery for civilian and military targets discrimination. In David B. Chenault and Dennis H. Goldstein, editors, *Polarization: Measurement, Analysis, and Remote Sensing VIII*, volume 6972, 2008.

68. Yong-Qiang Zhao, Peng Gong, and Quan Pan. Object detection by spectropolarimetric imagery fusion. *IEEE Transactions on Geoscience and Remote Sensing*, 46(10):3337–3345, October 2008.

69. James McCarthy, Mark Wooley, and Luz Roth. Correlation of environmental data measurements with polarimetric lwir sensor measurements of manmade objects in natural clutter. In David B. Chenault and Dennis H. Goldstein, editors, *Polarization: Measurement, Analysis, and Remote Sensing IX*, volume 7672, 2010.

70. A.M. El-Saba, M.S. Alam, and A. Surpanani. Application of passive imaging polarimetry in the discrimination and detection of different color targets of identical shapes using color-blind imaging sensors. In Dennis H. Goldstein and David B. Chenault, editors, *Polarization: Measurement, Analysis, and Remote Sensing VII*, 2006.

71. Aed El-Saba and Wesam A. Sakla. Linear high-boost fusion of stokes vector imagery for effective discrimination and recognition of real targets in the presence of multiple identical decoys. In David B. Chenault and Dennis H. Goldstein, editors, *Polarization: Measurement, Analysis, and Remote Sensing IX*, volume 7672, 2010.

72. Brian M. Flusche, Michael G. Gartley, and John R. Schott. Exploiting spectral and polarimetric data fusion to enhance target detection performance. In Sylvia S. Shen and Paul E. Lewis, editors, *Imaging Spectrometry XV*, volume 7812, 2010.

73. William H. Farrand and Joseph C. Harsanyi. Mapping the distribution of mine tailings in the coeur d'alene river valley, idaho, through the use of a constrained energy minimization technique. *Remote Sensing of Environment*, 59(1):64–76, January 1997.

74. William F. Basener and David W. Messinger. Enhanced detection and visualization of anomalies in spectral imagery. In Sylvia S. Shen and Paul E. Lewis, editors, *Algorithms and Technologies for Multispectral, Hyperspectral, and Ultraspectral Imagery XV*, volume 7334, April 2009.

75. Lingei Meng and John P. Kerekes. Adaptive target detection with a polarization-sensitive optical system. *Applied Optics*, 50(13):1925–1932, May 2011.

76. Joao M. Romano and Dalton Rosario. A covariance-based anomaly detector for polarimetric remote sensing applications. In David B. Chenault and Dennis H. Goldstein, editors, *Polarization: Measurement, Analysis, and Remote Sensing XI*, volume 9099, 2014.

77. Ken Watson. Two-temperature method for measuring emissivity. *Remote Sensing of Environment*, 42(2):117–121, November 1992.

78. Zhengming Wan and Jeff Dozier. A generalized split-window algorithm for retrieving land-surface temperature from space. *IEEE Transactions on Geoscience and Remote Sensing*, 34(4):892–905, July 1996.

79. Jie Cheng, Qing Xiao, Xiaowen Li, and QinHuo Liu. Multi-layer perceptron neural network based algorithm for simultaneous retrieving temperature and emissivity from hyperspectral ftir dataset. In *IEEE International Geoscience and Remote Sensing Symposium*, pages 4383–4385, July 2007.

80. Jie Cheng, QinHuo Liu, Xiaowen Li, Qing Xiao, Qiang Liu, and YongMing Du. Correlation-based temperature and emissivity separation algorithm. *Science in China Series D: Earth Sciences*, 51(3):357–369, March 2008.

81. Jie Cheng, Shunlin Liang, Jindi Wang, and Xiaowen Li. A stepwise refining algorithm of temperature and emissivity separation for hyperspectral thermal infrared data. *IEEE Transactions on Geoscience and Remote Sensing*, 48(3):1588–1597, March 2010.

82. Anne B. Kahle, Daryl P. Madura, and James M. Soha. Middle infrared multispectral aircraft scanner data: analysis for geological applications. *Applied Optics*, 19(14):2279–2290, 1980.

83. A.R. Gillespie. Lithologic mapping of silicate rocks using tims. In *TIMS Data User's Workshop*, pages 29–44, June 1985.

84. Peter S. Kealy and Simon J. Hook. Separating temperature and emissivity in thermal infrared multispectral scanner data: Implications for recovering land surface temperatures. *IEEE Transactions on Geoscience and Remote Sensing*, 31(6):1155–1164, November 1993.

85. A.R. Gillespie, S. Rokugawa, S.J. Hook, T. Matsunaga, and A.B. Kahle. Temperature/emissivity separation algorithm theorhetical basis document version 2.4. Technical report, NASA Contract NAS5-31372, March 1999.

86. T. Matsunaga. A temperature-emissivity separation method using an empirical relationship between the mean, the maximum and the minimum of the thermal infrared emissivity spectrum. *J. Remote Sens. Soc. Jpn.*, 14(3):28–39, 1994.

87. Alan Gillespie, Shuichi Rokugawa, Tsuneo Matsunaga, J. Steven Cothern, Simon Hook, and Anne B. Kahle. A temperature and emissivity separation algorithm for advanced spaceborne thermal emission and reflection radiometer (aster) images. *IEEE Transactions on Geoscience and Remote Sensing*, 36(4):1113–1126, July 1998.

88. Christoph C. Borel. Surface emissivity and temperature retrieval for a hyperspectral sensor. In *Geoscience and Remote Sensing Symposium Proceedings*, volume 1, 1998.

89. Christoph C. Borel and Ronald F. Tuttle. Recent advances in temperature-emissivity separation algorithms. *IEEE Aerospace Conference*, pages 1–14, March 2011.

90. Kenneth M. Hoffman and Ray Kunze. *Linear Algebra*. Pearson, 2nd edition, 1971.

91. Herve Adbi and Lynne J. Williams. Principle component analysis. *Computational Statistics*, 2(4):433–459, July 2010.

92. J. MacQueen. Some methods for classification and analysis of multivariate observations. In *Proceedings of the Fifth Berkeley Symposium on Mathematical Statistics and Probability*, volume 1, pages 281–297, 1967.

93. Pascale Masson and Wojciech Pieczynski. Sem algorithm and unsupervised statistical segmentation of satellite images. *IEEE Transactions on Geoscience and Remote Sensing*, 31(3):618–633, May 1993.

94. James J. Simpson, Timothy J. McIntire, and Matthew Sienko. An improved hybrid clustering algorithm for natural scenes. *IEEE Transactions on Geoscience and Remote Sensing*, 38(2):1016–1032, March 2000.

95. Farid Melgani and Lorenzo Bruzzone. Classification of hyperspectral remote sensing images with support vector machines. *IEEE Transactions on Geoscience and Remote Sensing*, 42(8):1178–1190, August 2004.

96. Nirmal Keshava and John F. Mustard. Spectral unmixing. *IEEE Signal Processing Magazine*, pages 44–57, January 2002.

97. Uta Heiden, Karl Segl, Sigrid Roessner, and Hermann Kaufmann. Determination of robust spectral features for identificiation of urban surface materials in hyperspectral remote sensing data. *Remote Sensing of Environment*, 111:537–552, April 2007.

98. David Slater and Glenn Healey. Material classification for 3d objects in aerial hyperspectral images. *IEEE Computer Society Conference on Computer Vision and Pattern Recognition*, 2, June 1999.

99. R. Greg Vaughan, Simon J. Hook, Wendy M. Calvin, and James V. Taranik. Surface mineral mapping at steamboat springs, nevada, usa, with multi-wavelength thermal infrared images. *Remote Sensing of Environment*, 99:140–158, April 2005.

100. Joseph A. Shaw. Polarimetric measurements of long-wave infrared spectral radiance from water. *Applied Optics*, 40(33):5985–5990, November 2001.

101. Lawrence B. Wolff. Classification of material surfaces using the polarization of specular highlights. *Proc. SPIE 1005 Optics, Illumination, and Image Sensing for Machine Vision*, pages 206–213, November 1988.

102. Lawrence B. Wolff. Polarization-based material classification from specular reflection. *IEEE Transactions on Pattern Analysis and Machine Intelligence*, 12(11):1059–1071, November 1990.

103. Lawrence B. Wolff and Terrance E. Boult. Constraining object features using a polarization reflectance model. *IEEE Transactions on Pattern Analysis and Machine Intelligence*, 13(7):635–657, July 1991.

104. Shoji Tominaga and Akira Kimachi. Polarization imaging for material classification. *Optical Engineering*, 47(12), December 2008.

105. Douglas G. Jones, Dennis H. Goldstein, and Jonathan C. Spaulding. Reflective and polarimetric characteristics of urban materials. September 2006.

106. Jihad Zallat, Piera Graebling, and Yoshi Takakura. Using polarimetric imaging for material classification. In *International Conference on Image Processing*, volume 3, pages 827–830, September 2003.

107. Dennis H. Goldstein and Joseph L. Cox. Spectropolarimetric properties of vegetation. In Dennis H. Goldstein and David B. Chenault, editors, *Polarization: Measurement, Analysis, and Remote Sensing VI*, volume 5432, 2004.

108. Yongqiang Zhao, Quan Pan, and Hongcai Zhang. Material classification based on multi-band polarimetric images fusion. In Dennis H. Goldstein and David B. Chenault, editors, *Polarization: Measurement, Analysis, and Remote Sensing VII*, volume 6240, 2006.

109. Chen Chao, Zhao Yong-qiang, Luo Li, Liu Dan, and Pan Quan. Robust materials classification based on multispectral polarimetric brdf imagery. *Proc. SPIE 7384 International Symposium on Photoelectronic Detection and Applications*, August 2009.

110. Sungwook Hong. Retrieval of refractive index over specular surfaces for remote sensing applications. *Journal of Applied Remote Sensing*, 3, October 2009.

111. Vimal Thilak, Charles D. Creusere, and David G. Voelz. Estimating the complex index of refraction and view angle of an object using multiple polarization measurements. *IEEE Fourtieth Asilomar Conference on Signal, Systems, and Computers*, pages 1067–1071, 2006.

112. Vimal Thilak, David Voelz, Charles Creusere, and Srikanth Damarla. Estimating the refractive index and reflected zenith angle of a target using multiple polarization measurements. *Proc. SPIE 6240 Polarization: Measurement, Analysis, and Remote Sensing VII*, (6240), May 2006.

113. Vimal Thilak, David G. Voelz, and Charles D. Creusere. Image segmentation from multi-look passive polarimetric imagery. *Proc. SPIE 6682 Polarization Science and Remote Sensing III*, September 2007.

114. Vimal Thilak, Charles D. Creusere, and David G. Voelz. Material classification using passive polarimetric imagery. *IEEE International Conference of Image Processing*, IV:121–124, September 2007.

115. Vimal Thilak, David G. Voelz, and Charles D. Creusere. Polarization-based index of refraction and reflection angle estimation for remote sensing applications. *Applied Optics*, 46(30):7527–7536, October 2007.

116. Vimal Thilak, Qingsong Wang, David G. Voelz, and Charles D. Creusere. Estimation of target geometry from mueller matrix imagery. In David B. Chenault and Dennis H. Goldstein, editors, *Polarization: Measurement, Analysis, and Remote Sensing VIII*, volume 6972, March 2008.

117. Vimal Thilak, Charles D. Creusere, and David G. Voelz. Passive polarimetric imagery based material classification for remote sensing applications. In *IEEE Southwest Symposium on Image Analysis and Interpretation*, pages 153–156, March 2008.

118. Vimal Thilak. *Exploiting Passive Polarimetric Imagery For Remote Sensing Applications*. PhD thesis, New Mexico State University, May 2008.

119. Vimal Thilak, Charles D. Creusere, and David G. Voelz. Passive polarimetric imagery-based material classification robust to illumination source position and viewpoint. In Jenq-Neng Hwang, editor, *IEEE Transactions on Image Processing*, volume 20, pages 288–292, January 2011.

120. Milo W. Hyde IV. *Determining the Index of Refraction of an Unknown Object Using Passive Polarimetric Imagery Degraded by Atmospheric Turbulence*. PhD thesis, Air Force Institute of Technology, Wright-Patterson Air Force Base, Ohio, August 2010.

121. Milo W. Hyde IV, Stephen C. Cain, Jason D. Schmidt, and Michael J. Havrilla. Material classification of an unknown object using turbulence-degraded polarimetric imagery. *IEEE Transactions on Geoscience and Remote Sensing*, 49(1):264–276, January 2011.

122. Cong Phuoc Huynh, Antonio Robles-Kelly, and Edwin Hancock. Shape and refractive index recovery from single-view polarisation images. *IEEE Conference on Computer Vision and Pattern Recognition*, pages 1229–1236, 2010.

123. David Wellems, Steve Ortega, David Bowers, Jim Boger, and Matthew Fetrow. Long wave infrared polarimetric model: theory, measurements and parameters. *Journal of Optics A: Pure and Applied Optics*, 8:914–925, March 2006.

124. Matthew P. Fetrow, David L. Wellems, Stephanie H. Sposato, Kenneth P. Bishop, Thomas R. Caudill, Michael L. Davis, and Elizabeth R. Simrell. Results of a new polarization simulation. *Proc. SPIE 4481 Polarization Analysis Measurement and Remote Sensing IV*, 4481:149–162, 2002.

125. D.L. Jordan, G.D. Lewis, and E. Jakeman. Emission polarization of roughened glass and aluminum surfaces. *Applied Optics*, 35(19):3583–3590, July 1996.

126. I. Bloomer A.R. Forouhi. Optical dispersion relations for amorphous semiconductors and amorphous dielectrics. *Physical Review B*, 34(10):7018–7026, 1986.

127. R. Brendel and D. Bormann. An infrared dielectric function model for amorphous solids. *Journal of Applied Physics*, 71(1), 1992.

128. Josef Humlicek. *Handbook of Ellipsometry*. William Andrew Publishing, 2005.

129. The MathWorks, Inc., Natick, Massachusetts, United States. *MATLAB Release 2015b*.

130. Alexander Berk, Lawrence S. Bernstein, and David C. Robertson. Modtran: A moderate resolution model for lowtran. Technical Report 12, Spectral Sciences Inc., 1987.

131. Viney P. Aneja, Candis S. Claiborn, Zeng Li, and Anuradha Murthy. Trends, seasonal variations, and analysis of high-elevation surface nitric oxide, ozone, and hydrogen peroxide. *Atmospheric Environment*, 28(10):1781–1790, 1994.

132. Stephen J. Young, Robert Johnson, and John A. Hackwell. An in-scene method for atmospheric compensation of thermal hyperspectral data. *Journal of Geophysical Research*, 107(D24), 2002.

133. Kristan P. Gurton and Rachid Dahmani. Effect of surface roughness and complex indices of refraction on polarized thermal emission. *Applied Optics*, 44(26):5361–5367, September 2005.

134. Roy M. Waxler and G. W. Cleek. The effect of temperature and pressure on the refractive index of some oxide glasses. *Journal of Research of the National Bureau of Standards A*, 77A(6):755–763, 1973.

REPORT DOCUMENTATION PAGE

The public reporting burden for this collection of information is estimated to average 1 hour per response, including the time for reviewing instructions, searching existing data sources, gathering and maintaining the data needed, and completing and reviewing the collection of information. Send comments regarding this burden estimate or any other aspect of this collection of information, including suggestions for reducing the burden, to Department of Defense, Washington Headquarters Services, Directorate for Information Operations and Reports (0704-0188), 1215 Jefferson Davis Highway, Suite 1204, Arlington, VA 22202-4302. Respondents should be aware that notwithstanding any other provision of law, no person shall be subject to any penalty for failing to comply with a collection of information if it does not display a currently valid OMB control number. **PLEASE DO NOT RETURN YOUR FORM TO THE ABOVE ADDRESS.**

1. REPORT DATE *(DD-MM-YYYY)*	2. REPORT TYPE	3. DATES COVERED *(From - To)*

4. TITLE AND SUBTITLE

5a. CONTRACT NUMBER

5b. GRANT NUMBER

5c. PROGRAM ELEMENT NUMBER

6. AUTHOR(S)

5d. PROJECT NUMBER

5e. TASK NUMBER

5f. WORK UNIT NUMBER

7. PERFORMING ORGANIZATION NAME(S) AND ADDRESS(ES)

8. PERFORMING ORGANIZATION REPORT NUMBER

9. SPONSORING/MONITORING AGENCY NAME(S) AND ADDRESS(ES)

10. SPONSOR/MONITOR'S ACRONYM(S)

11. SPONSOR/MONITOR'S REPORT NUMBER(S)

12. DISTRIBUTION/AVAILABILITY STATEMENT

13. SUPPLEMENTARY NOTES

14. ABSTRACT

15. SUBJECT TERMS

16. SECURITY CLASSIFICATION OF:			17. LIMITATION OF ABSTRACT	18. NUMBER OF PAGES	19a. NAME OF RESPONSIBLE PERSON
a. REPORT	b. ABSTRACT	c. THIS PAGE			
					19b. TELEPHONE NUMBER *(Include area code)*